Preparation of an Optically Trapped Fermi-Fermi Mixture of ^{6}Li and ^{40}K Atoms and Characterization of the Interspecies Interactions by Feshbach Spectroscopy

Dissertation

zur Erlangung des akademischen Grades
Doktor der Naturwissenschaften

eingereicht an der
Fakultät für Mathematik, Informatik und Physik
der Universität Innsbruck

von

Eric Wille

Betreuer der Dissertation:
Univ.Prof. Dr. Rudolf Grimm
Institut für Quantenoptik und Quanteninformation
Institut für Experimentalphysik

Innsbruck, Februar 2009

Abstract

This thesis describes an experiment capable to study ultracold mixtures with Li, K, and Sr, all having fermionic isotopes. We present the creation of an ultracold mixture of the two fermionic species ^{6}Li and ^{40}K. As the main scientific results of first experiments with this mixture, we present 13 heteronuclear magnetic Feshbach resonances in different stable spin mixtures. The positions of the resonances allow to determine the overall scattering properties for an ultracold ^{6}Li-^{40}K mixture in dependence of an external magnetic field.

Ultracold atomic Fermi gases are a unique experimental system to study the fundamental physics of Fermi many-body systems. Experiments with a single atomic species led to ground breaking results during the last few years. Heteronuclear mixtures of atoms are opening up new possibilities to study new kinds of fermionic quantum systems. Feshbach resonances are essential tools to vary the interaction properties of the atoms and for producing pairs like diatomic molecules or Cooper pairs.

The experimental setup is described in detail with a special emphasis on the new or improved technologies we had to develop in order to simultaneously work with Li, K, and Sr. The design of the machine provides a large variety of state-of-the-art techniques to trap, manipulate, and observe ultracold atomic mixtures.

Different isotopic combinations of Li, K, and Sr can be loaded into a multi-species magneto-optical trap (MOT), using a multi-species oven and a single Zeeman slower. Various magnetic and optical traps can be used for evaporative cooling and the creation of different potentials. A sophisticated coil system is used to control the magnetic field and its derivatives in different directions. Simultaneous imaging of the different atoms species can done by using fluorescence or absorption imaging techniques from different directions. Due to the complexity of an experiment with three different elements, special care was taken during design and construction in order to minimize the daily maintenance work.

The experiments presented in this thesis concentrate on the fermionic mixture with ^{6}Li and ^{40}K. From the MOT, both elements are loaded into a high-power optical dipole trap. We demonstrate the sympathetic cooling of ^{40}K by the evaporation of a ^{6}Li mixture in the lowest two spin states. Using the well-known ^{6}Li Feshbach resonance around 834 G, the ^{6}Li atoms provide an efficient coolant. At temperatures close to quantum degeneracy, we prepare different spin mixtures of ^{6}Li and ^{40}K to perform inelastic loss spectroscopy in dependence of the magnetic field. We observe 13 heteronuclear Feshbach resonances for different spin combinations. Our experimental findings were used in theoretical models by collaborating groups to characterize the Feshbach resonances and gain a full understanding of the scattering properties. The knowledge of the scattering properties now allows us to plan future studies with the newly available ^{6}Li-^{40}K Fermi gas mixture.

Contents

Chapter 1

Introduction

The quantum physics of Fermi systems plays an important role in many different fields of fundamental and applied physics. Numerous technical applications like semiconductor lasers [1], high-temperature superconductors [2], or Josephson junctions [3] are based on the quantum nature of the Fermi gas of electrons. But despite the widespread importance of fermionic many-body systems, the complexity of these systems still causes many open questions. Besides for the technological relevant field of solid state physics, Fermi systems are also important for the understanding of nuclear or quark matter in the context of particle- and astrophysics [4, 5]. This thesis presents experiments with atomic Fermi gases of ^{6}Li and ^{40}K. Fermionic quantum gases of atoms have recently become available for experiments and offer many novel possibilities [6]. To understand the interest in this special mixture, we will first give a brief overview of the history of quantum gases.

The different statistical properties of bosons and fermions were discovered in the 1920s. Satyendra Bose formulated the statistics for photons 1924 [7] and one year later, Albert Einstein generalized the concept for atoms [8]. In the year 1926, Enrico Fermi and Paul Dirac introduced the statistics for fermions [9, 10].

A direct consequence of the statistical properties is the existence of quantum gases at low temperatures with properties very different from classical gases. The theory of Fermi gases allows to understand the properties of white dwarfs (Ralph Fowler, 1926 [11]) and electrons in matter (Arnold Sommerfeld, 1928 [12]). bosons can form a Bose-Einstein condensate (BEC), which was discovered in the form of superfluid ^{4}He in 1937 by Pyotr Kapitsa, John F. Allen, and Don Misener [13, 14].

The phenomenon of superconductivity of metals was already found in 1911 by Heike Kamerlingh Onnes [15]. But it took until 1957 until John Bardeen, Leon Cooper, and Robert Schrieffer formulated the BCS theory to describe superconductivity [16, 17]. The basic idea of the BCS theory is to pair two fermions to a composite boson, a Cooper pair. The composite bosons can form a Bose-Einstein condensate with superconducting properties. The BCS theory

connected the different worlds of bosons and fermions. In 1972, a superfluid phase was discovered in liquid ^{3}He by David Morris Lee, Douglas Osheroff and Robert Coleman Richardson [18]. Here, the fermionic ^{3}He atoms form pairs, which can undergo Bose-Einstein condensation. Despite the success of the BCS theory, it cannot describe all superconducting systems. In 1986, Bednorz and Müller discovered a novel type of superconductors, which lose their electrical resistivity at 35 K [19] or at even higher temperatures. The nature of the electron pairs leading to this so-called high-temperature superconductivity is not yet fully understood.

With the special exception of superfluid Helium, other atoms could not be cooled to quantum-degeneracy before 1995 [20] despite years of serious efforts. The group of Eric Cornell and Carl Wieman could produce the first Bose-Einstein condensate of dilute atomic gases. They used ^{87}Rb atoms trapped and cooled with resonant laser light and subsequent evaporative cooling in a magnetic trap. Quantum-degenerate gases of atoms quickly showed a large potential for the fundamental research of quantum physics [21].

The successful techniques used for experiments with Bose-Einstein condensates led to the first creation of an atomic Fermi gas of ^{40}K in 1999 [22]. One major interest for fermionic quantum gases was to study the crossover from a molecular Bose-Einstein condensate to a quantum gas of Cooper pairs with atoms. The first step into the crossover was done by producing a BEC of $^6Li_2$ molecules in 2003 [23]. This year marked the onset of many spectacular experiments over the whole crossover region [6]. Like the experiments with bosonic atoms, fermionic atoms proved to be ideal systems to study quantum physical systems not available before.

The experiment described in this thesis started in 2004. At that time, experiments were limited to homonuclear Fermi gases of either ^{6}Li or ^{40}K. But many physical phenomena of Fermi gases are related to the presence of a mixture of different kinds of fermions. Such imbalanced or heteronuclear gases are especially important in the context of high-temperature superconductivity or the physics of colour superconductivity in quantum chromodynamics [4, 5]. Consequently, our group in Innsbruck and several other groups started to build experiments to study heteronuclear Fermi gases of atoms.

The technology and physics required to study Fermi gases of either ^{6}Li or ^{40}K were already well-known. Furthermore, these two alkali isotopes are the only naturally occuring fermionic atoms. Therefore, the mixture of ^{6}Li and ^{40}K is the natural choice to start studying heternuclear Fermi gases of atoms. After deciding to use these two species, we named our project FeLiKx (Fermionic Li-K experiment). Later, we decided to include Strontium as a third species. Strontium as an alkaline earth atom offers many different properties and extends the future possibilites of the FeLiKx project.

The work of this thesis comprises the design and construction of the FeLiKx experiment as well as the first experiments with a mixture of ^{6}Li and ^{40}K atoms. The interactions between these two species are the most important property to study the quantum physics of Fermi gases. Especially magnetic Feshbach resonances [24] are important to create molecules and to access the BEC-BCS crossover. No information about the interaction properties and Feshbach resonances of ^{6}Li and ^{40}K was available before. Consequently, the first experiments with a mixture

of ^{6}Li and ^{40}K atoms were devoted to the investigation of magnetic Feshbach resonances. The knowledge of the resonance positions allows to deduce the complete interaction properties at low temperatures using theoretical models. These topics are presented in the chapters following this introduction.

Chapter 2 presents a brief theoretical overview of three different topics. First, the BEC-BCS crossover is discussed to give the reader the necessary background to understand the major scientific goal of the FeLiKx project. Afterwards, the physics of ultracold collisions is summarized. The understanding of collisions is important for the experimental strategy to reach temperatures in the ultracold regime. Furthermore, the interactions of the ultracold quantum gases are determined by their collision properties. The final topic of chapter 2 covers the physics of Feshbach resonances.

Chapter 3 describes the design and properties of the FeLiKx experiment. This includes the vacuum chamber, the laser systems, the Zeeman slower, the magnetic field coils, the magneto - optical trap, the different optical dipole traps, the imaging systems, the electronic control system and many smaller subsystems. Special emphasis is put on the devices we had to develop to render the combination of Li, K and Sr atoms possible.

Chapter 4 discusses the different techniques we use to trap and cool a mixture of ^{6}Li and ^{40}K. This includes the operation of the multi-species magneto-optical trap, the transfer into an optical dipole trap and evaporative cooling.

Chapter 5 presents our experiments to search the Feshbach resonances between ^{6}Li and ^{40}K. We could locate 13 different resonances and deduce the precise interaction properties with the help of two different theoretical models used by collaborating groups.

Chapter 6 summarizes the content of this thesis and gives an outlook for future experiments based on the results.

Chapter 2

Interactions in Ultracold Fermi Gases

The objective of the FeLiKx project is to study heteronuclear mixtures of atomic Fermi gases. The first section of this chapter presents the theoretical background to understand the basic physics of degenerate Fermi gases. The second section gives a more detailed description of the theory of ultracold collisions, which are important for evaporative cooling, the stability of quantum gas mixtures, and for searching Feshbach resonances. The third section describes the theory of Feshbach resonances, whose exploration is the main scientific result of this thesis. The theoretical background described in this chapter is far from being complete. It should only introduce the concepts being important for the following chapters. For stringent derivations and more details, the reader is asked to consult the cited literature.

2.1 Basic Theory of Quantum Gases

The spin-statistic theorem formulated by Fierz [25] and Pauli [26] relates the spin of a particle to the statistics of a many-body system of these particles. As a consequence, there are two different classes of particles[1]. Systems of identical particles with an integer spin have symmetric wave functions under exchange of the particles - they are called bosons. Systems of identical particles with an half-integer spin have anti-symmetric wave functions under exchange of the particles - they are called fermions. A further consequence of the spin-statistic theorem is the Pauli exclusion principle for fermions. It states that two identical fermions cannot occupy the same quantum state. bosons in contrast are allowed to occupy identical quantum states. This fundamental difference in the behavior of fermions and bosons builds the foundation of a multitude of physical phenomena. We are only able to list a few like the periodic system of the elements, the laser, the conductivity or even superconductivity of metals. A many-body system of bosons or fermions at low temperatures is often called a quantum gas. The following sections will discuss the basic

[1]The spin-statistic theorem assumes a Lorentz invariant space. This is not always the case, as for example in two dimensional geometries. Particles with different spins and statistics can exist under these conditions.

theoretical properties of fermionic and bosonic quantum gases and show how the two different fields can be connected.

2.1.1 Bosons and Fermions

The many-body physics of bosons and fermions can be described using methods from statistical mechanics. The basic properties and differences can already be understood by looking only at the statistics of a non-interacting ensemble of bosons or fermions. This case is presented in the next paragraphs, while the physics of interacting particles is discussed in the next section.

The thermodynamical properties of quantum gases can be derived using a suitable potential. We will use the grand potential

$$J = U - TS - \sum_i \mu_i N_i \tag{2.1}$$

defined by the internal energy U, the product of the temperature T and entropy S and the products between the chemical potentials μ_i and the number N_i for particles of type i. The grand canonical potential can be derived using the density operator ρ of the many-body system

$$\rho = \frac{1}{\tilde{z}} \mathrm{e}^{-\beta(H-\mu N)}. \tag{2.2}$$

H is the Hamiltonian of the many-body system with a temperature expressed by $\beta = (k_B T)^{-1}$. The normalizing constant $\tilde{z} = \mathrm{Tr}\exp(-\beta(H-\mu N))$ is called the partition function and leads to the grand potential by

$$J = -k_B T \ln \tilde{z}. \tag{2.3}$$

Having n_k particles with energy ϵ_k the trace can be calculated and we get

$$J = -k_B T \ln \sum_{\{n_k\}} \prod_k [\mathrm{e}^{-\beta(\mu-\epsilon_k)}]^{n_k} = \mp k_B T \sum_k \ln[1 \pm \mathrm{e}^{\beta(\mu-\epsilon_k)}]. \tag{2.4}$$

The upper sign is valid for fermions ($n_k \in \{0,1\}$) and the lower sign for bosons ($n_k \in \mathbb{N}_0$). The convergence of the geometrical sum requires $\mu < 0$ in the bosonic case. The distribution functions $\bar{n}_k$ for non-interacting fermions and bosons are derived as

$$\bar{n}_k = \frac{\partial J_k}{\partial \mu} = \mp k_B T \frac{\partial \ln[1 \pm \mathrm{e}^{\beta(\mu-\epsilon_k)}]}{\partial \mu} = \frac{1}{\mathrm{e}^{\beta(\epsilon_k-\mu)} \pm 1}. \tag{2.5}$$

Figure 2.1 shows the distribution functions for different temperatures. If the temperature is equal to zero, fermions occupy all the lowest energy states up to the chemical potential. This reflects the Pauli exclusion principle as two identical fermions cannot be in the same quantum state. The Fermi energy E_F is defined to be the energy of the highest occupied state at zero temperature.

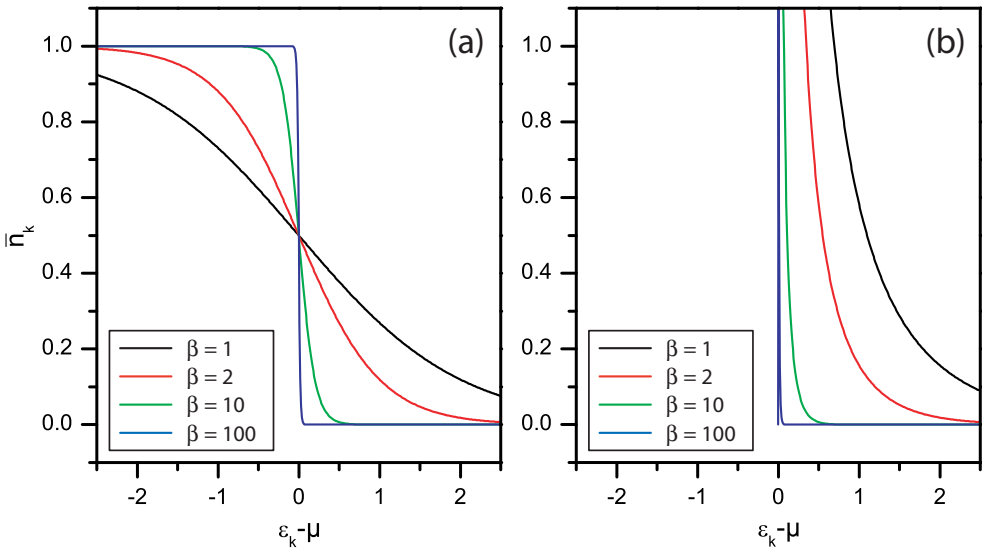

Figure 2.1: Fermi (a) and Bose (b) distribution functions for different values of β.

Note that the Fermi energy is equal to the chemical potential at zero temperature but not anymore for finite temperatures. The Fermi energy can be calculated for a homogeneous Fermi gas as

$$E_F = (6\pi^2)^{\frac{2}{3}} \frac{\hbar^2}{2m} \left(\frac{N}{V}\right)^{\frac{2}{3}}, \tag{2.6}$$

where m is the mass of the particles and N/V the number N of particles per volume V. At finite temperatures, the particles are excited to higher energy states and the step function of the Fermi distribution is smoothened out. The Fermi energy is related to the Fermi momentum $\hbar k_F$ and the Fermi temperature T_F by

$$E_F = \frac{\hbar^2 k_F^2}{2m} = k_B T_F. \tag{2.7}$$

A non-interacting gas of bosons behaves very differently. At zero temperature, all particles occupy the ground state. Consequently, the chemical potential is zero for $T = 0$. If the temperature is increased, more and more particles leave the ground state and occupy higher energy states. But the chemical potential remains zero until the ground state is not occupied with a macroscopic number of particles anymore. This transition occurs at the condensation temperature

$$T_{C,BEC} = \frac{2\pi}{(\zeta(3/2))^{2/3}} \frac{\hbar^2}{m k_B} \left(\frac{N}{V}\right)^{\frac{2}{3}} \tag{2.8}$$

where ζ is the Riemann zeta function with $\zeta(3/2) \approx 2.61$. The particles condensed in the ground state form a so-called Bose-Einstein condensate (BEC). Note that the transition for a Bose gas from zero to finite chemical potential is a second-order phase transition while the Fermi gas does not undergo any phase transition.

The theory described so far is valid for a quantum gas with a single species of non-interacting particles without a trapping potential. The next section describes the extension towards systems with two different kinds of interacting fermions.

2.1.2 Pairing Fermions

Two different fermionic particles can form a pair. Since each of the fermions has a half-integer spin, the spin of the composite pair is an integer. Therefore, the pair is a boson. In the last section, we have seen that fermions and bosons have very different properties. Pairing of fermions connects the physics of Fermi and Bose gases.

The pairing properties of two particles depend on the interaction, which induces an inter-particle potential $V(\vec{r})$, where $\vec{r}$ is the distance between the two particles. The quantum phenomena of Fermi and Bose gases typically occur at very low temperatures. In this regime, the interaction can be described by the s-wave scattering length a because higher partial waves require more energy than available for the cold particles (see section 2.2.1 for details). For identical fermions, s-wave scattering is forbidden because of its even exchange symmetry. Therefore, two different kind of fermions are required to study interacting many-body systems. This can be either realized by mixing two different species or by using the same kind of particles in two different internal quantum states. We will label the two types with $\uparrow$ and $\downarrow$.

The scattering length a can take all values between $\pm\infty$ including zero. For $a = 0$, the two different fermions are non-interacting and form two independent Fermi distributions. A weak interaction can be either weakly repulsive for $0 < k_F a \ll 1$ or weakly attractive for $-1 \ll k_F a < 0$. The fermions are strongly interacting if $k_F|a| \gtrsim 1$. The inverse scattering parameter $(k_F a)^{-1}$ is frequently used to map the transition between $\pm\infty$ onto the zero crossing. The following paragraphs discuss the pairing possibilities in these different regimes. We will treat the case of two fermionic components with identical densities $N_\uparrow/V = N_\downarrow/V = N/V$ and masses $m_\uparrow = m_\downarrow = m$.

A very instructive analysis of fermionic pairing is the mean field approach by Eagles [27] and Leggett [28]. We base our discussion on recent articles reviewing the topic in the context of cold atomic gases [6, 29]. The mean field approach allows to calculate the order parameter[2] Δ, the chemical potential μ and the single-particle excitation spectrum

$$E_{\vec{k}} = \sqrt{\Delta^2 + \left(\frac{\hbar^2\vec{k}^2}{2m} - \mu\right)^2} \tag{2.9}$$

in dependence of the interaction $(k_F a)^{-1}$, where k is the wavenumber of the particles. It is important to understand the exact meaning of these parameters in the context of a system with

[2]More precisely, the order parameter is a complex number Δe^{iS} where S is the phase. The phase is especially important to describe the superfluid properties of the quantum gas. As our discussion is limited to the single-particle excitations, we will continue to work with the absolute value Δ for simplicity and call it order parameter.

two types of fermions. The chemical potential μ is defined as half of the energy difference between the ground states (GS) with $(N_\uparrow, N_\downarrow)$ particles and $(N_\uparrow + 1, N_\downarrow + 1)$ particles:

$$\mu = \frac{1}{2}\left[E_{\text{GS}}(N_\uparrow + 1, N_\downarrow + 1) - E_{\text{GS}}(N_\uparrow, N_\downarrow)\right]. \tag{2.10}$$

Note that the possibility of pairing of the two additional particles affects the chemical potential. The single-particle excitation spectrum is defined as

$$\begin{aligned} E_{\vec{k}} &= E_{\vec{k}}(N_\uparrow + 1, N_\downarrow) - \frac{1}{2}\left[E_{\text{GS}}(N_\uparrow + 1, N_\downarrow + 1) + E_{\text{GS}}(N_\uparrow, N_\downarrow)\right] \\ &= E_{\vec{k}}(N_\uparrow + 1, N_\downarrow) - E_{\text{GS}}(N_\uparrow, N_\downarrow) - \mu. \end{aligned} \tag{2.11}$$

In this case, a single fermion with momentum $\hbar\vec{k}$ is added without the possibility to form a pair. The minimum of $E_{\vec{k}}$ is called the gap

$$\Delta_{\text{gap}} = \min_{\vec{k}} E_{\vec{k}}. \tag{2.12}$$

The gap is the lowest energy required to add a single particle compared to half of the energy required to add a pair. Since breaking a pair produces two free particles, the energy needed to do so is twice the gap. The gap should not be confused[3] with the order parameter Δ. The order parameter measures the presence of a macroscopic occupation of a paired state. Therefore, if Δ becomes zero, the system passes a phase transition from a symmetry-broken state to a symmetric state as described by the standard Ginzburg-Landau theory.

The parameters Δ, Δ_{gap}, μ and the excitation spectrum $E_{\vec{k}}$ vary depending on the interaction $(k_F a)^{-1}$. An analytical solution is available in the form of elliptic integrals [30]. The results are shown in Fig. 2.2. They provide a good insight into the different regimes of two component Fermi gases. In addition, the figure shows the energy of the bound state for a two-body system

$$E_B = -\frac{\hbar^2}{ma^2}. \tag{2.13}$$

It is zero for $k_F a < 0$ where no bound state exists close below the dissociation threshold. A two-body bound state emerges at $(k_F a)^{-1} = 0$ with a binding energy increasing quadratically for positive $k_F a$. For a better comparison with the single-particle values Δ, Δ_{gap} and μ, the bound state energy per particle $E_B/2$ is plotted.

The regime of weakly attractive fermions with $-1 \ll k_F a < 0$ is described by the Bardeen-Cooper-Schrieffer (BCS) theory [16, 17] from 1957. Compared to the non-interacting case, the ground state of the system with an arbitrarily weak interaction is not described anymore by two Fermi distributions. The weak interaction gives rise to a bound state between two fermions, which can form a so-called Cooper pair. It is important to note that the bound state does not exist in the two-body picture but only in the many-body picture. The reason is that the Fermi

[3] Some texts call Δ the gap.

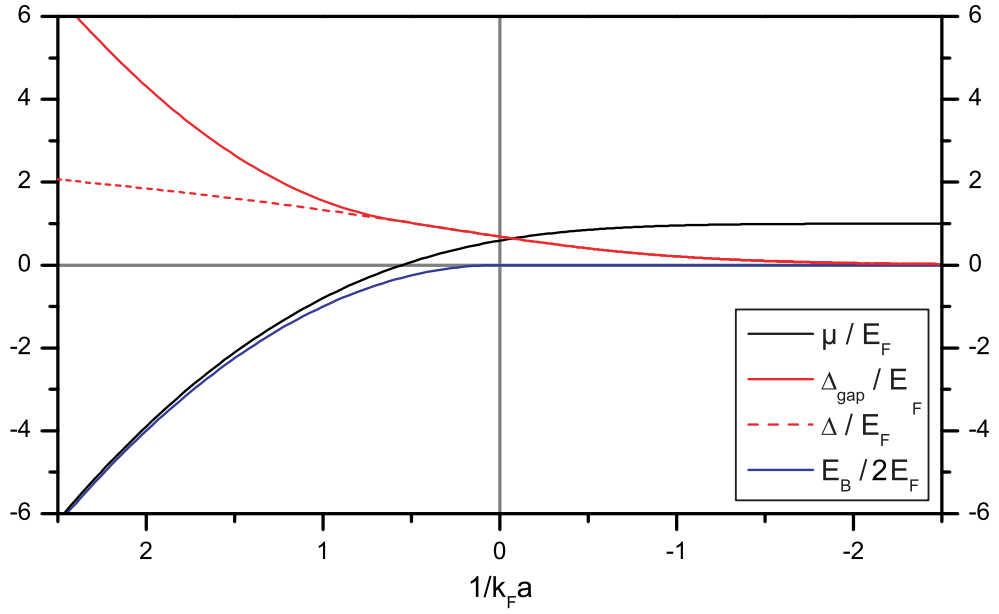

Figure 2.2: Relevant energies within the BEC-BCS crossover. Shown is the chemical potential μ (black), the gap Δ_{gap} (red, solid line) and the order-parameter Δ (red, dashed line) using the mean-field approach. Additionally, the two-body bound state energy for repulsive interaction $1/k_F a < 0$ is shown in blue.

distribution of all the particles blocks the states with an energy smaller than E_F. The density of states available for particles at the edge of the Fermi distribution is therefore modified and leads to the existence of the bound state. The binding energy of the Cooper pairs is equal to two times the gap

$$2\Delta_{\text{gap}} = \frac{16}{\text{e}^2} E_F \text{e}^{-\frac{\pi}{2k_F|a|}}. \tag{2.14}$$

This equation does not include the Gorkov-Melik-Barkhudarov correction, which adds a factor of $(4e^{-1/3})$ to the right-hand side [29, 31]. For decreasing interaction $k_F a$, the gap shrinks exponentially. The chemical potential approaches the Fermi energy in this regime. This is easily understood as additional particles have to be placed on top of the Fermi distribution. Also the single-particle excitation spectrum reflects the edge of the Fermi distribution (see Fig. 2.3). The minimum excitation occurs with particles close to the Fermi momentum $\hbar k_F$. Consequently, the Cooper pairs only exist close to the Fermi surface $|\vec{k}| = k_F$ within a small region with a width proportional to the gap. Pairing is achieved with particles of opposite momenta $\vec{k}_\uparrow = -\vec{k}_\downarrow$.

For increasing interaction $1/k_F a \to 0$, the gap and the binding energy of a Cooper pair, becomes larger. The minimum of the excitation spectrum is shifted towards smaller values $k_{min} < k_F$. An increasing part of the fermions inside the Fermi distribution is paired. Also the character of the pairs changes. In the BCS regime, the paired fermions are strongly correlated in the momentum space where only states with $|\vec{k}| \approx k_F$ are available. Now, the pair can

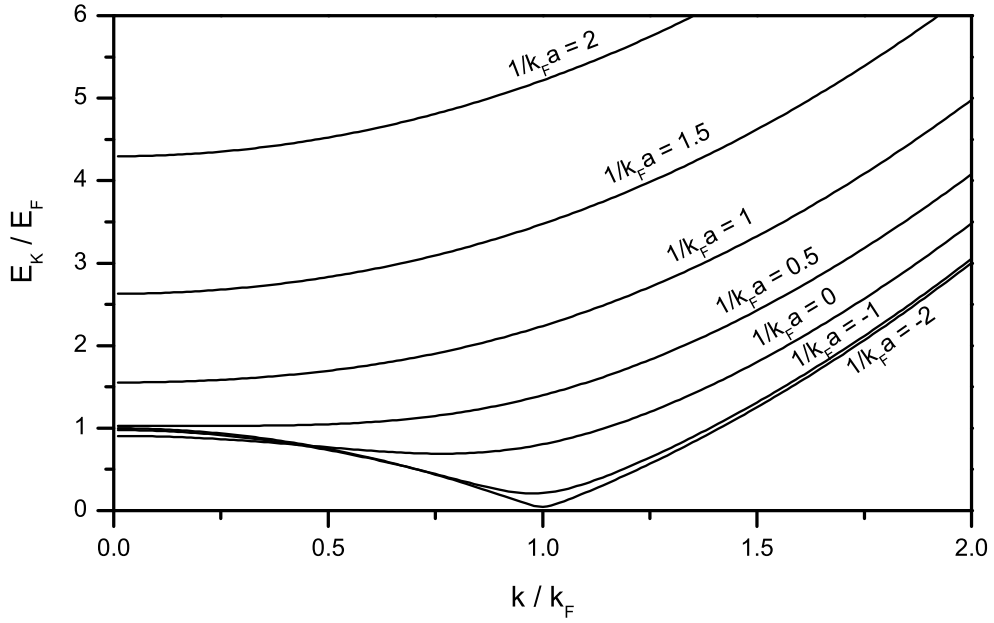

Figure 2.3: Single-particle excitation spectrum. The excitation spectra (see equation (2.9)) are shown for different interaction parameters within the BEC-BCS crossover. The minimum position of the excitation energy is located around $k = k_F$ for weak attractive interactions. It moves towards $k = 0$ for increasing interaction strength until it reaches $k = 0$ for $1/k_F a = 0.55$. The value of the minimal excitation energy Δ_{gap} can also be seen in Fig. 2.2.

occupy a large part of the momenta $|\vec{k}| \lessgtr k_F$ and the correlation is not restricted to the momentum space anymore. Around $1/k_F a \approx 0$ the chemical potential is of equal size as the gap. Consequently, the entire momentum space is available.

For $1/k_F a = 0.55$ the chemical potential changes sign and becomes negative. This has important consequences for the pairing. The minimum of the excitation spectrum does not occur anymore for $k \neq 0$. Regarding equation (2.9) and Fig. 2.3, the gap Δ_{gap} is not equal to the order parameter Δ anymore but becomes

$$\Delta_{\text{gap}} = \min_k E_k = \begin{cases} |\Delta| = & \mu \geq 0 \\ \sqrt{\Delta^2 + \mu^2} = & \mu < 0. \end{cases} \tag{2.15}$$

The chemical potential contributes to the gap Δ_{gap} of the pair and becomes the dominant part for increasing values of $1/k_F a$.

In the weakly repulsive regime $1/k_F a \gg 1$, the contribution of the order parameter Δ is negligible and the gap, respectively the pair binding energy $2\Delta_{\text{gap}}$ evolves to

$$2\Delta_{\text{gap}} = -2\mu = \frac{E_F^2}{k_F^2 a^2} = \frac{\hbar^2}{2ma^2} = -E_B. \tag{2.16}$$

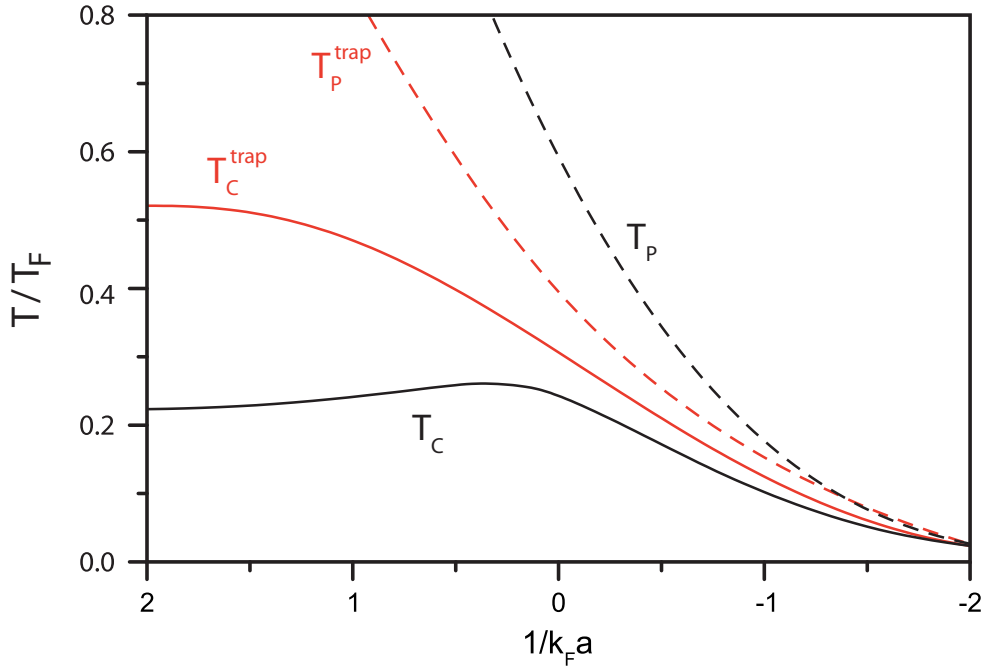

Figure 2.4: Pairing temperature T_P (black dashed line) and critical temperature T_C (black solid line) within the BEC-BCS crossover in the homogeneous case. The temperatures $T_{P,C}^{\text{trap}}$ for a gas in a harmonic trap are shown in red. Crossing the critical temperature is accompanied with a phase transition while the pairing temperature indicates a smooth transition. Both temperatures exponentially approach $T = 0$ for $1/k_F a \to -\infty$. The figure is based on data from [33].

The gap that characterizes the binding of the fermion pairs becomes equal to half the bound state energy of the two-body system. Furthermore, the Fermi energy does not enter the binding energy anymore. The pairs are now characterized by a wave function corresponding to the last bound state of the interaction potential that occurred at $1/k_F a = 0$. The pairs are correlated in local space. Equation (2.16) shows that the chemical potential for two particles is equal to the binding energy. We can introduce another chemical potential $\mu_{\uparrow\downarrow} = 2\mu - E_B$ for a bound pair and immediately get $\mu_{\uparrow\downarrow} = 0$. This is exactly the requirement for a Bose-Einstein condensate as discussed in section 2.1.1. But instead of bosonic particles, we have a BEC of paired fermions. In the case of atoms, the pairs are called molecules as they occupy a bound state of the interaction potential. The crossover through the interaction range $1/k_F a \gtrless 0$ is called the BEC-BCS crossover. Note, that this is a smooth crossover without any phase transitions as the order parameter Δ stays finite.

After having discussed the BEC-BCS crossover for zero temperature, we briefly want to present the case for finite temperatures. For $T \neq 0$ an analytical treatment is not possible anymore. First studies of this problem were done by Nozières and Schmitt-Rink [32]. The basic results are presented in Fig. 2.4. The two different energies Δ and Δ_{gap} give rise to two characteristic temperatures of the system.

The temperature T_C is defined as the temperature at which the order parameter Δ crosses zero and a phase transition occurs. For temperatures below this critical temperature T_C spontaneous symmetry breaking occurs. The order parameter becomes nonzero, with a well defined fixed phase. This gives rise to the phenomena of long-range coherence and superfluidity. The other energy is given by the gap $\Delta_{\text{gap}} \geq \Delta$, which corresponds to half the binding energy of the pairs. If the temperature increases towards $k_B T_P \approx \Delta_{\text{gap}}$ the pairs break up. This is not a phase transition and the breaking of the pairs occurs smoothly around T_P.

Figure 2.4 shows the critical temperature T_C and the pairing temperature T_P for the BEC-BCS crossover. In the BCS limit, both temperatures approach zero exponentially [34]

$$\frac{T_C}{T_F} = \left(\frac{2}{e}\right)^{\frac{7}{3}} \frac{\gamma}{\pi} e^{-\frac{\pi}{2k_F|a|}} = \frac{\gamma}{\pi} \frac{\Delta_{\text{gap}}(T=0)}{E_F}, \tag{2.17}$$

where $\gamma \simeq 1.781$ is a constant and the equation includes the Gorkov-Melik-Barkhudarov correction. Consequently, pairing and the phase transition coincide.

The phase transition occurs at temperatures very small compared to the Fermi temperature. This BCS region corresponds to the low temperature superconductors where $T_C/T_F \approx 10^{-8}$.

For stronger interactions in the crossover regime $1/k_F|a| \lesssim 1$ the pairing temperature becomes significantly larger than the critical temperature. Pairs can exist without the gas being superfluid for $T_C < T < T_P$. As both temperatures are only one order of magnitude below the Fermi temperature, pairing and superfluidity is easier to reach in experiments. High-temperature superconductors are close to this regime with $T_C/T_F \approx 10^{-2}$.

On the BEC side of the crossover, the pairing temperature is related to the binding energy of the molecules. It increases quadratically and T_P becomes much larger than the Fermi temperature. The critical temperature becomes

$$\begin{aligned} \frac{T_C}{T_F} &= 2\pi \left(6\pi^2 \zeta(3/2)\right)^{-\frac{2}{3}} \approx 0.218 \\ &= \frac{1}{T_F} \frac{\pi}{(\zeta(3/2))^{2/3}} \frac{\hbar^2}{m k_B} \left(\frac{N}{V}\right)^{\frac{2}{3}}, \end{aligned} \tag{2.18}$$

which is the same critical temperature as in equation (2.8) for molecules with a mass of $2m$.

The mean-field ansatz discussed in the last paragraphs is very insightful because of the possibility to treat the whole BEC-BCS crossover analytically. But although the outcomes agree qualitatively to more sophisticated theories, most quantitative results are not correct at first or higher order. Better models are available either for the limiting cases of the crossover or by using powerful numerical methods.

Additionally, models for quantum gases in trapping potentials require further modifications like a local density approximation. These results will again differ significantly from the presented homogeneous case [29, 33]. The pairing temperature and the critical temperature for a gas in a

harmonic trap are shown in Fig. 2.4. The inhomogeneous density distribution in a trap will result in a superfluid region in the center and a surrounding region with a normal gas. This bimodal distribution is very evident on the BEC side and gets weaker for stronger interactions closer to the resonance and on the BCS side.

2.1.3 Imbalanced Pairing

The BEC-BCS crossover as discussed in the previous paragraphs is only valid for equal density and masses of the two fermions. In this case a common chemical potential can be formulated and the two Fermi surfaces overlap. The next step towards the understanding of paired Fermi gases is to consider asymmetric systems with unequal densities and/or masses. At this time, the theories about imbalanced Fermi gases still have many open problems and are an active field of research. Especially in the contexts of high-temperature superconductors and quantum chromodynamics, imbalanced pairing plays an important role [4]. The FeLiKx project should access imbalanced pairing experimentally to contribute to the advancement of that field. To give the reader an idea about the physics of such systems, we can only list some of the existing concepts and first experimental results for imbalanced Fermi gases.

First experiments with imbalanced ^{6}Li Fermi gases have been done by the groups of Hulet [35, 36] and Ketterle [37, 38]. Both groups implemented the imbalance by different atom numbers for two spin states. They found a phase transition from the superfluid state on the BCS side to a normal state and phase separations between pairs and regions with unbound particles. A theoretical treatment of these experiments is presented in the chapter by F. Chevy in reference [6].

Before the first experiments with imbalanced mixtures, different theoretical predictions were elaborated. Clogston [39] and Chandrasekhar [40] found a first-order phase transition within the BEC-BCS crossover, which occurs even at $T = 0$ as soon as the difference of the imbalanced chemical potentials become equal to the gap energy $\sqrt{2}\Delta_{\mathrm{gap}}$. This would typically happen in the BCS regime and the superfluid character is lost for arbitrary small interactions.

Another quantum phase in imbalanced Fermi gases is the predicted Fulde-Ferrell-Larkin-Ovchinnikov [41, 42] state. In this case, the pairs have a finite total momentum, which shifts the unequal Fermi surfaces to cause an overlap. Furthermore, quantum phases with deformed Fermi surfaces [43] have been proposed.

The exotic quantum states mentioned above have not been found experimentally so far. Furthermore, it is unclear whether they exist in trapped geometries and for finite temperatures, as required for an experimental realization. Future experiments will have to show which quantum phases can be produced or whether even new, different phases will be discovered. Experiments can be either done with imbalanced spin-mixtures of a single species or using two different species with unequal masses.

2.2 Ultracold Collisions

Collisions between the particles in a quantum gas play an important role for many reasons. First, the interaction at very low temperatures is predominantly determined by the s-wave scattering length a. As discussed in the last section, the location of the system within the BEC-BCS crossover depends on the value of a. Secondly, collisions are important to render evaporation cooling possible to reach the quantum-degenerate regime. Finally, inelastic collisions influence the lifetime of a trapped sample of atoms. In this section, we will first introduce the basic concepts of scattering theory. Afterwards, we will discuss different kinds of collisions that are important for our experiments. At the end, we will elaborate the consequences for a heteronuclear mixture of ^{6}Li and ^{40}K atoms.

2.2.1 Basic Scattering Theory

Here, we present a very compact derivation of the most important concepts of quantum scattering. More detailed discussions can be found in many textbooks and reviews like [44, 31, 45, 21].

The scattering problem of two particles can be solved using the Schrödinger equation for the relative motion of two particles

$$\left[-\frac{\hbar^2}{2m_r}\nabla^2 + V(\vec{r})\right]\Psi(\vec{r}) = \frac{\hbar^2 k^2}{2m_r}\Psi(\vec{r}), \tag{2.19}$$

where m_r is the reduced mass and $V(\vec{r})$ the inter-particle potential. Restricting the problem to spherical symmetric potentials approaching zero at infinity, we can separate the wave function into radial and angular parts

$$\Psi(\vec{r}) = \sum_{l=0}^{\infty}\sum_{m=-l}^{m=l}\frac{u_l(r)}{r}Y_{l,m}(\vartheta,\varphi) \tag{2.20}$$

using the spherical harmonic functions $Y_{l,m}(\vartheta,\varphi)$. The Schrödinger equation for the radial part becomes

$$\left[-\frac{\hbar^2}{2m_r}\frac{d^2}{dr^2} + \frac{\hbar^2 l(l+1)}{2m_r r^2} + V(r)\right]u_l(r) = \frac{\hbar^2 k^2}{2m_r}u_l(r). \tag{2.21}$$

The angular momentum quantum number l causes a centrifugal barrier for the partial waves of $\Psi(\vec{r})$ with $l > 0$. As $\hbar^2 k^2/m_r > 0$, the radial part $u_l(r)$ has to behave as

$$\lim_{r\to\infty} u_l(r) = c_l \sin(kr + \phi_l), \tag{2.22}$$

with c_l and ϕ_l being amplitudes and phases determined by the solution of the Schrödinger equation. $\phi_l = -l\frac{\pi}{2} + \delta_l$ is a good choice for later convenience. Furthermore, $u_l(r = 0) = 0$ is required to obtain a normalizable solution. This gives the boundary conditions for the Schrödinger equation.

We use the following ansatz to solve the equation. Far outside the interaction potential the solution has the form

$$\lim_{r\to\infty}\psi(\vec{r}) = \mathrm{e}^{ikr\cos\vartheta} + f(k,\vartheta)\frac{\mathrm{e}^{ikr}}{r}, \tag{2.23}$$

with an incoming plane wave and an outgoing scattered spherical wave with the scattering amplitude $f(k,\vartheta)$. The plane wave is incident along the z-axis and the problem becomes independent of the angle φ. This function can be written in the basis of spherical harmonics with the result

$$\lim_{r\to\infty}\psi(\vec{r}) = \sum_{l=0}^{\infty}\frac{1}{r}\left[(-1)^{l+1}\frac{2l+1}{2ik}\mathrm{e}^{-ikr} + \left(\frac{2l+1}{2ik}+f_l\right)\mathrm{e}^{ikr}\right]P_l(\cos(\vartheta)), \tag{2.24}$$

where we have expanded $f(k,\vartheta) = \sum f_l P_l(\cos\vartheta)$ using the Legendre polynomials $P_l(\cos\vartheta)$. Comparing the expression within the squared brackets with the general expansion of the wave function (2.20) and the limiting boundary conditions (2.22) gives

$$u_l(r) = c_l\sin\left(kr + -l\frac{\pi}{2} + \delta_l\right) = \left[(-1)^{l+1}\frac{2l+1}{2ik}\mathrm{e}^{-ikr} + \left(\frac{2l+1}{2ik}+f_l\right)\mathrm{e}^{ikr}\right]. \tag{2.25}$$

This solves the scattering problem with

$$c_l = i^l\frac{2l+1}{k}\mathrm{e}^{i\delta_l} \quad \text{and} \quad f_l = \frac{2l+1}{k}\mathrm{e}^{i\delta_l}\sin\delta_l. \tag{2.26}$$

We conclude that the scattering amplitude $f(k,\vartheta)$ is solely determined by the the scattering phases δ_l.

The scattering phases are related to the cross section and the scattering length of the atoms as we will show in the following. The scattering cross section is given by the absolute square of the scattering amplitude as

$$\sigma(k) = \int |f(k,\theta)|^2 d\Omega. \tag{2.27}$$

At this point it is important to consider the symmetry properties of quantum states for identical particles. For bosons, requiring symmetric wave function, only the even partial waves contribute to the scattering process. For fermions, having anti-symmetric wave functions, only odd partial waves contribute. This results in the following scattering cross sections

$$\sigma(k) = \frac{8\pi}{k^2}\begin{cases}\sum_{l\in 2\cdot\mathbb{N}} (2l+1)\sin^2\delta_l(k) & \text{for bosons}\\ \sum_{l\in 2\cdot\mathbb{N}-1}(2l+1)\sin^2\delta_l(k) & \text{for fermions}\\ \sum_{l\in\mathbb{N}_0} (2l+1)\sin^2\delta_l(k) & \text{for distinguishable particles.}\end{cases} \tag{2.28}$$

In the case of very low energies, collisions can only occur with the lowest angular momenta l. The scattering processes with $l = 0, 1, 2, \ldots$ are called s, p, d-wave scattering and so on. In the limit of zero temperature, the cross section becomes

$$\lim_{k\to 0}\sigma(k) = \begin{cases} 8\pi a^2 & \text{for bosons}\\ 0 & \text{for fermions}\\ 4\pi a^2 & \text{for distinguishable particles.}\end{cases} \tag{2.29}$$

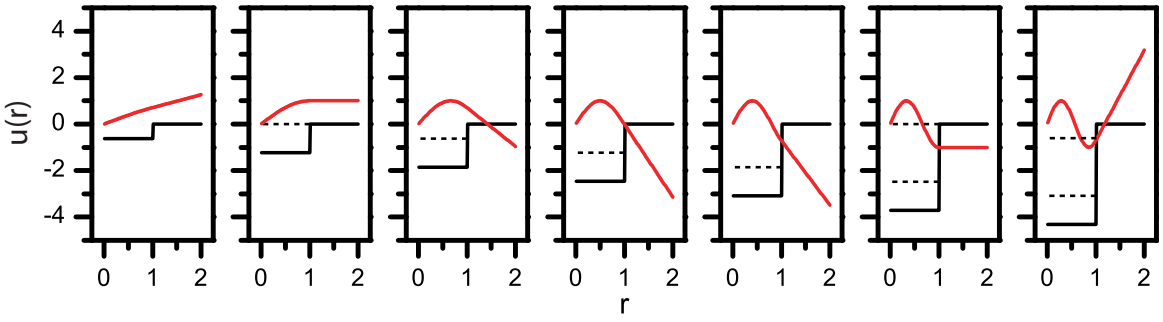

Figure 2.5: Scattering wave function in box potentials with increasing depth. Shown is the radial part $u(r)$ (red line) of the wave function in a one dimensional box potential (black line). With increasing potential depths, new bound states (dashed line) occur.

where we defined the scattering length as

$$a = -\lim_{k\to 0} \frac{\tan \delta_0(k)}{k}. \tag{2.30}$$

As a only includes partial waves with $l = 0$, it is also called s-wave scattering length. For fermions the s-wave scattering length is zero due to the Pauli exclusion principle. Consequently, at low enough temperatures, identical fermions are non-interacting particles.

The s-wave scattering length depends on the details of the interaction potential. But some general properties of a can already be deduced by regarding a simple one-dimensional square well potential as shown in Fig. 2.5. The solution of the Schrödinger equation (2.21) for a box with a width of $r_0 = 1$ and a depth of V_0 is

$$u(r) \propto \begin{cases} \sin\sqrt{2V_0 r^2} & r \leq 1 \\ r - a & r > 1, \end{cases} \tag{2.31}$$

where we have set $\hbar = m_r = 1$ for simplicity. This simple model shows two important features of the scattering length. First, the scattering length is equal to the intersection of the long-range part of the wave function with the r-axis. This gives an intuitive picture of how the scattering changes if the potential changes. Mathematically, we get

$$a = 1 - \frac{\tan\sqrt{2V_0}}{\sqrt{2V_0}}. \tag{2.32}$$

The tangent results in a oscillatory behavior with repetitive singularities. The singularities emerge exactly at the point where a new bound state appears at the top of the potential. This property of the scattering length is independent of the form of the potential. The scattering length changes its sign from minus to plus during the appearance of the new bound state. Comparing these results with the BEC-BCS crossover, we can identify this bound state as the two-body bound state that appears as the interaction parameter $1/k_F a$ crosses zero.

2.2.2 Inelastic Collisions

In the preceding section, the internal structure of the particles has not been considered. Consequently, the kinetic energy is conserved during the scattering process, which is called an elastic collision. Inelastic collisions, on the other hand, take place if the internal structure of the particles, like the spin quantum numbers, changes during the scattering. In most cases internal energy is released and the particles gain kinetic energy. This energy gain often leads to heating or loss of the trapped particles. A change of the spin can also result in losing the particle from a spin dependent trapping potential. Inelastic collisions are often limiting experiments with cold atoms, but on the other hand, they can also be useful for the detection of scattering resonances or the preparation of specific spin states or even molecules. This section will present the most important inelastic scattering processes and discuss their impact on experiments with cold atoms. More details can be found in the literature, for example [21, 31, 46].

Inelastic collisions of two atoms can be characterized by the change of the spin states. The symmetry of the Hamiltonian of the two-atom system results in several conservation rules that restrict the possible changes of the spin quantum numbers. It is therefore useful to start the discussion with the two-atom Hamiltonian

$$H = H_{\text{kin}} + H_{\text{pot}} + H_{\text{hf}} + H_Z + H_{\text{dip}} + H_{\text{so}}. \tag{2.33}$$

The different contributions are the kinetic energy H_{kin}, the potential energy H_{pot} between the two atoms, the hyperfine coupling H_{hf} between the nuclear and electronic spin of each atom, the Zeeman shift H_Z of the atoms in a magnetic field, the magnetic dipole-dipole interaction H_{dip} between the two atoms and the spin-orbit coupling H_{so}. They are discussed in more detail in the following.

The kinetic part H_{kin} describes the relative motion of the two atoms. It does not depend on the spins, but it includes the orbital angular momentum quantum number l. It has already been introduced in the context of elastic scattering in equation (2.21).

The interatomic potential is written as H_{pot}. For the case of two alkali atoms, the potential depends on the separation r and on the relative orientation between the electronic spins. It can be written as

$$H_{\text{pot}} = V_s(r)P_s + V_t(r)P_t, \tag{2.34}$$

where P_s and P_t are projection operators on the singlet and triplet subspaces. There are several parts contributing to the potentials $V_s(r)$ and $V_t(r)$. For small distances r, the Coulomb repulsion between the nuclei dominates. The difference between the singlet (anti-parallel spins) and triplet (parallel spins) potential results from the exchange interaction between the electrons. In case of the singlet spin state, the spatial part of the wave function is symmetric. This increases the negative charge density in between the two nuclei and leads to a stronger binding. The decrease of the electron density for the triplet case weakens the binding. For large distances, the exchange interaction decreases exponentially and the van der Waals (vdW) interaction becomes the dominant part. It is caused by the induced electric dipole interaction between the two atoms and gives

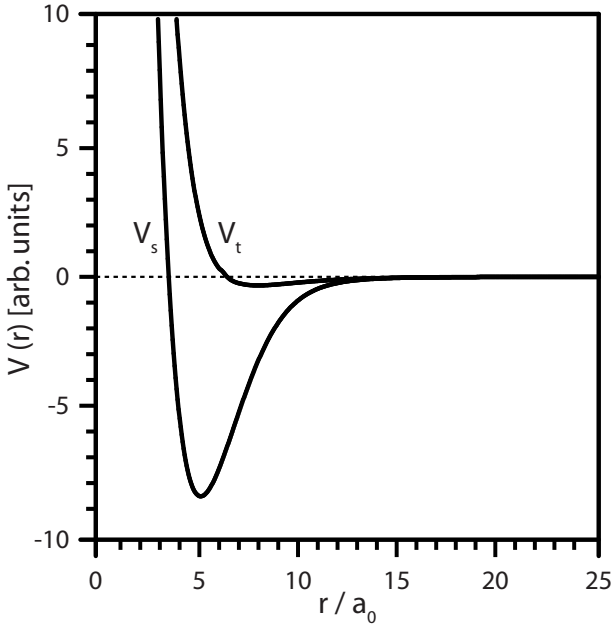

Figure 2.6: Singlet and triplet potential between two ^{6}Li atoms [47]. The radius is plotted in units of the Bohr radius a_0.

rise to an attractive potential. The vdW interaction is typically modelled by the first parts of the multipole expansion

$$V_{\text{vdW}} = -\frac{C_6}{r^6} - \frac{C_8}{r^8} - \frac{C_{10}}{r^{10}} - \dots, \tag{2.35}$$

where $C_{6,8,10}$ are the vdW coefficients. The potentials $V_s(r)$ and $V_t(r)$ are shown in Fig. 2.6 for the example of two ^{6}Li atoms. If the scattering atoms are in a pure singlet or triplet state, only one potential is required to calculate the collision. In this case, the singlet and the triplet potentials will give rise to the two different s-wave scattering lengths a_s and a_t.

The nuclear spin $\vec{i}_j$ of each atom couples to its electronic spin $\vec{s}_j$ and results in the hyperfine interaction Hamiltonian H_{hf}

$$H_{\text{hf}} = \frac{a_{\text{hf},1}}{\hbar^2}\vec{i}_1 \cdot \vec{s}_1 + \frac{a_{\text{hf},2}}{\hbar^2}\vec{i}_2 \cdot \vec{s}_2, \tag{2.36}$$

where $a_{\text{hf},j}$ is the hyperfine coupling constant for the two atoms $j \in \{1, 2\}$. In the case of alkali atoms with a single s-electron, the hyperfine interaction leads to a split ground state with the quantum numbers $f = i \pm s$. The two states are separated by an energy difference of $2a_{\text{hf}}$.

An external magnetic field $\vec{B}$ leads to a Zeeman splitting of the spin states with different projections onto the direction of the field. This interaction is implemented by the Hamiltonian

$$H_Z = \frac{\mu_B}{\hbar}\left(g_s\vec{s}_1 + g_s\vec{s}_2 + g_{i,1}\vec{i}_1 + g_{i,2}\vec{i}_2\right)\vec{B}, \tag{2.37}$$

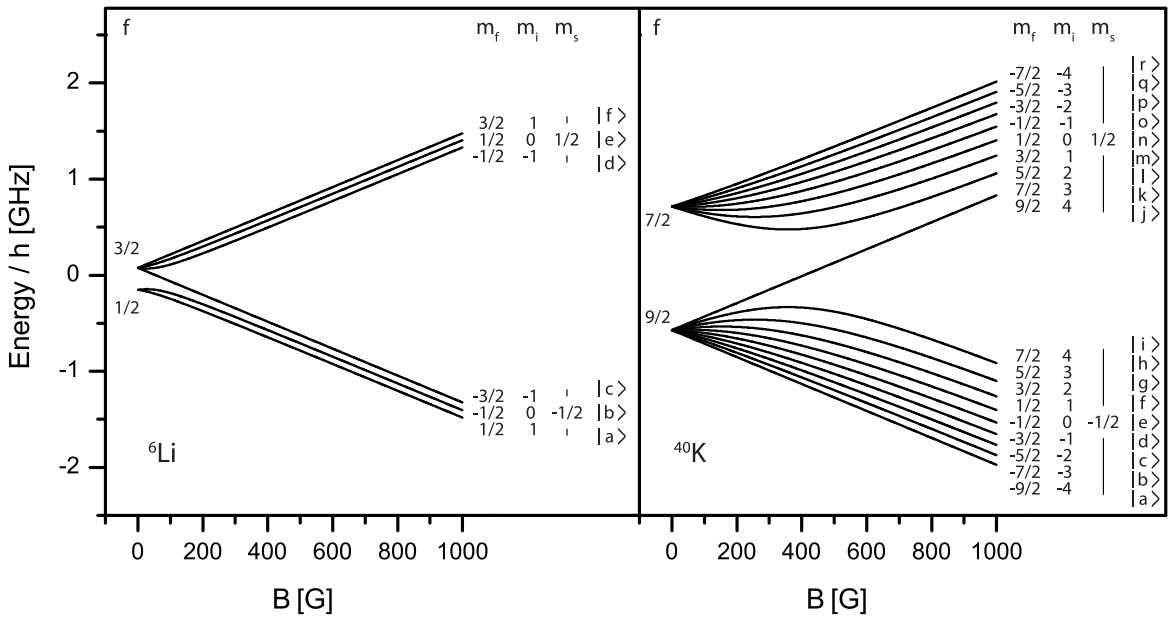

Figure 2.7: Zeeman splitting of the hyperfine states of ^{6}Li and ^{40}K with the quantum numbers f, m_f, m_i and m_s. Note the inverse hyperfine structure of ^{40}K compared to ^{6}Li. Labelling the states with $|a\rangle, |b\rangle, |c\rangle$... in order of increasing energy is used as a simple and useful notation.

where μ_B is the Bohr magneton and g_s ($g_{i,j}$) is the Landé factor for the electron (nucleus). In case of the alkali metals, the energy levels can be calculated analytically with the Breit-Rabi formula

$$\begin{aligned} E(B, m_f) &= \frac{2a_{\text{hf}}}{2(2i+1)} + m_f g_i \mu_B B \\ &\pm a_{\text{hf}} \sqrt{1 + \frac{4m_f}{2i+1}\frac{\mu_B(g_s - g_i)}{2a_{\text{hf}}}B + \left(\frac{\mu_B(g_s - g_i)}{2a_{\text{hf}}}B\right)^2}, \end{aligned} \tag{2.38}$$

for $m_f \in \{-f, \ldots, f\}$ and $f = i \pm 1/2$. The energy for the different Zeeman states for ^{6}Li and ^{40}K are shown in Fig. 2.7 together with the magnetic quantum numbers m_f, m_i and m_s. Figure 2.7 also introduces a useful method to label the states with $|a\rangle, |b\rangle, |c\rangle$... in order of increasing energy.

The next part of the Hamiltonian is the magnetic dipole-dipole interaction

$$H_{\text{dip}} = \frac{\mu_0 \mu_B^2}{\pi}\frac{1}{r^3}\left(\vec{s}_1 \cdot \vec{s}_2 - \frac{(\vec{s}_1 \cdot \vec{r})(\vec{s}_2 \cdot \vec{r})}{r^2}\right). \tag{2.39}$$

It depends on the relative orientation between the electronic spins and the axis between the two atoms. Therefore and in contrast to the contributions discussed above, it has no spherical symmetry.

A similar term is the spin orbit coupling

$$H_{\text{so}} = -C\mathrm{e}^{-\frac{r}{r_{\text{so}}}} \left(\vec{s}_1 \cdot \vec{s}_2 - \frac{(\vec{s}_1 \cdot \vec{r})(\vec{s}_2 \cdot \vec{r})}{r^2} \right) \tag{2.40}$$

with C and r_{so} being positive constants, which can be determined numerically [48, 49]. It has the same spin structure but a different radial dependence and the opposite sign as the dipole-dipole contribution (2.39).

After having introduced the two-atom Hamiltonian (2.33), we can deduce different categories of inelastic scattering. If the two atoms are far apart and non-interacting, their eigenstate can be expressed by the product of the individual atomic eigenstates. For small magnetic fields where the hyperfine coupling (2.36) dominates the Zeeman shift (2.37), $\{f_1, m_{f,1}, f_2, m_{f,2}, l, m_l\}$ is a suitable set of quantum numbers. l and m_l are the orbital momentum quantum numbers. In a high magnetic field, the electronic and nuclear spins are decoupled and $\{m_{s,1}, m_{i,1}, m_{s,2}, m_{i,2}, l, m_l\}$ are good quantum numbers. The possibility of inelastic collisions now arises, because the interaction within the interatomic potential does not conserve any complete set of quantum numbers. A collision between two atoms will result in a superposition of different eigenstates. The symmetries of the different parts of the Hamiltonian (2.33) determine the possible couplings between the states.

In many cases, the dipolar interactions H_{dip} and H_{so} are small and can be neglected. In this case, the only remaining part that couples the spins of the two atoms is the exchange interaction contained in H_{pot}. It couples the singlet and triplet states. Consequently, the two-atom system is described using the sum of the electronic spins $S = s_1 + s_2$ and the sum of the nuclear spins $I = i_1 + i_2$. But due to the hyperfine coupling between the electronic and nuclear spins, only $F = S + I$ and its projection quantum number m_F are conserved quantities during a collision. In the presence of a magnetic field, the Zeeman interaction H_Z breaks the spherical symmetry and only m_F remains a conserved quantum number. This leads to so-called spin-exchange collisions. Two atoms with initial quantum numbers $\{m_{f,1}, m_{f,2}\}$ can couple to a final state with $\{m_{f,1} \pm 1, m_{f,2} \mp 1\}$ if the process is energetically allowed. The released energy is typically much larger than the trapping potential and the atoms are lost after the collision. For alkali atoms, typical collision rates are of order of $10^{-11}\text{cm}^3\text{s}^{-1}$. As the densities of the samples are often larger than 10^{11}cm^{-3}, spin-exchange collisions can destroy the trapped sample within less than one second. Therefore, it is crucial to prepare the atoms in hyperfine states, which do not allow for exothermic spin-exchange collisions. The requirements for ^{6}Li-^{40}K mixtures are discussed in the next section 2.2.3.

A second type of inelastic collisions is induced by the dipolar interactions H_{dip} and H_{so}. They couple the angular momentum of the two atoms with the spin part. A detailed calculation shows that transitions with $\Delta l \in \{0, \pm 2\}$ and $\Delta(m_l + m_F) = 0$ are possible [21, 31]. The typical rates for these dipolar collisions are on the order of $10^{-15}\text{cm}^3\text{s}^{-1}$. Therefore, dipolar collisions may not be limiting the lifetime of the trapped samples, even if they are allowed by the selection rules.

Another kind of inelastic collisions are three-body collisions. They are not described by the two-body Hamiltonian, but they are very important in the context of molecular quantum gases. Two scattering atoms cannot form a molecule with a binding energy $E_B < 0$, as energy and momentum conservation cannot be fulfilled simultaneously for this process. But if a third atom participates in the collision, the formation of a dimer molecule becomes possible. This process can lead to atom loss, if the released energy is larger than the trapping potential. But if the binding energy is small enough, the atoms and molecules stay trapped and the three body collision is a possible way to create a cloud of weakly bound molecules.

The binding energy is converted into kinetic energy of the newly formed molecule and the single atom following the equation

$$0 = E_B + \frac{1}{2}(m_1 + m_2)v_m^2 + \frac{1}{2}m_3 v_a^2, \tag{2.41}$$

where we consider three atoms $j \in \{1, 2, 3\}$ with different masses m_j and the velocities v_m of the molecule and v_a of the atom after the collision. The initial kinetic energy of the particles has been neglected. Momentum conservation leads to

$$0 = (m_1 + m_2)v_m + m_3 v_a. \tag{2.42}$$

Combining both equations, the ratio between the kinetic energies of the molecule and the atom after the collision is easily calculated as

$$\frac{E_{\text{kin},m}}{E_{\text{kin},a}} = \frac{m_3}{m_1 + m_2}. \tag{2.43}$$

If only one species with mass $m_1 = m_2 = m_3$ is present, the molecule gains one third of the binding energy while the remaining atoms gains the other two thirds. If two different species are present and a heteronuclear molecule with mass $m_1 + m_2$ is formed, this dimer still gets less energy than the single atom with the mass $m_3 = m_1$ or $m_3 = m_2$. This important matter of fact supports the trapping of the molecules during the formation process.

The three-body collisions discussed above are useful to create molecules in weakly bound states. On the other side, a collision of the molecule with an atom or another molecule can release energy by transferring the molecule into a deeper bound state. This energy is much larger than available trapping potentials. Consequently, these three or four-body collisions can lead to a loss of trapped molecules. The rate constants for atom-dimer or dimer-dimer collisions depend on the scattering length and the statistical properties of the atoms. As the formation of molecules requires a weakly bound state, the scattering length will be very large and lead to strongly enhanced destructive atom-dimer and dimer-dimer collisions. For molecules made of bosons, their lifetime within an ultracold cloud is too short for most experiments[4]. If fermionic atoms are used to form bosonic molecules, the Pauli principle suppresses the atom-dimer and

[4]Using optical lattices prevents the molecules from colliding and lifetimes up to 700 ms have been reached with $^{87}Rb_2$ molecules [50].

dimer-dimer collisions. For such collisions, at least three particles have to come close together, with two of them being identical fermions in the same spin state. In the case of weakly bound molecules with large inter-atomic distances, Petrov et al. have calculated a strong decrease of the collision rate with increasing scattering length [51, 52]. This work was extended to heteronuclear molecules in [53]. The suppressive effect of the Pauli principle decreases for an increasing mass ratio up to $m_1/m_2 = 12.33$. In the case of homonuclear molecules, lifetimes on the order of 1 s ($^6Li_2$) [54] and 100 ms ($^{40}K_2$) [55] are possible. This made the quantum-degenerate regime accessible for these bosonic dimers [23, 56].

2.2.3 Lithium Potassium Collisions

This section treats the different collision properties discussed above in the special case of ^{6}Li-^{40}K mixtures. Interactions between ultracold ^{6}Li and ^{40}K atoms have not been studied before the work presented in this thesis. Therefore, many important properties like the interspecies scattering length were not known during the design of the experimental setup. We will restrict the discussion of this section to the basic qualitative interaction properties related to the spin structure of the atoms. The new results based on our experiments will be presented in chapter 5.

First, we will discuss spin-exchange collisions between ^{6}Li and ^{40}K in a magnetic field. They are characterized by the conservation of $m_F = m_{f,^6\mathrm{Li}} + m_{f,^{40}\mathrm{K}}$. ^{40}K has an inverted hyperfine structure as shown in Fig. 2.7. This is due to the nuclear magnetic moment being parallel to the nuclear spin, which is the opposite of the situation in all other natural occurring alkali isotopes. Consequently, the most favorable kind of exothermic spin-exchange collision is the case where both colliding atoms with initial quantum numbers $\{m_{f,^6\mathrm{Li}}, m_{f,^{40}\mathrm{K}}\}$ are transferred into the next lower lying Zeeman energy level with $\{m_{f,^6\mathrm{Li}} + 1, m_{f,^{40}\mathrm{K}} - 1\}$. But if either ^{6}Li or ^{40}K already is in the lowest level ($m_{f,^6\mathrm{Li}} = 1/2$ or $m_{f,^{40}\mathrm{K}} = -9/2$) and the other atom is in any state of the lower branch of Zeeman levels ($f_{^6\mathrm{Li}} = 1/2$ and $f_{^6\mathrm{Li}} = 3/2, m_{f,^6\mathrm{Li}} = -3/2$ or $f_{^{40}\mathrm{K}} = 9/2$), exothermic spin-exchange collisions are forbidden. This results in 12 different spin combinations that are stable against spin-exchange collisions.

There are even possibilities for stable combinations with three different spin states. Two of these possibilities are of special importance. First, having ^{6}Li atoms in the two lowest Zeeman levels with $m_{f,^6\mathrm{Li}} = 1/2$ and $m_{f,^6\mathrm{Li}} = -1/2$ together with ^{40}K in its lowest level with $m_{f,^{40}\mathrm{K}} = -9/2$ gives a mixture stable against spin-exchange collisions. The second possibility is to have two components of ^{40}K in its lowest two level with $m_{f,^{40}\mathrm{K}} = -9/2$ and $m_{f,^{40}\mathrm{K}} = -7/2$ together with the lowest ^{6}Li state.

The initial preparation of the trapped atoms typically consists of a spin mixtures with $f_{^6\mathrm{Li}} = 1/2$ and $f_{^{40}\mathrm{K}} = 9/2$ (see section 4.2.2 for technical details). The exothermic spin-exchange collisions can now increase the population of the lower lying Zeeman levels. As ^{6}Li is only present in the two lowest spin states, spin-exchange relaxation is restricted to collisions with $m_{f,^6\mathrm{Li}} = -1/2$ and the ^{40}K states with $m_{f,^{40}\mathrm{K}} \neq -9/2$. In the case of a large enough reservoir of ^{6}Li atoms, the mixture will finally end up in a stable three component mixture with $m_{f,^6\mathrm{Li}} =$

$\pm 1/2$ and $m_{f,^{40}\mathrm{K}} = -9/2$. This is a very favorable starting point for experiments. Therefore, it is interesting to calculate the released energy of this spin relaxation process. The energy difference $E_{\mathrm{relax}}(B) = E_{^6\mathrm{Li}}(B) + E_{^{40}\mathrm{K}}(B)$ between the Zeeman levels is distributed among the two atoms fulfilling energy and momentum conservation. Assuming initial zero kinetic energy for simplicity, we get the final kinetic energies

$$\begin{aligned} E_{\mathrm{kin},^6\mathrm{Li}}(B) &= \frac{m_{^{40}\mathrm{K}}}{m_{^6\mathrm{Li}} + m_{^{40}\mathrm{K}}} E_{\mathrm{relax}}(B) = \frac{40}{46} E_{\mathrm{relax}}(B) \approx 0.87\, E_{\mathrm{relax}}(B) \\ E_{\mathrm{kin},^{40}\mathrm{K}}(B) &= \frac{m_{^6\mathrm{Li}}}{m_{^6\mathrm{Li}} + m_{^{40}\mathrm{K}}} E_{\mathrm{relax}}(B) = \frac{6}{46} E_{\mathrm{relax}}(B) \approx 0.13\, E_{\mathrm{relax}}(B). \end{aligned} \tag{2.44}$$

The ^{40}K atom only gets 13% of the relaxation energy. Therefore, under certain conditions, the ^{40}K atoms may still be trapped while the ^{6}Li atoms leave the trap and take away most kinetic energy. We assume a trap depth of $k_B \times 1$ mK corresponding to $h \times 21$ MHz. Consequently, the maximum relaxation energy that would not lead to loss of the ^{40}K atom would be $h \times 21/0.13$ MHz $= h \times 162$ MHz. Regarding the energy splitting of the Zeeman levels in Fig. 2.7, the relaxation energy stays below 162 MHz for magnetic fields below ≈ 200 G for the relevant spin combinations in the lower branches. Heteronuclear spin-exchange collisions can therefore be used to prepare a pure sample of ^{40}K in the absolute ground state together with ^{6}Li in the two lowest Zeeman states. If the excess trap depth for ^{40}K is large enough for a given magnetic field, the ^{40}K atoms are not lost during the relaxation. For experimental conditions with finite tempereture, the thermal energy needs to be added to the relaxation energy. Fortunately, infrared optical dipole traps are deeper for ^{40}K than for ^{6}Li. This additional depth supports the trapping of the ^{40}K atoms after the relaxation. However, a larger amount of ^{6}Li atoms is lost because every ^{40}K atom can require several spin relaxations depending on the initial Zeeman state and each transition is accompanied by one ^{6}Li spin relaxation.

If spin-exchange collisions are forbidden, the dominating part of inelastic collisions is due to dipolar collisions or three-body collisions. Only the absolute ground state with $m_{f,^6\mathrm{Li}} = 1/2$ and $m_{f,^{40}\mathrm{K}} = -9/2$ is stable against dipolar relaxation. However, in most cases of other alkali atoms, the dipolar processes are weak enough not to limit the lifetime of the trapped atoms.

The three-body collisions leading to molecule formation can be analyzed in a similar way to spin relaxation. Instead of the relaxation energy, the binding energy of the molecule is released and the final particles are one molecule and one atom. For ^{6}Li-^{40}K mixtures, the following combinations are possible:

These numbers may play an important role, if the molecule formation takes place in a shallow trap. Especially in the cases where the binding energy is predominately transferred to one particle, this particle (atom or molecule) can be lost from the trapping potential. Of course, the different potential depths of an optical dipole trap for ^{6}Li, ^{40}K and the diatomic molecules affect the situation.

$$
\begin{aligned}
{}^6\mathrm{Li} + {}^6\mathrm{Li} + {}^6\mathrm{Li} &\longrightarrow {}^6\mathrm{Li}_2(0.33\,E_B) + {}^6\mathrm{Li}(0.67\,E_B)\\
{}^{40}\mathrm{K} + {}^{40}\mathrm{K} + {}^{40}\mathrm{K} &\longrightarrow {}^{40}\mathrm{K}_2(0.33\,E_B) + {}^{40}\mathrm{K}(0.67\,E_B)\\
{}^6\mathrm{Li} + {}^6\mathrm{Li} + {}^{40}\mathrm{K} &\longrightarrow {}^6\mathrm{Li}_2(0.77\,E_B) + {}^{40}\mathrm{K}(0.23\,E_B)\\
{}^6\mathrm{Li} + {}^6\mathrm{Li} + {}^{40}\mathrm{K} &\longrightarrow {}^6\mathrm{Li}{}^{40}\mathrm{K}(0.12\,E_B) + {}^6\mathrm{Li}(0.88\,E_B)\\
{}^6\mathrm{Li} + {}^{40}\mathrm{K} + {}^{40}\mathrm{K} &\longrightarrow {}^{40}\mathrm{K}_2(0.07\,E_B) + {}^6\mathrm{Li}(0.93\,E_B)\\
{}^6\mathrm{Li} + {}^{40}\mathrm{K} + {}^{40}\mathrm{K} &\longrightarrow {}^6\mathrm{Li}{}^{40}\mathrm{K}(0.47\,E_B) + {}^{40}\mathrm{K}(0.53\,E_B)
\end{aligned}
$$

2.3 Feshbach Resonances

Magnetic Feshbach resonances are an important tool for experiments with ultracold atoms. These resonances allow to tune the *s*-wave scattering length between two atoms by simply changing the external magnetic field. This does not only alter the collision properties of the atoms. In the case of fermions, Feshbach resonances allow to access the BEC-BCS crossover, which was discussed in section 2.1.2. The physics of Feshbach resonances in ultracold gases was reviewed recently in [57, 24]. This section will first present the basic concepts of Feshbach resonances. Afterwards, we will present a model that allows to calculate the magnetic field positions of Feshbach resonances. Finally, we will give an overview of the well-known homonuclear Feshbach resonances of ^{6}Li and ^{40}K.

2.3.1 Basic Theory of Feshbach Resonances

A Feshbach resonance is a resonance of the scattering length between two atoms. Such a resonance occurs, if a new bound state becomes energetically accessible by tuning an external parameter such as a magnetic field. It is also possible to use optical fields to tune the scattering length [58], but these so-called optical Feshbach resonances will not be discussed within this thesis.

In section 2.2.1, we have shown how the scattering length depends on the location of the last bound state of an interaction potential. If the potential is changed and the last bound state disappears (or a new one appears), the scattering length diverges and changes from plus to minus (minus to plus) infinity. But for particles without internal spin structure, the variation of the potential is not possible experimentally.

In the case of particles with an internal spin structure, the interaction potential depends on the spin state of the two-atom system and therefore also on an external magnetic field. The details of this potential are found in equation (2.33) and the related discussion in the last section. Tuning the magnetic field will shift the bound states of the potential relative to their zero-field position. The shift depends on the magnetic moment of the two-atom spin state. Consequently, the energy level of one bound state can cross the scattering energy of the two colliding atoms. If

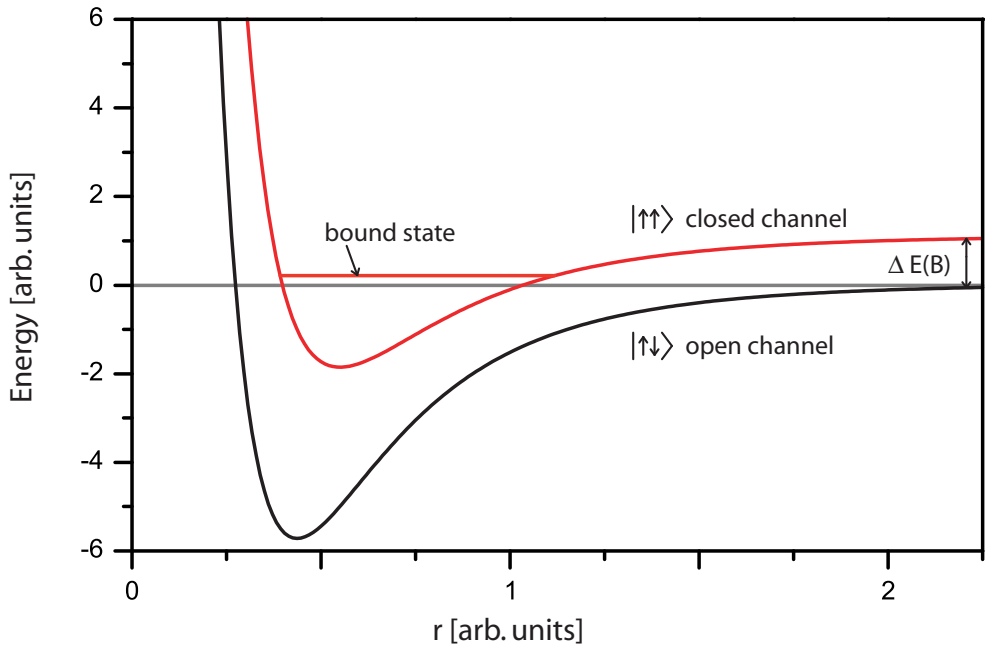

Figure 2.8: Illustration of a Feshbach resonance. Two colliding atoms in the open channel can couple to a bound state of the closed channel. The separation between the two channels can be varied with an external magnetic field. The Feshbach resonance occurs, if the the bound state crosses the dissociation energy of the open channel.

the scattering wave function of the two atoms can couple to the bound state, the scattering length diverges and a Feshbach resonance occurs.

A simplified picture to illustrate a Feshbach resonance is shown in Fig. 2.8. The colliding atoms are prepared in an initial spin state symbolized by $|\uparrow\downarrow\rangle$. The different spin state combinations of the separated atoms are called channels. The initial channel of the colliding atoms is called the open channel. If the asymptotic energy of the potential at large interatomic distances r is larger than the total energy, the channel is called a closed channel. The atoms cannot leave the collision in a closed channel because of energy conservation. In our example, the atoms have zero kinetic energy and the total energy coincides with the open potential for large interatomic distances. For a different spin state $|\uparrow\uparrow\rangle$ another potential exists with a different asymptotic energy $\Delta E(B)$. This distance depends on the external magnetic field B. By shifting the potentials against each other, a bound state of the closed channel can become resonant to the asymptotic energy of the open channel. This causes a Feshbach resonance, if the bound state can couple to the spin state of the open channel.

Although this simple picture is very intuitive and used frequently, it is important to understand its limits. A finite coupling between the open channel and the bound state of the closed channel means, that the initial spin state $|\uparrow\downarrow\rangle$ is no eigenstate at closer distances. Therefore, the two-atom wave function is projected onto the two subspaces belonging to the two potentials. This

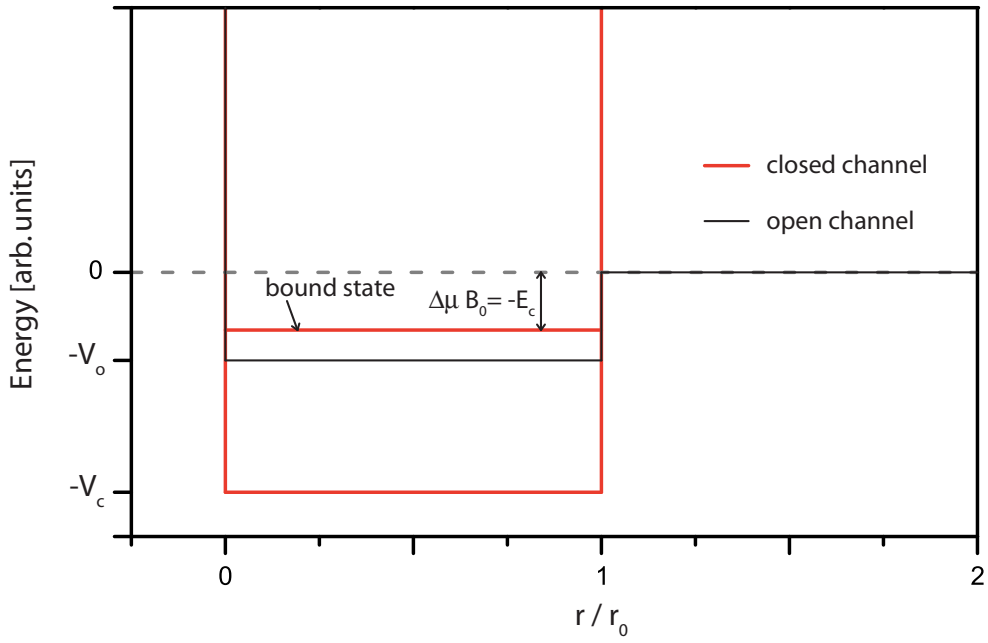

Figure 2.9: Box potentials used in the Feshbach resonance model. Shown are the two box potentials as described in equation (2.45).

coupling between the two subspaces also changes the character of the bound state. It cannot be attributed only to the closed channel potential as the picture in Fig. 2.8 might suggest. The bound state is an eigenstate of the entire interaction Hamiltonian as the coupling between the different channels is necessary for the resonance. However, the distribution of the wave function of the bound state among the subspaces of the open and closed channels is an important characteristic for the Feshbach resonance as we will discuss further below.

Many details of Feshbach resonances can be understood by using a model of two coupled square-well potentials. These potentials allow to calculate analytical results. The following example is based on references [24, 59]. Similar examples can be found in [60, 61]. We use the two square well potentials

$$\begin{aligned} V_o(r) &= -V_o\Theta(r_0 - r) \\ V_c(r) &= -V_c\Theta(r_0 - r) + V_\infty\Theta(r - r_0), \end{aligned} \tag{2.45}$$

where $\Theta(x)$ is the Heaviside step function. The potentials are shown in Fig. 2.9.

The two potentials could be regarded as the singlet and triplet potential introduced in equation (2.34). However, for simplicity we will treat the current example without attributing real potentials or interactions. The second potential, together with its bound states can be shifted by applying a magnetic field B by the energy $\Delta\mu B$, where $\Delta\mu > 0$ is analogue to the difference of the magnetic moments. Introducing a weak coupling energy $V_{oc}(r) = V_{oc}\Theta(r_0 - r)$ with

$V_{oc} \ll |V_o - V_c|$ leads to the following Schrödinger equation for the model system:

$$\begin{pmatrix} -\frac{\hbar^2\nabla^2}{2m_r} + V_o(r) - E & V_{oc} \\ V_{oc} & -\frac{\hbar^2\nabla^2}{2m_r} + V_c(r) + \Delta\mu B - E \end{pmatrix} \begin{pmatrix} \Psi_o(r) \\ \Psi_c(r) \end{pmatrix} = 0. \tag{2.46}$$

Again, the coupling V_{oc} could express different interactions like hyperfine or dipole coupling. This example will make no specific choice but note that we assume V_{oc} to vanish for $r > r_0$. Using box potentials, the Schrödinger equation can be fully solved analytically. Without loss of generality, we set $V_\infty \to \infty$ to simplify the results. We will not provide detailed calculations here to be able to concentrate the discussion on the important outcomes in the context of Feshbach resonances.

First, the properties of the uncoupled potentials with $V_{oc} = 0$ should be specified. The Hamiltonian is diagonal and the two potentials can be treated independently. For zero energy E and a finite magnetic field $B > 0$, only the first potential has a solution $\Psi_o(r)$ that is described by the standard scattering theory discussed in section 2.2.1. This will give a scattering length a_{bg} depending on the size of the box. Changing the magnetic field does not affect $\Psi_o(r)$ or a_{bg}. But the second potential is shifted to different energies. The depth of the potential V_c is related to the energy of the bound state $E_c(B = 0) < 0$ that will cause the Feshbach resonance. For $\Delta\mu B_0 = -E_c(B = 0)$, the bound state energy becomes zero: $E_c(B = B_0) = 0$. Note, that the bound state is shifted proportional to the magnetic field.

To discuss the influence of the coupling V_{oc}, we can now solve the Schrödinger equation. As the potentials only involve box-like functions, the solution can be constructed using a suitable combination of trigonometrical and exponential functions. For $E > 0$, the open channel wave function Ψ_o will show an oscillating behavior outside the box for $r > r_0$. The boundary conditions at $r = r_0$ will introduce a phase shift and the related scattering length. As the solution of Ψ_o is coupled to the closed channel solution Ψ_c inside the box for $r < r_0$, the scattering length depends on the closed channel and especially on the location of its bound state. An illustration of the scattering length is shown in Fig. 2.10.

We can identify several important parameters of a Feshbach resonance. The shape of the resonance is given by its location B_{res}, the background scattering length a_{bg} and the width $\Delta B = B_{\text{res}} - B_{\text{zero}}$, where B_{zero} is the zero crossing of the scattering length. The analytical form of the scattering length around the resonance is given by

$$a(B) = a_{\text{bg}} \left(1 - \frac{\Delta B}{B - B_{\text{res}}}\right). \tag{2.47}$$

The behavior of the scattering length does not characterize a Feshbach resonance sufficiently. The second important parameter is the bound state. The energy of the uncoupled bound state in the closed channel E_c as well as the energy E_b of the coupled case is also shown in Fig. 2.10. The zero crossing of E_b coincides with the resonance of the scattering length at B_{res} and is shifted by δB away from the zero crossing of E_c at B_0. Furthermore, E_b does not vary linearly but quadratically with B around the Feshbach resonance.

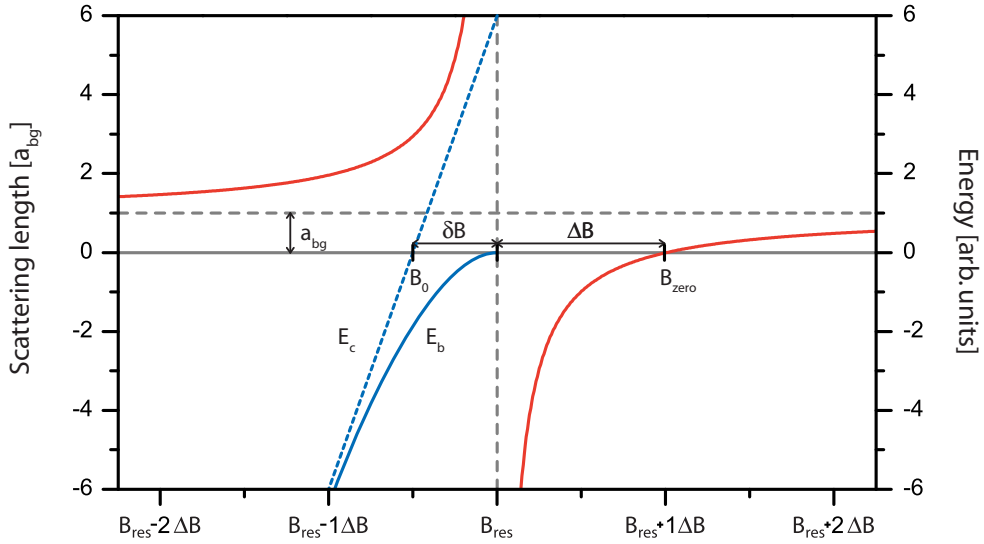

Figure 2.10: Scattering length and bound state energy around a Feshbach resonance. The scattering length (red line) diverges at the resonance position B_{res} and has a width of ΔB towards its zero crossing at B_{zero}. The energy of the bound state E_b (solid blue line) behaves quadratically close to the resonance position where it vanishes. The bound state energy of the uncoupled closed channel E_c (dashed blue line) changes linearly and crosses zero at the field B_0.

These properties should now be related to the model parameters. The background scattering length is only determined by the open channel potential. If we express the scattering length in units of r_0, it is only a function of V_o. The closed channel potential defines the zero crossing of the bound state at B_0 in the uncoupled case. Although the resonance position is shifted due to the coupling, we can consider V_c to define the resonance position. The remaining two parameters V_{oc} and $\Delta\mu$ define the width ΔB and the shift δB by the formulas [24]

$$\Delta B = \frac{1}{\Delta\mu}\frac{(1-a_{\text{bg}}/r_0)^2}{a_{\text{bg}}/r_0}\frac{2V_cV_{oc}^2}{(V_o-V_c)^2} \quad \text{and} \tag{2.48}$$

$$\delta B = \Delta B\frac{a_{\text{bg}}/r_0}{1-a_{\text{bg}}/r_0}. \tag{2.49}$$

Within the context of using Feshbach resonances for studying the BEC-BCS crossover, another property is important. The BEC-BCS crossover regime requires a weakly bound state on the BEC side of the resonance. But the bound state of the coupled channel model has a weakly bound contribution from the open channel, while it has a deeply bound contribution from the closed channel. This is reflected by the magnetic field dependance, which is linear or quadratic. Therefore, only the magnetic field range within the resonance in which the bound state projection onto the open channel is close to one is suitable to simulate the BEC-BCS crossover. A suitable parameter to describe the size of this region is the rate ζ^{-1} of the increasing closed channel

fraction Z if B deviates from the resonance position [24]

$$\lim_{a\to\infty} Z = \frac{1}{\zeta}\left|\frac{B - B_{\text{res}}}{\Delta B}\right| \tag{2.50}$$

For the box potential model, we get [24]

$$\zeta = \frac{\mu_B}{\hbar^2} a_{\text{bg}}^2 \Delta\mu \Delta B. \tag{2.51}$$

For $\zeta \ll 1$, the bound state is of open channel character only for a small fraction of the resonance width ΔB. Such resonances are called closed channel dominated. If $\zeta > 1$, the weakly bound state character persists over a large range of the resonance width and the resonance is called open channel dominated. The binding energy varies quadratically and the Feshbach resonance has the character required for the BEC-BCS crossover. It is important to note, that ζ and the width ΔB are related but different parameters. Most broad ($\Delta B \geq 1$ G) Feshbach resonances found so far are open channel dominated and most small resonances are closed channel dominated [24]. But suitable values of the background scattering length or the difference of the magnetic moments can also lead to broad closed channel or narrow open channel dominated Feshbach resonances.

To summarize, the most important parameters describing a Feshbach resonance are the position B_{res}, the width ΔB, the background scattering length a_{bg}, the zero crossing of the uncoupled closed channel B_o and ζ characterizing the open/closed channel character. The full assignment of a Feshbach resonance is usually done by using the quantum numbers of the open and closed channel. This also includes the angular momentum quantum numbers l_o and l_c of each channel. Parity conservation requires $|l_0 - l_c|$ to be even. A precise assignment requires both quantum numbers. But in the context of ultracold gases, collisions with higher partial waves are strongly suppressed and usually $l_o \in \{0, 1\}$. In this case, Feshbach resonances are often called *s*-wave, *p*-wave, *d*-wave and so on using only their closed channel quantum number $l_c = 0, 1, 2, ...$

2.3.2 The Asymptotic Bound State Model

The box potential model is very useful to understand the physics of a single Feshbach resonance. But it does not give insight into the structure of the many Feshbach resonances two specific atoms can have in dependence of the magnetic field. Their theoretical description requires a more detailed knowledge about the interatomic potentials and the interaction properties. In the following, we will present the asymptotic bound state model (ABM) [62] to calculate the positions of Feshbach resonances. This model is especially suited to assign experimentally determined Feshbach resonances. It is based on earlier work [63, 64] and has been extended by Tobias Tiecke, Servaas Kokkelmans and Jook Walraven [62] in the context of assigning the ^{6}Li^{40}K Feshbach resonances presented in this thesis.

The asymptotic bound state model is based on diagonalizing the Hamiltonian

$$H_{\text{ABM}} = H_{\text{kin}} + H_{\text{pot}} + H_{\text{hf}} + H_Z \tag{2.52}$$

by using several approximations. This results in the energies of the bound states of all closed channels for two given atoms. Within the ABM, Feshbach resonances occur, if the energy of a bound channel coincides with the energy of the two free atoms in the open channel. Additionally, the quantum number m_F must be identical for the two channels to couple both states. The solution $|\Psi\rangle$ of the Schrödinger equation with the ABM Hamiltonian are of the form

$$|\Psi\rangle = |R_{S,l}\rangle|Y_{l,m}\rangle|S, m_S, m_{i,1}, m_{i,2}\rangle, \tag{2.53}$$

where $|R_{S,l}\rangle$ is the radial part, $|Y_{l,m}\rangle$ is the angular part and $|S, m_S, m_{i,1}, m_{i,2}\rangle$ is the spin part.

By rewriting the hyperfine interaction

$$\begin{aligned} H_{\text{hf}} &= \frac{a_{\text{hf},1}}{\hbar^2}\vec{i}_1 \cdot \vec{s}_1 + \frac{a_{\text{hf},2}}{\hbar^2}\vec{i}_2 \cdot \vec{s}_2 && (2.54)\\ &= \left(\frac{a_{\text{hf},1}}{2\hbar^2}\vec{i}_1 + \frac{a_{\text{hf},2}}{2\hbar^2}\vec{i}_2\right)(\vec{s}_1 + \vec{s}_2) + \left(\frac{a_{\text{hf},1}}{2\hbar^2}\vec{i}_1 - \frac{a_{\text{hf},2}}{2\hbar^2}\vec{i}_2\right)(\vec{s}_1 - \vec{s}_2) && (2.55)\\ &= V_{\text{hf}}^{+} + V_{\text{hf}}^{-}, && (2.56) \end{aligned}$$

we identify two parts $V_{\text{hf}}^{\pm}$, which conserve (V_{hf}^{+}) or mix (V_{hf}^{-}) the singlet and triplet subspaces.

This leads to the following matrix elements of the ABM Hamiltonian in the spin subspace

$$\langle S', m_S', m_{i,1}', m_{i,2}'|E_{S,l} + V_{\text{hf}}^{+} + V_{\text{hf}}^{-}\langle R_{S',l}|R_{S,l}\rangle + H_Z|S, m_S, m_{i,1}, m_{i,2}\rangle. \tag{2.57}$$

Here, we have introduced the energies $E_{S,l}$ of the last bound state of the singlet ($S = 0$) or triplet ($S = 1$) potentials. The precise location of these energies determines the position of the Feshbach resonances. Unfortunately, in many cases the knowledge of the potentials V_s and V_t is not accurate enough to allow to calculate these energies with the required precision. The asymptotic bound state model uses these $2(l + 1)$ variables as free parameters to fit the resonance positions of the model to experimental observations. This method does not require any knowledge of the potential shape. However, the C_6 coefficients of the van-der-Waals potentials can be used to determine the energy spacing between the bound states for different angular momenta l. This reduces the number of free parameters to the two values $E_{S,l=0}$.

All the other contributions to the matrix elements can be easily calculated with the following exception. The overlap integral $\langle R_{S',l}|R_{S,l}\rangle$ between the radial wave functions would also require the solution of the Schrödinger equation within the potential. Two possibilities exist to circumvent this problem. In the case of ^{6}Li^{23}Na Feshbach resonances [64] for example, the full contribution $V_{\text{hf}}^{-}\langle R_{0,l}|R_{1,l}\rangle$ could be neglected. This is a valid approximation if the singlet-triplet spacing is much larger than the mixing: $E_0 - E_1 \gg V_{\text{hf}}^{-}\langle R_{0,l}|R_{1,l}\rangle$. The asymptotic bound state model approximates the overlap as $\langle R_{S',l}|R_{S,l}\rangle = 1$. The bound states responsible for Feshbach resonances usually are the last bound states of the potentials. Consequently, a large part of their wave function is located within the long range asymptote of the potential. As the asymptotic part for the singlet and triplet potentials are equal, the overlap integral is very close to unity in this situation[5].

[5]For ^{6}Li^{40}K the values are 0.979 for $l = 0$ and 0.965 for $l = 1$ [62].

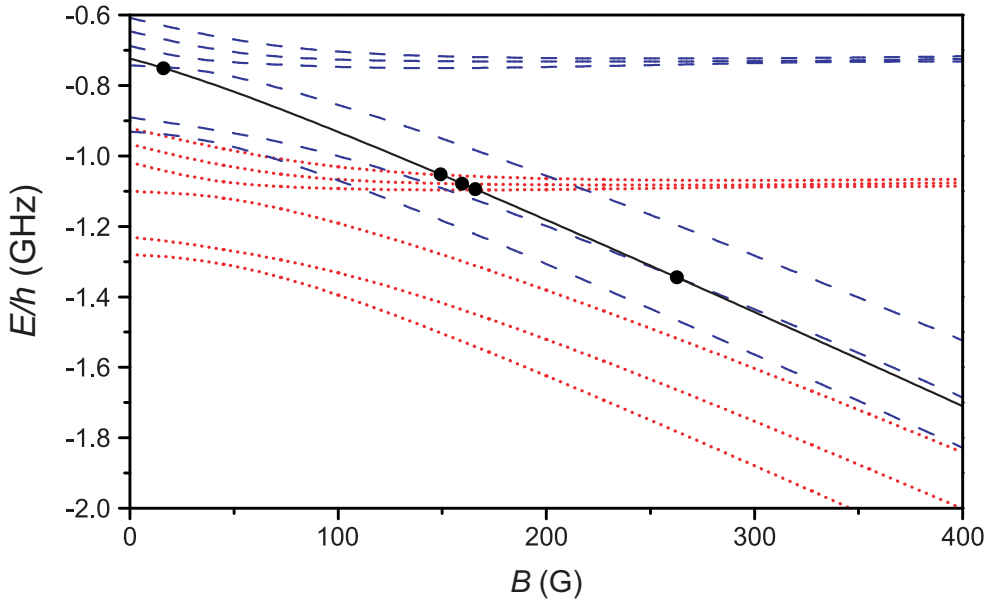

Figure 2.11: Solutions of the asymptotic bound state model for the ^{6}Li$|a\rangle$-^{40}K$|b\rangle$ channel with $m_F = -3$ [65]. Shown are the bound state energies for $l = 0$ (dotted red lines) and $l = 1$ (dashed blue lines). The Feshbach resonances (black dots) occur at the crossings with the open channel energy (solid black line).

These models allow for a very intuitive understanding of the pattern of Feshbach resonances for specific mixtures. The bound states of the two-atom system can be calculated by diagonalizing matrix (2.57). The energy of the open channel atoms is given by the sum of the two Breit-Rabi formulas for the two atoms. Feshbach resonances now occur, if the open channel energy intersects with the energy of a bound state of equal m_F. To visualize the model, Fig. 2.11 shows the Feshbach resonances between ^{6}Li$|a\rangle$ and ^{40}K$|b\rangle$ with $m_F = -3$ discovered during the work of this thesis. The bound state energies are shown for $l = 0$ (dotted red lines) and for $l = 1$ (dashed blue lines). The black line is the open channel energy. Five Feshbach resonances occur at the intersections marked with black dots. The fit parameters $E_{S,l}$ have been determined to reproduce the measured resonance positions that are presented in chapter 5. The fitting procedure corresponds to the shifting and bending of the different branches, which translates into a shift of the resonances. Some characteristic features of the resonance pattern can be extracted from the model, like the resonance triplet around 150 G. Therefore, an experimentally observed pattern can easily be used to identify the bound states responsible for the resonances and finding good initial values for the fitting procedure. Once the values $E_{S,l}$ are fixed, the model predicts all Feshbach resonances in other channels with different m_F or at higher magnetic fields.

The simple visualization and the short computation time of the asymptotic bound state model make it an ideal candidate to assign experimental observations of Feshbach resonances. On the other hand, the ABM does not compute the width of the Feshbach resonances and also

neglects the dipolar coupling parts in the Hamiltonian as well as the coupling between the bound state and the scattering continuum. A full treatment of the multi-channel scattering problem is possible but requires a larger effort in analytical and numerical computing. Despite the limitations of the ABM, the resulting resonance positions are very close to the results of full coupled-channel calculations for many combinations of two species [62, 65].

2.3.3 Homonuclear Feshbach Resonances of ^{6}Li and ^{40}K

Although the research programm of the FeLiKx project focuses on heteronuclear mixtures of fermionic quantum gases, the homonuclear interactions play an important role, too. Therefore, this section will briefly discuss the known single-species Feshbach resonances of ^{6}Li and ^{40}K.

Table 2.1 lists the known resonances. The open channel state is written as $|x\rangle|y\rangle$, where x and y label the Zeeman states of the two atoms by using the letters $a, b, c...$ in order of increasing energy (see also Fig. 2.7).

Element	channel	l_o	l_c	B_{res} [G]	ΔB [G]	a_{bg}/a_0	$\Delta\mu/\mu_B$	ζ	reference
^{6}Li	$\|a\rangle\|b\rangle$	s	s	543.3	0.1	60	2.0	0.001	[54]
^{6}Li	$\|a\rangle\|b\rangle$	s	s	834.2	−300	−1405	2.0	−1400	[66]
^{6}Li	$\|a\rangle\|c\rangle$	s	s	690.4	−122.3	−1727	2.0	−850	[66]
^{6}Li	$\|b\rangle\|c\rangle$	s	s	811.2	−222.3	−1490	2.0	−1200	[66]
^{6}Li	$\|a\rangle\|a\rangle$	p	p	159.1	na	na	2.0	na	[67, 68]
^{6}Li	$\|a\rangle\|b\rangle$	p	p	185.1	na	na	2.0	na	[67, 68]
^{6}Li	$\|b\rangle\|b\rangle$	p	p	214.9	na	na	2.0	na	[67, 68]
^{40}K	$\|a\rangle\|b\rangle$	s	s	201.6	8.0	174	1.68	3.1	[69]
^{40}K	$\|a\rangle\|c\rangle$	s	s	224.2	9.7	174	1.68	3.8	[70]
^{40}K	$\|b\rangle\|b\rangle$	p	p	198.4	na	na	0.134	na	[71, 69]
^{40}K	$\|b\rangle\|b\rangle$	p	p	198.8	na	na	0.134	na	[71, 69]

Table 2.1: Properties of homonuclear Feshbach resonances for ^{6}Li and ^{40}K. The data has been taken from the review article [24]. The background scattering length is given in units of the Bohr radius $a_0 = 0.0529177$ nm. Parameters that are not defined for *p*-wave resonances are indicated as "na".

The most important resonance within the context of this thesis is the 300 G broad ^{6}Li $|a\rangle|b\rangle$ *s*-wave resonance at 834 G. The enhancement of the scattering length around this field is used for the evaporative cooling of a ^{6}Li $|a\rangle|b\rangle$ mixture. The ^{40}K atoms are sympathetically cooled during the evaporation. The details of the procedure are described in chapter 4.

Chapter 3

Experimental Setup

The main objective of the following chapter is a basic technical description of the FeLiKx machine. It comprises the ultrahigh vacuum chamber, the atomic beam source, the laser systems to slow and trap the atoms, the coils to generate the necessary electromagnetic fields, the imaging devices, and the computer control system. While the present chapter concentrates on the technical realization of the experimental setup, the details of the operation and performance are presented in chapter 4.

Most of the technologies are based on the numerous experiments for cold atoms working around the world. We especially took advantage of the knowledge from the cold atom groups in Innsbruck, Paris (C. Salomon), Austin (M. Raizen) and Florence (G. Tino). As far as the parts of our experimental setup are common within our scientific community, the description will be compact and concentrated on the special features of the FeLiKx machine.

The main challenge in realizing the experimental setup was to combine the different requirements of Li, K and Sr. In addition, we were striving to keep the operation of this multi-species machine as simple as possible to maximize the time available for scientific experiments. Therefore, we had to develop novel devices or improve existing ones. These parts of the machine will be described in more detail. This includes the multi-species oven, the glass cell, and the systems used to combine all the laser beams with different wavelengths. The high performance coils were already described in the report of Clarice Aiello [72], and the resonator dipole trap was the topic of the diploma thesis of Andreas Trenkwalder [73]. Therefore, we will only give a brief update of the current status of these two systems.

3.1 Overview of the Experiment

The scientific task of FeLiKx is to study mixtures of different fermionic atoms in the quantum-degenerate regime. When we started to design the machine in 2004, research on ultracold fermi-

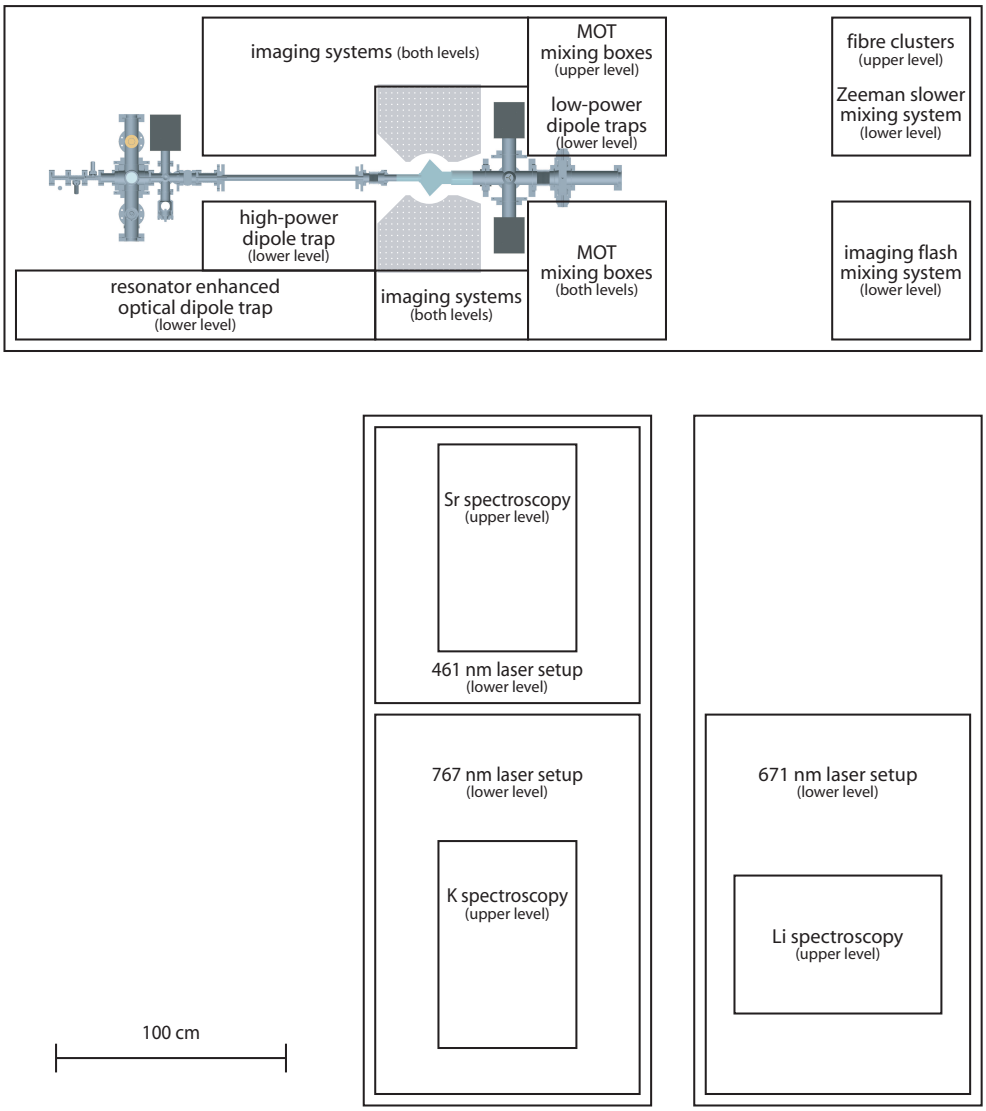

Figure 3.1: Layout of the three optical tables. The two smaller optical tables contain the near-resonant laser systems. The spectroscopy setups are places on three honeycomb breadboards on a higher level. The third table contains the vacuum chamber and all the other optical systems at the indicated places. Also shown is the central steel breadboard around the glass cell. Another steel breadboard is placed 30 cm above the glass cell (not shown). For simplicity of the figure, we did not show the coils and the mounting structure.

ons was only carried out with single fermionic elements, either with ^{6}Li or ^{40}K. These two elements are the only natural occurring fermionic alkali metals and the techniques of cooling them to quantum degeneracy are well established. Therefore, the obvious choice to select two elements for experiments with fermionic mixtures would be ^{6}Li and ^{40}K.

The FeLiKx setup is build to work with Li and K atoms. Additionally, we have designed it to be also compatible with Sr atoms. This increases the number of possible heteronuclear Fermi mixtures from one (^{6}Li-^{40}K) to three (^{6}Li-^{40}K, ^{6}Li-^{87}Sr and ^{40}K-^{87}Sr). But Sr as an alkaline earth metal has some very different properties compared to alkali atoms. An ultracold mixture of alkali and alkaline earth metals has not been realized yet and offers a new system with interesting novel properties of its own right. Discussing the various possibilities of such mixtures is beyond the scope of this thesis as the scientific results presented here only involve ^{6}Li-^{40}K mixtures. But the adding of Sr had a significant influence on the design of the machine, which is discussed in the present chapter.

The first step in designing a machine for Li, K and Sr is to choose between several possibilities for trapping the atoms in a MOT and to transfer them into an optical dipole trap. A MOT can be loaded either with a cold atomic beam or by loading the cold atoms directly from the gas in a vapor cell. The latter approach of a vapor cell MOT requires to transport the atoms into a separated UHV chamber because the vapor pressure necessary for loading the MOT is too high to give high enough lifetimes for the evaporative cooling. In general, the transport into the UHV chamber can be done either using a magnetic transport [74] or using a moving optical dipole trap [75]. In the case of Sr, only an optical transport would be possible due to the zero magnetic moment of Sr. The other possibility besides a vapor-cell MOT approach is to use a slow atomic beam to load the MOT inside a UHV environment. Such a beam can either be produced using a Zeeman slower [76] or by another MOT, often in a 2D configuration (see [77]).

The most suitable solution for Li is to use a Zeeman slower. Li requires temperatures above 300°C to have a vapor pressure high enough for a sufficient loading rate. Furthermore, the low mass of Li leads to a relatively high velocity of thermal Li and only a small fraction of the Maxwell distribution could be captured by a vapor cell MOT. These properties would make it difficult to realize a vapor cell MOT. Also a 2D MOT for Li is a challenging problem and has only been demonstrated very recently [78]. Also Sr MOTs have only been realized using a Zeeman slower so far.

On the other side, a ^{40}K MOT is usually made using a vapor cell MOT with dispensers [79]. This method only requires few milligrams of enriched ^{40}K, which is very expensive. A Zeeman slower for ^{40}K has a higher consumption of the metal. Therefore, the feasibility of a ^{40}K Zeeman slower within a limited budget was unknown to us when we designed the experiment.

As a result, there are several possibilities for the basic design of a multi-species machine for Li, K and Sr. First, one can use a Zeeman slower for ^{6}Li and ^{87}Sr and a vapor cell MOT for ^{40}K with an optical transport into an UHV chamber. This is the optimal solution for the different MOTs, but the combination of these three different parts requires a more complicate vacuum chamber and a complex experimental sequence. A similar concept has been realized for

a ^{6}Li-^{40}K-^{87}Rb mixture using a magnetic transport [80]. A second possible design would be to overcome the difficulties of a 2D or vapor cell MOT for Li (and potentially Sr) and combine it with a 2D or vapor cell MOT for ^{40}K. This approach, together with an optical transport, is realized in a ^{6}Li-^{40}K experiment at Amsterdam [81]. We chose a third possibility. We designed a novel and economic beam source working with ^{6}Li, ^{40}K and ^{87}Sr to be able to use a single Zeeman slower. This simplifies the design of the vacuum chamber and the experimental sequence, as no transport of a cold atomic cloud is required.

The general layout of the three optical tables of the FeLiKx machine is presented in Fig. 3.1. The laser systems for the near-resonant laser beams (461 nm, 671 nm and 767 nm) are placed on two separate tables. On the third table we placed the vacuum chamber, all the dipole trap laser systems, the beam mixing systems and the imaging systems. Especially the space around the glass cell is packed very tight. But we also build the other optical setups compact to keep space for further extensions. The electronics are placed over the tables on ceiling mounted racks. Many other devices are situated in the basement below the laboratory to save space and to keep the lab quiet and with a low heat load. The vacuum chamber and the different optical and electronic setups are discussed in the following sections.

3.2 Multi-Species Oven

Our attempt to use a single Zeeman slower for Li, K and Sr requires a source that emits a single atomic beam consisting of all three elements. Li, K and Sr all have very different vapor pressures (see Fig. 3.2). To optimize the atom flux individually for each element, the temperatures of the reservoirs need to be regulated separately. Additionally, the beam source must be able to operate at temperatures above 500 °C and needs to be resistant against aggressive chemical properties of the metals. Finally, the high cost of enriched ^{40}K requires an efficient use of the potassium reservoir. A beam source combining all these properties has not been demonstrated before, especially concerning the operation with only a few milligram of ^{40}K.

Enriched ^{40}K can be bought in the form of potassium chloride[2]. The potassium chloride is mixed with calcium powder and heated to obtain metallic potassium[3], which is distilled into glass ampules[4]. The enriched metallic K with 7% ^{40}K costs about 66 EUR per mg. 10 mg of 7% enriched K contain about 10^{19} ^{40}K atoms. If the beam source should operate continuously for one year with 10 mg, the flux of ^{40}K atoms would be 3.5×10^{11} per second. We need a MOT loading rate of at least 10^5 s^{-1} to be able to start an experiment after 10 s loading time with 10^6

[1] In contrast to the data presented in figure 3.2, typical temperatures for a Sr oven are between 100°C and 200°C higher than for ovens with Li. Measurements of the atomic flux from a Sr oven at the Observatoire de Paris and at JILA have obtained a flux about 100 times less than predicted by the theory. The authors attribute this deviation to errors of the values of the vapor pressure of Sr (see page 74 of reference [87]).

[2] purchased from www.tracesciences.com

[3] after 2 KCl + Ca → 2K + $CaCl_2$

[4] purchased from www.techglass.com

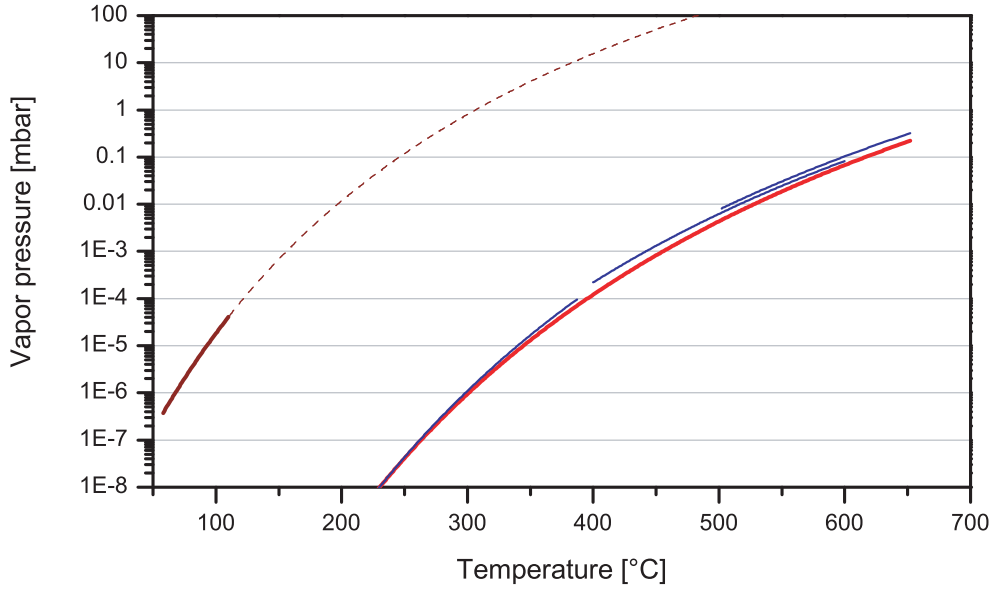

Figure 3.2: Vapor pressures of Li, K and Sr. The solid lines show the vapor pressures of Li (red) [82], K (brown) [83] and Sr (blue)[1] [84, 85, 86]. The dashed line is an extrapolation of the formula for K as no data could be found in the literature for this temperature region.

K atoms. This requires an efficiency of the Zeeman slowing process and the MOT capturing of at least 3×10^{-6}.

We performed a simulation of the Zeeman slowing process following the concept presented in [88]. The model uses the velocity distribution of the atomic beam based on its temperature and the geometry of the outlet of the oven. The evolution of the velocity and the geometry of the atomic beam is calculated throughout its propagation along the vacuum chamber including the Zeeman slowing process. All atoms that cross the MOT region and have velocities slower than the capture velocity of the MOT are trapped in the MOT. This simulation allowed us to estimate the efficiency of capturing ^{40}K atoms out of the atomic beam to be above 3×10^{-6}. Therefore, the use of an oven with enriched ^{40}K should be feasible if we find a design that fulfills all the criteria for Li, K and Sr mentioned above.

Stan and Ketterle [89] presented a multiple species atom source using a mixing chamber to which multiple reservoirs at different temperatures can be attached. The atomic beam, consisting of several elements, leaves the mixing chamber through a hole. The partial pressures in the mixing chamber of the species determines the individual flux of each element in the atomic beam. This concept allows for a very simple design of the oven. But mixing all elements in a single chamber could result in chemical reactions. Additionally, Li, K and Sr have gaseous, liquid and solid phases within the desired temperature regime. This would lead to a complex mixture where a ternary phase diagram would be necessary to understand the composition of the

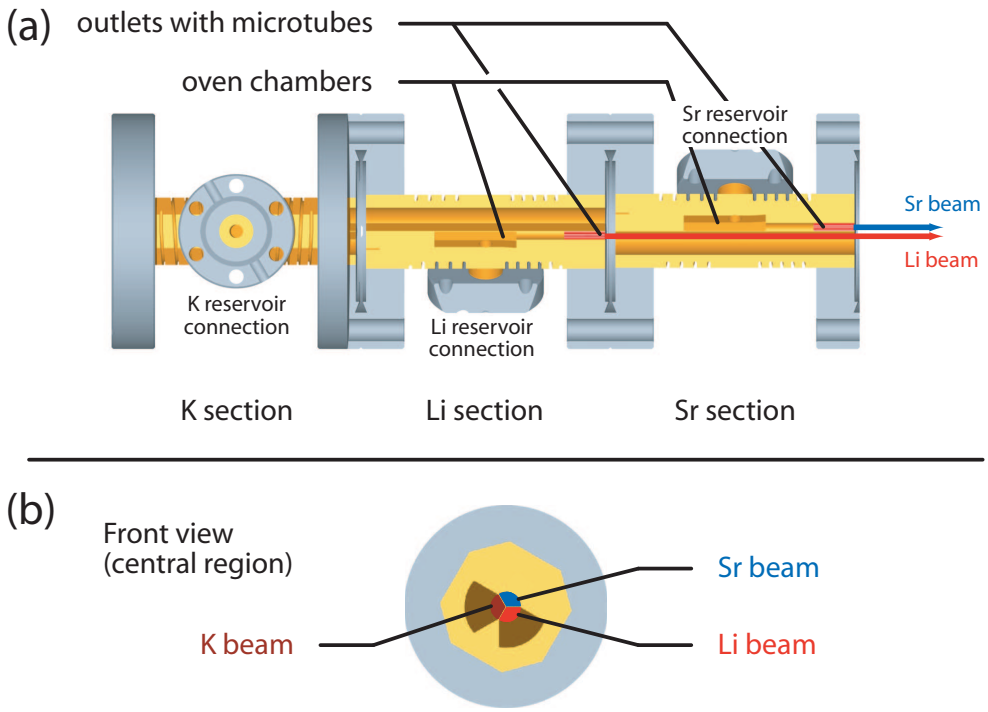

Figure 3.3: Concept of the multi-species oven. The central steel part of the oven is brass-coloured in the figure for clarity. Figure (a) shows a top view of the oven cut in the middle. The atom beams of Li and Sr are indicated by arrows that leave the outlets of the corresponding oven chambers. The Li beam flies through the fly-through chamber, which is separated by the Sr oven chamber by a thin wall. The K beam is not shown for clarity but it would pass the Li and Sr sections above the cut in the middle of the Li and the Sr beams. Figure (b) shows the front view of the oven with the beam profiles of each atomic species neglecting their transverse velocity.

mixture. In the context of using only few mg of enriched ^{40}K, this is especially problematic. We did not want to take the risk that a substantial amount of ^{40}K is bound chemically or in the fluid phase of a Li-K-Sr mixture. Therefore, we decided to develop an alternative design.

The concept of our multi-species oven is shown in Fig. 3.3. We designed an oven consisting of three different oven chambers, each with an attached reservoir. The outlets of each oven chamber are situated as close as possible to the central axis of the oven. Each oven chamber produces an atomic beam of its species with the cross section of a third circle (see Fig. 3.3b). The three oven chambers are staggered along the central axis to permit different temperatures for each section. Right after the exit of the oven, the atomic beam consists of three separated parts containing the Li, K and Sr atoms with a total diameter of 5 mm. The transversal velocity of the atoms causes the beam to be divergent. Hence, the three parts of the atomic beam begin to overlap after flying some centimeters. Effectively, this produces a single beam consisting of all three species, which can be decelarated using a single Zeeman slower. To be captured by the

MOT after the Zeeman slower, the atoms have to be close to the central axis and must have a small transverse velocity. Otherwise, the atoms hit the wall of the Zeeman slower tube or miss the MOT. To maximize the number of atoms close to the central axis, the separation between the three parts of the beam and consequently the separation between the three oven chambers must be as small as possible. This was one of the important challenges of our design. A second issue is the design of the outlet geometry of the oven. This defines the flux and the divergence of the atomic beam. An array of microtubes made of stainless steel yields a small divergence of the beam without the usage of long collimation tubes [87, 90]. This is well suited to keep the oven design compact. Furthermore, because of the small size of the outlet, the oven can be operated at higher temperatures without leaving the molecular flow regime. That would happen, if the higher temperature leads to a mean free path of the atoms, which is smaller than the size of the collimation tube.

The detailed technical realization of the oven is depicted in Fig. 3.4. It is build using three identical sections, which are connected with standard CF40 flanges. Each section has three chambers, one oven chamber and two fly-through chambers. These chambers are separated by walls with a thickness of only 0.2 mm. The oven chamber of each section has an opening with a CF16 flange to connect a reservoir with the metallic Li, K or Sr.

The front opening of the oven consists of about 55-60 microtubes[5], which fill a third circle with a diameter of 5 mm. The microtubes have an inner (outer) diameter of 200 μm (300 μm) and a length of 12 mm. They are put in place by sticking an alignment plug (not shown in the figures) into the oven chamber. This aligns the microtubes. They are held in place by hammering a wedge-shaped front plug to their side, which keeps them in the third circle shape (see Fig. 3.4a). Afterwards, the alignment plug is removed. The back part of the oven chamber is closed using another wedge-shaped steel plug. Both, the front and rear plug have to be machined very precisely to avoid small gaps.

The front and back part of each section is heated by thermocoax wires[6]. The wires are wound around the oven sections into a notch that is milled into the metal body. The circular ground shape of the notch optimizes the thermal contact between the round heating wire and the oven body. The wires are fixed using a u-shaped clamp. The front and back part of the oven can be heated individually to keep the front part the hottest spot of each section. This prevents the microtubes from clogging. A thermocouple[7] is placed close to each heating wire to measure and control the temperature.

The three oven sections are rotated 120° against each other (see Fig. 3.3, Fig. 3.4b and Fig. 3.5). The section closest to the vacuum chamber is the Sr section, the middle one the Li section and the last one the K section. Consequently, the Li beam passes the fly-through chamber of the Sr section and the K beam passes the fly-through chambers of the Li and the Sr chamber.

[5] purchased from www.goodfellow.com with 500 mm length and cut to 12 mm in the IQOQI workshop using a wire erosion machine

[6] model SEI 10/50 purchased from www.thermocoax.com

[7] model TKA05/50 purchased from www.thermocoax.com

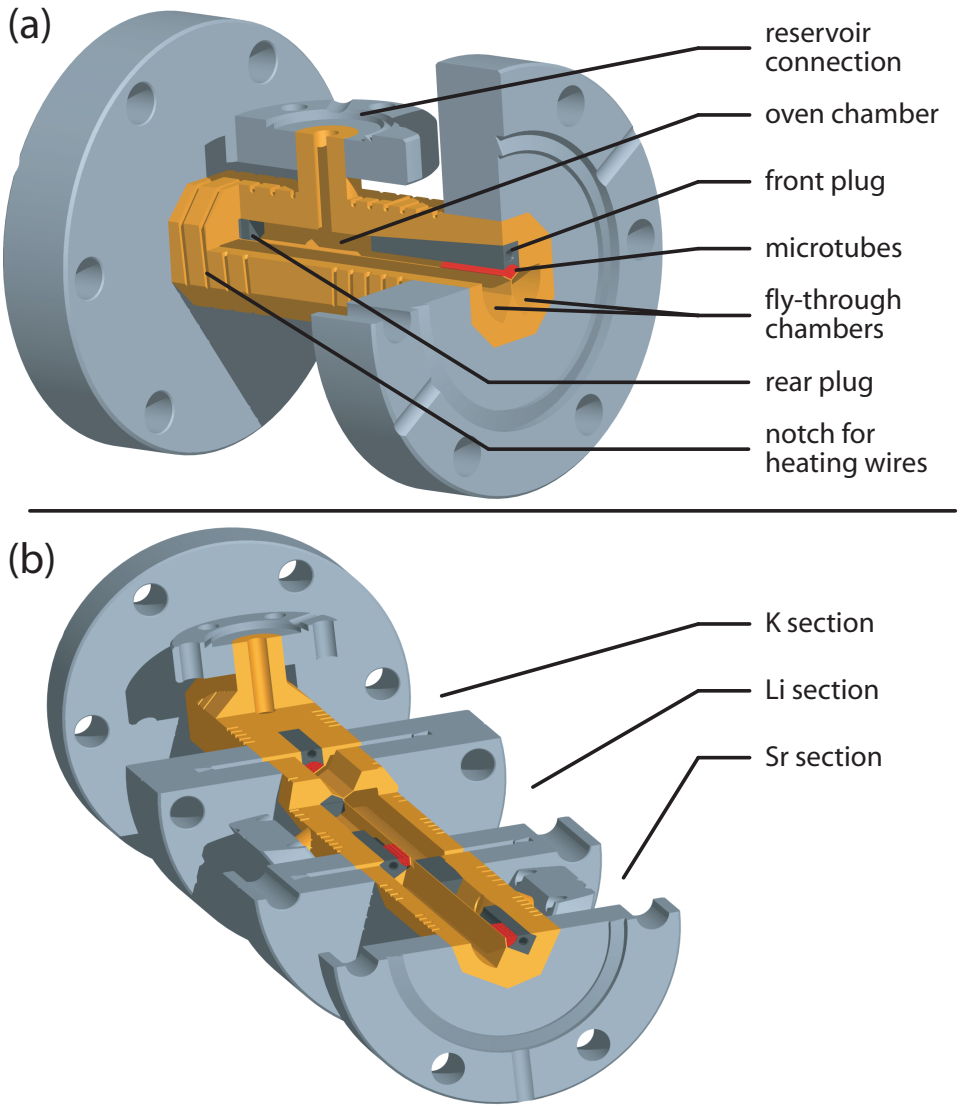

Figure 3.4: Details of the multi-species oven. Colours highlight different parts for clarity. Figure (a) shows a detailed drawing of one oven section with a cutout. Figure (b) shows all three oven sections mounted together. The front of the oven chamber is cut out below the central axis while the region between the K and the Li section is cut above the central axis.

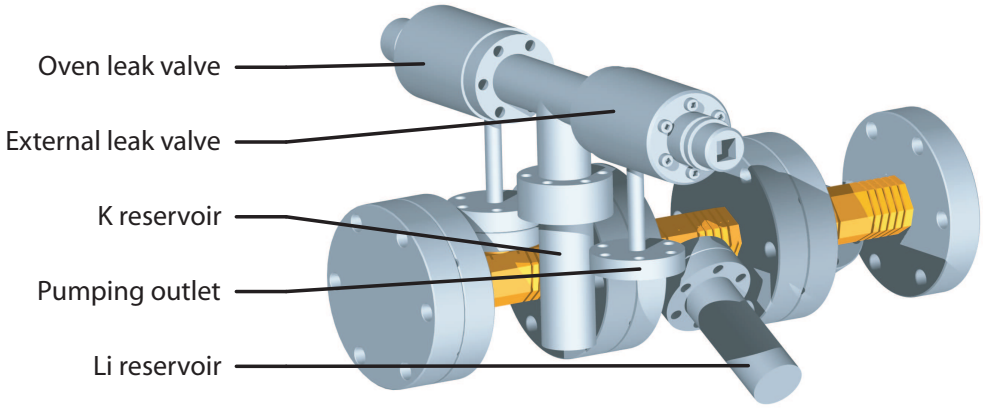

Figure 3.5: The multi-species oven is shown completely mounted with all the reservoirs. The central parts of the oven are brass-coloured in the figure for clarity.

The order of the three sections is determined by the typical temperatures of the three sections. Sr is the hottest section with around 500°C, Li is around 400°C hot and the temperature of the K section is around 200°C. The sequence described above results in a smooth temperature gradient across the oven, and keeps the microtubes the hottest place of each section. The back part of the K section is closed with an blind flange.

The metal reservoirs containing the Li, K and Sr supplies are connected to the CF16 flange on each oven section (see Fig. 3.5). For Li and Sr we use simple steel tubes. They are filled with a few grams of the metals and connected to the oven. The Li reservoir is filled with a mixture of about 80% ^{6}Li and 20% ^{7}Li to keep the possibility of experiments with the bosonic isotope. The Sr reservoir is filled with non-enriched metal. The reservoir tubes are also heated by thermocoax wires. Their temperatures are typically 20°C below the oven chambers to avoid clogging the ovens.

The reservoir for K is more complex to meet with the problem of having only a few mg of the enriched metal. It can be seen in Fig. 3.5. The K metal is also placed inside a steel tube, but an all-metal leak valve[8] is placed between the reservoir tube and the oven section. Another leak valve connects the reservoir tube with the outside to allow to separately pump this reservoir. This construction enables us to replace the K reservoir without opening the vacuum chamber. The enriched K is delivered in small glass ampules containing 10 mg of the metal. One of these ampules is put into the reservoir tube. The tube is squeezed in its lower third to prevent the glass ampule from falling to the bottom (the squeezing is not shown in the figure). The reservoir tube is now connected to the CF16 tee.

[8]model ZMD95 suitable for hot or corrosive gases purchased from www.thermovacgen.com

Heating element	Operating temperature [°C]	Standby setting [°C]
Sr oven front	500	460
Sr oven back	480	440
Sr reservoir	460	300
Li oven front	460	420
Li oven back	440	400
Li reservoir	420	300
K oven back	220	20
K reservoir	200	20
K oven valve	220	20
K external valve	220	20

Table 3.1: Typical temperatures of the different parts of the oven under operation and the standby settings.

To start a reservoir refill, the valve towards the oven is closed and the reservoir part can be pumped and baked individually. Afterwards, the reservoir tube is squeezed at the location of the glass ampule to break the glass and free the K metal. Positioning the glass ampule well above the bottom of the tube prevents the welded bottom seal from being damaged by the squeezing process. Closing the pumping valve and opening the external valve towards the oven finishes the procedure of filling the K reservoir. All parts of the reservoir are heated by thermowires and controlled using thermocouples.

After some months of using the oven, we saw evidence for a leak through the external valve of the K reservoir. High-temperature operation of the closed valve with one side exposed to atmosphere is not recommended. Therefore, we attached another low vacuum section to the outer part of the leak valve to allow operation at high temperatures. These parts are not shown in Fig. 3.5.

We use nickel gaskets for sealing the CF flanges of all oven and reservoir parts. Cooper gaskets react with alkali metals and would soon develop leaks. Furthermore, nickel gaskets work at higher temperatures than copper gaskets, which become soft at temperatures above 500°C.

All parts of the oven are insulated using glass fiber materials, which are suited for high temperatures and outer layers of aluminium foil. The whole oven part is enclosed inside an insulated box. The box prevents the warm air around the oven to cause convection currents on the optical table, which would influence the laser beams around the vacuum chamber. Warm air from the inside of the box is blown out into the cellar by a tube and a fan, and fresh air is suck in from the laboratory. This reduces the transfer of heat from the oven to the box.

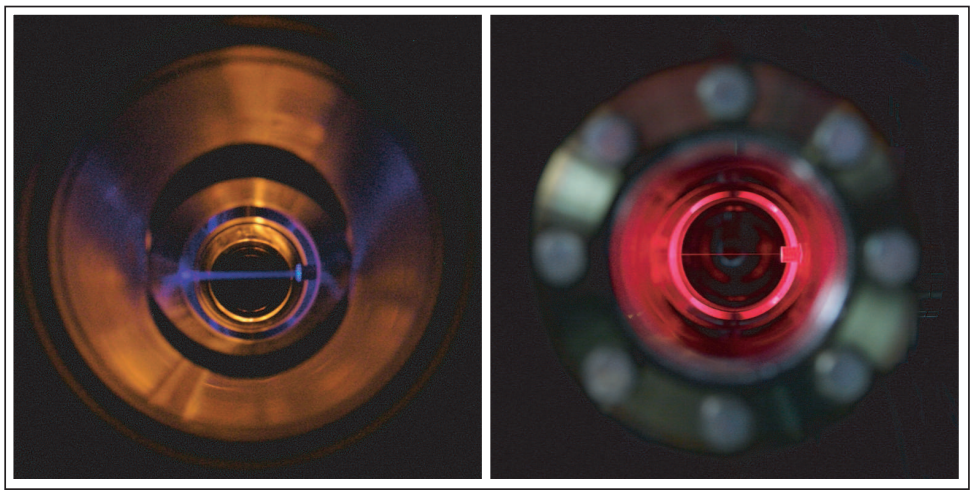

Figure 3.6: Fluorescence of the atom beams as seen through a viewport. The left photo shows the blue fluorescence of the Sr beam. The right photo shows the red fluorescence of the Li beam. The oven is located to the left of the photos. A part of the collimation tube can be seen on the right side of each photo.

The temperatures of the different oven parts are controlled via solid state relays by ten microcontrollers connected to a PC. A control software allows easy day-to-day operation of the oven without risking steep temperature ramps. In table 3.1 typical temperatures for the different oven parts are presented. If the experiments are not running, the oven can be put into a standby mode, for which the temperatures are lowered to a point where the atomic flux is negligible. The time needed to reach the operating temperature starting from the standby settings is about 30 minutes. Additionally, excessive temperature changes are reduced.

The multi-species oven was working successfully for more than 15 months with 10 mg of enriched K. After that time we did exchange the reservoir because of a significant decrease in the K loading rate into the MOT. During the exchange we found a black substance around the broken glass ampule, possibly potassium oxide. It is possible that part of the K did react with air because of a small leak through the external leak valve. But already the operation time of 15 months proves the suitability of our oven design with a Zeeman slower for experiments with small amounts of expensive materials.

Our concept for a multi-species oven is not only limited to the three species of Li, K and Sr. The design has been successfully adopted for a new two-species experiment in Innsbruck using Rb and Cs [91]. The pictures of Fig. 3.6. show the fluorescence of the atom beams of Li and Sr photographed through the viewports of the vacuum chamber.

3.3 Vacuum Chamber

Experiments with ultracold quantum gases need to be performed in a vacuum environment. A typical experimental cycle takes about 10 to 100 seconds. Therefore, the scattering rate with background particles in the vacuum must be low enough to enable lifetimes of tens of seconds possible. This requires an ultrahigh vacuum (UHV) chamber with a pressure below 10^{-10} mbar. Figure 3.7 shows an overview of the vacuum chamber. On the left side, the multi-species oven produces an atomic beam of Li, K and Sr. The atomic beam passes through two differential pumping sections, the Zeeman slower, the glass cell and finally ends at a viewport in the UHV pumping chamber.

The two differential pumping sections have several purposes. They block the gas that leaves the oven in order to achieve the pressure difference between 10^{-3} mbar in the oven and $< 10^{-10}$ mbar in the glass cell. The first chamber uses two 55 l/s ion pumps[9]. The second chamber uses a 40 l/s ion pump[10] and a titanium sublimation pump[11]. The first two chambers are connected by a differential pumping tube (inner diameter 5 mm, length 108 mm, conductance 0.14 l/s). Both chambers can be evacuated by a full-metal CF40 angle valve[12]. The first chamber has a Bayard-Alpert type ionization gauge[13] for measuring the pressure. Additionally, four viewports[14] provide optical access along two orthogonal axis. They have an anti-reflection coating for the 461 nm light used for transversal cooling of the Sr atom beam. The second differential pumping chamber has a wobble stick[15], which is used as a shutter for blocking the atomic beam. The shutter is actuated using a computer-controlled servo motor. Both differential pumping chambers are separated from the rest of the vacuum chamber by a full-metal CF40 gate valve[16]. The gate valve allows us to service the high vacuum part of the chamber without opening the ultrahigh vacuum part. This is necessary if the Li or Sr reservoir need to be exchanged or if a leak occurs in the oven or the differential pumping chambers. After the gate valve, a second differential pumping tube (inner diameter 6 mm, length 137 mm, conductance 0.19 l/s) is placed in front of the Zeeman slower tube.

The part of the vacuum chamber described so far is mounted on an aluminium breadboard and connected to the rest of the vacuum chamber by a CF40 bellow. That allows to move the front part of the vacuum chamber relative to the UHV part. This way, the atomic beam, which is collimated by the microtubes and the differential pumping tubes within the chamber, can be aligned to hit the MOT.

[9] model Vaclon Plus 55 StarCell purchased from www.varianinc.com
[10] model Vaclon Plus 40 StarCell purchased from www.varianinc.com
[11] model ZST23 purchased from www.thermovacgen.com
[12] model 54032-GE02 purchased from www.vatvalve.com
[13] model UHV-24p purchased from www.varianinc.com
[14] type VPZ64 purchased from www.vacom.de
[15] model WS-275 purchased from www.mdcvacuum.com
[16] model 48132-CE44 purchased from www.vatvalve.com

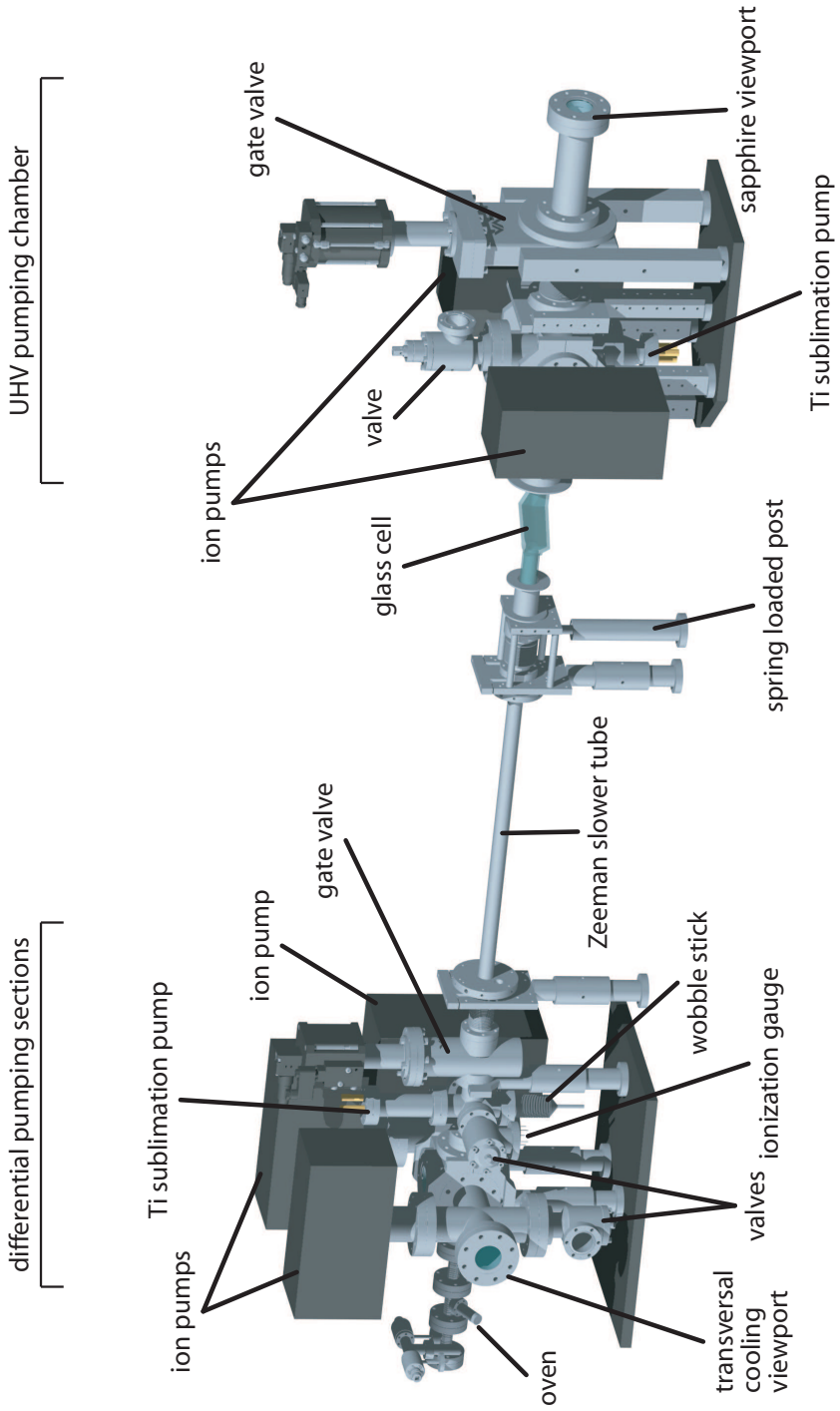

Figure 3.7: CAD drawing of the vacuum chamber. See text for more details.

The next part of the vacuum chamber is the Zeeman slower tube. It is 600 mm long and has an inner diameter of 14 mm. After the Zeeman slower, the atoms reach the region where they are captured by the MOT and where all further experiments are done. We designed a special glass cell for this central part of the vacuum chamber. The glass cell will be discussed in detail in section 3.4. It is connected to the Zeeman slower tube by a flexible welded bellow[17] to avoid stress. The other side of the glass cell is mounted to a CF63 six-way cross. Two 55 l/s ion pumps and a titanium sublimation pump are attached to this cross to maintain a pressure of less than 10^{-10} mbar in the glass cell. An all-metal angle valve[18] is used for evacuating the UHV part. The end of the vacuum chamber consists of a CF63 sapphire viewport[19] for the Zeeman slower laser beam. The outer surface of the 2" sapphire window has a broadband antireflection coating for 450-800 nm. The viewport is heated permanently to 200°C to prevent the inner surface from getting coated by the atomic beam. Two metal boxes with 3" windows[20] enclose the hot viewport to avoid air turbulences and possible sudden temperature changes of the sapphire window. The warm air inside the outer box is blown out into the cellar by a tube and a fan and fresh air is suck in from the laboratory. The viewport is separated from the six-way cross by a straight tube, a gate valve[21] and a flexible bellow. We installed the gate valve, because viewports are a potential risk for developing leaks, especially if the seals are coated with alkali metals. The gate valve would allow us to exchange the Zeeman slower viewport without venting the UHV chamber with the glass cell. The bellow protects the glass cell from vibrations caused by actuating the gate valve and the viewport can be shifted if it gets coated in spite of the heating. The straight CF63 tube allows us to heat the viewport without heating the gate valve.

To reach a pressure below 10^{-10} mbar, all parts of the vacuum chamber need to be baked to remove any dirt and water from the surfaces and to deplete the metal surface from hydrogen. We used several steps of baking to achieve a very clean and hydrogen free chamber. All parts that were fabricated in our workshop (i.e. most parts of the oven, the differential pumping tubes and the Zeeman slower tube) were baked at more than 400°C for several days to remove any residual oil from the manufacturing process. The vacuum chamber was first assembled without the glass cell. All parts were chosen to be heatable to at least 300°C. The assembled chamber was baked at 300°C for several weeks to remove any residual dirt and as much hydrogen as possible. After mounting the glass cell, the UHV part of the vacuum chamber was baked at 200°C for 12 days. The ion pumps and titanium sublimation pumps were activated to be cleaned while still hot. Finally, the chamber was cooled down to room temperature and helium leak tests were performed using a residual gas analyzer.

The current of the two ion pumps of the UHV chamber is below the lowest measurable value of 10^{-7} A, which corresponds to a pressure below 10^{-10} mbar. The pressure inside the glass cell is difficult to measure but we have reached lifetimes of more than 50 s of cold atoms inside a magnetic quadrupole trap. Therefore, the vacuum quality does not limit our experi-

[17] custom made by www.comvat.com
[18] model 57132-GE02 purchased from www.vatvalve.com
[19] custom made by www.torrscientific.co.uk
[20] purchased from www.cvilaser.com
[21] model 48236-CE44 purchased from www.vatvalve.com

ments. The first differential pumping section has a pressure below 10^{-9} mbar (measured with the Bayard-Alpert ionization gauge) if the oven is fully operating. The current of the ion pumps is continuously compared to a threshold value. If exceeded, the gate valves are closed automatically by an electro-pneumatic security system. This protects the different sections of the vacuum chamber from being vented by leaks in other sections.

3.4 Glass Cell

The glass cell is one of the key elements of the experimental design. All experiments with the cold atoms are performed inside the cell. Exchanging the glass cell would take several months. Therefore, the design of the glass cell should be compatible with a wide range of possible experiments. The main criteria for the design of the glass cell is to get good optical access from many different directions. This is especially important for a multi-species experiment, which requires many laser beams for trapping, manipulating and imaging the atoms. Our novel design is shown in Fig. 3.8, see Fig. 3.9 for a photo.

The glass cell was manufactured by Hellma GmbH[22]. The central part is made of Spectrosil 2000, a synthetic fused silica[23]. The walls have a thickness of 5 mm. They are joined by thermal bonding. This process joins the glass surfaces without exceeding the melting temperature of the material. The glass walls keep their high optical quality while a vacuum-tight connection is achieved. To connect the glass cell with the CF flanges of our vacuum chamber, two glass to metal transitions[24] are attached to the central part.

The inner height of the glass cell is 22 mm. This corresponds to the maximal diameter of a laser beam that can be used with 1" lenses and wave plates. Together with the bottom and the ceiling, the total height of the central part is 32 mm. The low height allows to place the magnetic coils around the glass cell close together to maximize the magnetic field for a given current. For the glass to metal transition on the right side we chose a larger CF63 flange to increase the pumping speed towards the ion pumps.

The diamond shape of the glass cell was chosen to have three orthogonal axis with each crossing at least one wall under 90°. This reduces aspherical aberrations of beams along these axis, which is important for both imaging beams and dipole trap beams. The two walls on the left of the glass cell deviate from the orthogonal orientation but are designed to provide an axis at Brewster's angle. Such an axis is necessary for a resonator enhanced optical dipole trap [92]. Additionally, it is also useful for other high-power dipole traps to decrease the Fresnel

[22] www.hellma-worldwide.com

[23] For applications with high-power infrared laser beams, quartz glasses with a low content of OH molecules may be a better choice. OH molecules have absorption bands in the infrared regions, which contribute to thermal lensing. For example, Suprasil 3001 has an OH content of ¡1 ppm compared to 1000 ppm of Spectrosil 2000.

[24] models SQ-200-F3 and SQ-125-F2 with 316 non-magnetic steel flanges purchased from www.larsonelectronicglass.com

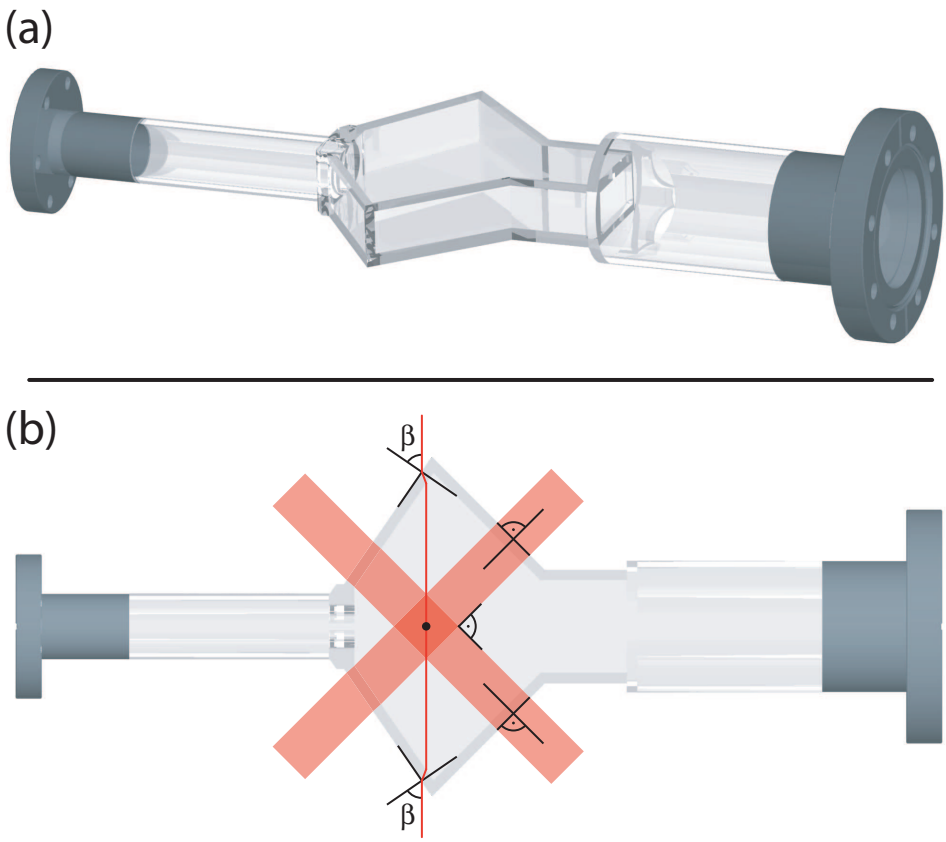

Figure 3.8: CAD drawing of the glass cell. Figure (a) shows a 3D overview of the glass cell. Figure (b) shows a top view of the glass cell. The outlines of the two MOT, respectively imaging laser beams are drawn in red as well as the beam path for the resonator dipole trap. β indicates Brewster's angle. The optical access in between the shown beam paths can be used for additional purposes.

reflections. More information about the different traps and imaging systems can be found in the corresponding sections of this chapter.

Compared to steel chambers with viewports, glass cells can offer a better optical access to the trapped atoms. Another advantage of glass cells is, that magnetic fields are less affected by metal structures. This particularly improves the switching times because less eddy currents are generated. On the other side, glass cells are very fragile. Mounting them to the vacuum chamber requires a well elaborated concept with a lot of care, especially using glass cells with two flanges. The most important task is to minimize stress during mounting as well as during bakeout and for the long time of usage afterwards. Our glass cell is mounted with the CF63 flange to the back part of the vacuum chamber. This fixes its position. The other side is connected to a flexible welded bellow, which compensates small movements as for example due to temperature changes. The torque on this end of the glass cell and the bellow is canceled by a spring inside

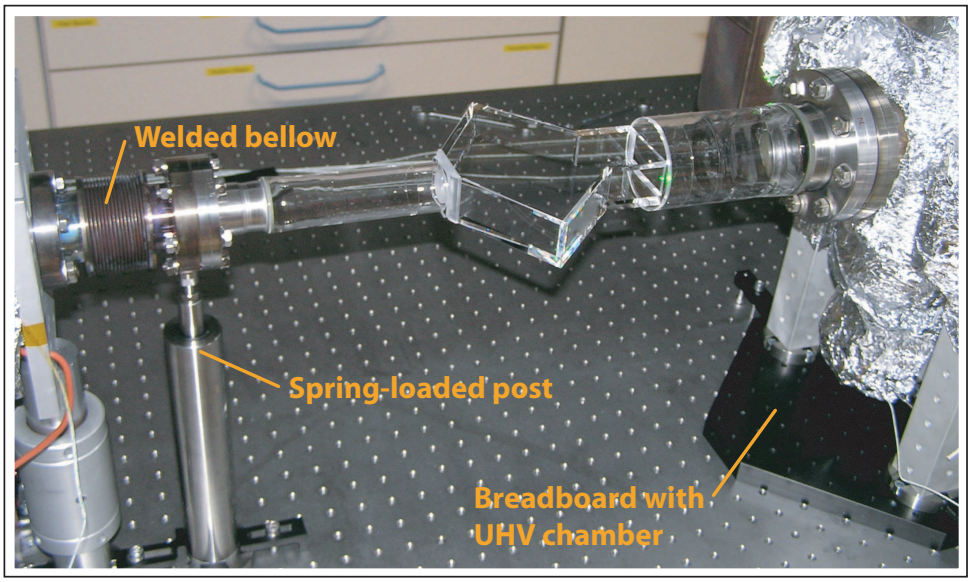

Figure 3.9: Photo of the mounted glass cell before the bakeout.

the post below this connection. The post is pressing upwards against the flange with a force compensating gravity. Figure 3.9 shows a photo of the glass cell before the final bakeout.

Mounting the glass cell was done as follows. In a first step, we mounted the CF40 flange to the rotatable flange of the welded bellow. Before this procedure, the CF63 flange of the glass cell was placed on foam on a digital balance, which indicated the residual force. The balance could be moved up and down using a lab jack to compensate any undesired force, especially during the mounting procedures. The CF40 glass cell flange was clamped to a solid mount to reduce the force on the cell. While tightening the CF seal, the lab jack was used to cancel out occuring forces. The rotational degree of freedom was controlled using dial gauges. After the CF40 connection was closed, the clamp was opened and we checked the alignment of the glass cell. When the alignment was not good enough, the last steps had to be repeated. We could finally achieve an alignment of the glass cell being parallel to the optical table within less than 0.05°. The solid mount for the CF40 flange was now carefully exchanged against the spring-loaded post. The length of the rod on top of the spring was adjusted such that the CF40 flange position did not move within the precision of the dial gauges. The next step was mounting the CF63 flange. For this, we approached the back part of the vacuum chamber slowly to the glass cell by sliding it on its breadboard. After it was fixed in its final position, we inserted the copper gasket and tightened the seal.

The whole procedure is completely adiabatic. This means it can be interrupted at any time without risk. Especially attaching the glass cell during the first step and cancelling residual forces using the balance allows to minimize the stress on the glass. A more detailed description with photos can be found in reference [93]. During the bakeout at 200°C, the glass cell was surrounded

by a metal cage to avoid contact with the heating wires and to protect the glass surfaces from evaporating dirt.

3.5 Resonant Laser Systems

For slowing, trapping, manipulating, and imaging the atoms, we need laser beams with frequencies to address the dipole transition from the ground *s*-state to the excited *p*-state. Therefore, suitable laser systems and an optical setup to control the frequency and intensity for all the laser beams is required. These optical setups will be described in the present section.

The laser systems and the associated optical setups are placed on two separate optical tables. One table is used for the Li, the second for the K laser system. Both tables have space for the different parts of the Sr laser system. The different laser beams are sent to the vacuum chamber, which is placed on the third table, using polarization maintaining single-mode glass fibres. Using fibres brings along unavoidable losses. But separating the laser systems from the vacuum chamber using glass fibres avoids realignments of the critical optical setup around the vacuum chamber if the laser system needs realignment. Separating the Li and K setup between two tables allows to operate the machine with Li while another person is working on the K laser system or the other way around.

3.5.1 Laser System for Lithium

Laser cooling of Li atoms requires light with a wavelength of 671 nm. The level diagrams of ^{6}Li and ^{7}Li are shown in Fig. 3.10. For the MOT, we use the D2 line with the $F = 3/2 \rightarrow F' = 5/2$ transition. The linewidth of this transition is 6 MHz. As the hyperfine levels of the excited $P_{3/2}$ state are spaced closer than the linewidth, the $F = 3/2 \rightarrow F' = 5/2$ transition is no cycling transition and a large amount of atoms will be pumped into the $S_{1/2}, F = 1/2$ ground state. This requires a large amount of repumping light with a frequency offset of 228 MHz to depopulate the $S_{1/2}, F = 1/2$ state. For ^{6}Li, a well working ratio between repumping power and principal cooling power is 1:1. Therefore, the distinction between repumping and cooling transition is not really valid, as both transitions equally contribute to the cooling process in the MOT.

The spin-flip Zeeman slower requires light with an offset of -496 MHz from the $F = 3/2 \rightarrow F' = 5/2$ transition to compensate the magnetic Zeeman shift. Equally shifted repumping light is also required.

For the imaging laser beams and optical pumping, the required frequencies depend on the applied magnetic field and the spin state of the atoms. Typically, imaging is done close to a Feshbach resonance to study molecules and Cooper pairs, or at zero magnetic field. To cover the whole range between zero and a few thousand Gauss, a tunable, beat locked laser with a tuning range of several GHz is needed. An alternative is to use beams from the MOT and Zeeman

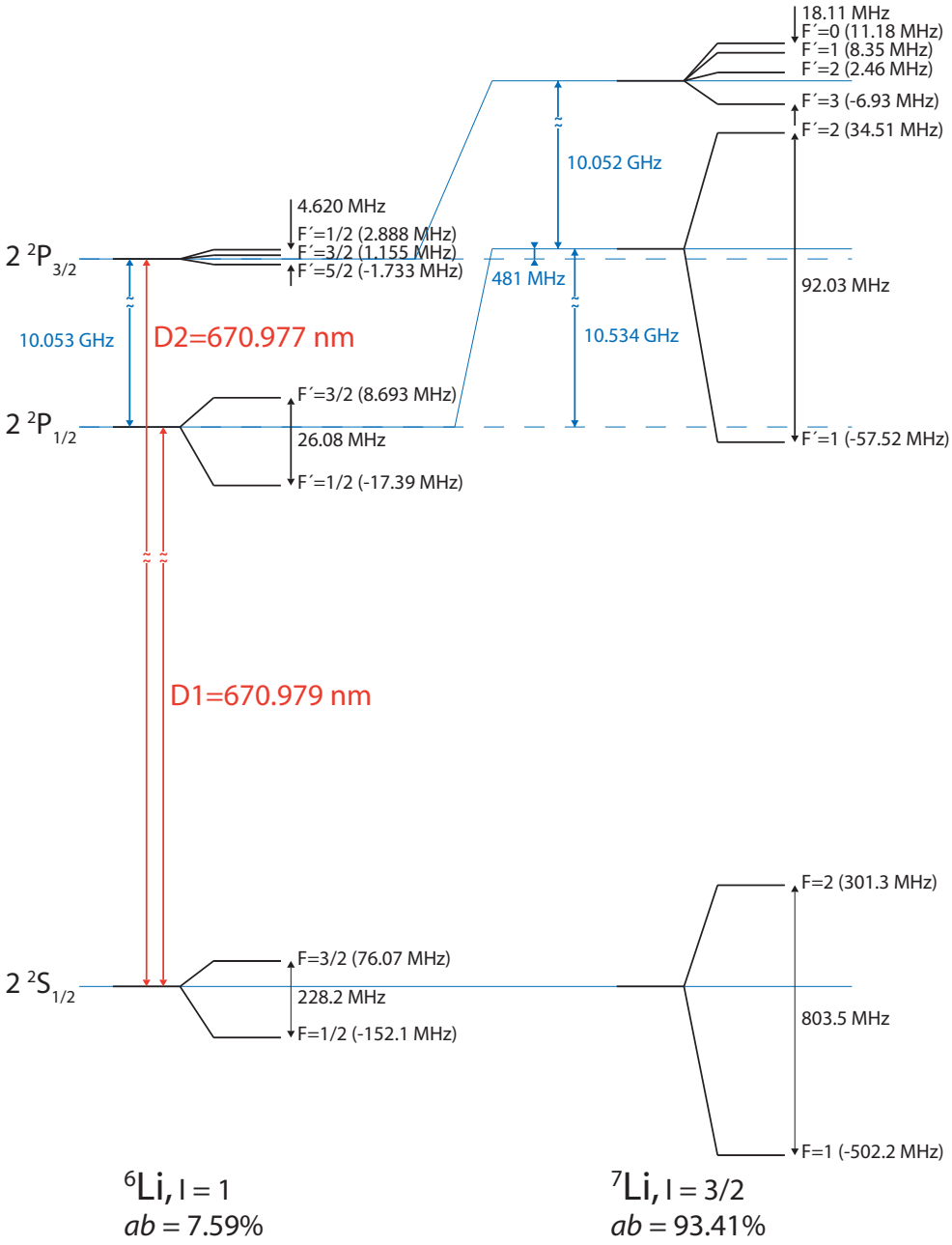

Figure 3.10: Diagram of energy levels for ^{6}Li and ^{7}Li. The natural abundance ab of the isotopes is given at the bottom. The data is taken from [94]

slower setup and to shift their frequencies using acousto-optical modulators (AOMs). This is eased because those beams are not needed during the imaging sequence. The latter approach is easier but it is only possible to cover few regions of the magnetic field.

During the first two years of building and operating the experiment, we used a dye laser[25] pumped with a 10-W Nd:YVO_4 laser[26]. At that time, this was the only commercially available laser source with more than 250 mW output power. We were able to reach between 500 and 1000 mW of 671 nm light and could operate the dye laser continuously for more than 10 hours without relocking. Unfortunately, these happy times of perfect operation were frequently interrupted by the necessary maintenance work to exchange the dye and to realign the laser cavity for optimal performance. We tried different laser dyes (DMC in ethylene glycol and LD688 in 2-phenoxyethanol) and different alignment strategies. But we always had to service the dye laser for several days per month. Therefore, we exchanged the dye laser against a system using diode lasers and tapered amplifiers[27] in the year 2007 as these lasers were available by that time.

In the following, we describe the laser setup as it is working at the time of writing this thesis. A conceptual drawing of the laser system can be seen in Fig. 3.11. The main laser source is a commercially available system consisting of a Fabry Perot type semiconductor laser with an external grating for frequency stabilization and a subsequent amplification with a tapered amplifier diode. The system is set to an output power of about 300 mW. The light is sent through an optical fibre to obtain a Gaussian beam profile, which is better suited for the following AOMs and seeding of the other two tapered amplifiers. Furthermore, modifications of the laser source do not require an alignment of all the other elements after the optical fibre.

A small part of the output power is split off to be used for frequency characterization and stabilization. The spectrum of the light is measured using a dedicated Fabry Perot spectrometer[28]. The absolute frequency is measured using a Fizeau interferometer type wavemeter[29]. The light for the spectroscopy passes a double-pass AOM (DP-AOM) to shift the frequency of the laser to a convenient value. The locking signal for frequency stabilization is produced using a modulation transfer spectroscopy setup [95]. For this, the laser beam is split in two parts. The phase of one beam is modulated with 8 MHz using an electrooptical modulator. Both beams are overlapped in counterpropagating directions passing a spectroscopy cell[30] with ^{6}Li vapor. If the light is resonant with the atomic transition, the modulation signal is transferred from one beam onto the other and can be measured on a photodiode. The electronic signal is mixed with the 8 MHz modulation signal. The resulting profile is the derivation of the doppler free absorption profile. A PID regulator is used to lock the laser to the zero crossing of the profile. The error signal is split into a fast and slow part. Slow deviations are corrected by moving the laser grating with a piezo. Fast deviations are corrected by modulating the laser current.

[25] purchased from www.radiant-dyes.com
[26] purchased from www.coherent.com
[27] purchased from www.toptica.com
[28] model FPI 100 purchased from www.toptica.com
[29] model WS6 purchased from www.toptica.com
[30] purchased from www.leosolutions.com

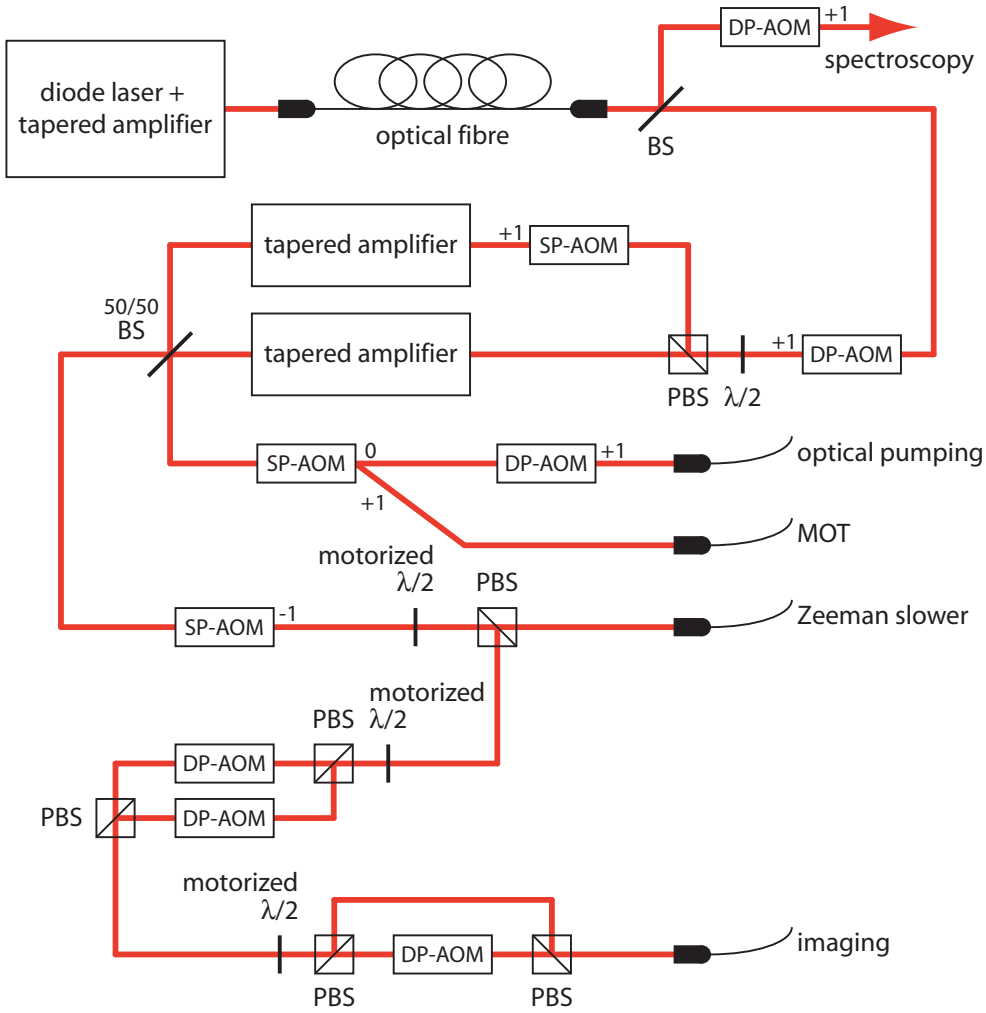

Figure 3.11: Optical concept for the 671 nm laser system. The propagation of the laser beams through the functional elements of the optical system is shown. For simplicity, mirrors, lenses, and shutters are not shown as well as some wave plates for polarization corrections.

The major part of the output power from the main laser passes a double-pass AOM, which is used to change the frequency, as for example during the different phases of the MOT. The resulting beam is split in two fractions. One part is directly coupled into the second tapered amplifier and is used for the cooling transition. The frequency of the other part is first shifted by 228.2 MHz using a single-pass AOM (SP-AOM) before seeding a third tapered amplifier. This light is used for the repumping transition. Each tapered amplifier delivers up to 400 mW of optical power. The two beams are combined using a 50/50 beamsplitter. One of the resulting beams is sent through a single-pass AOM and further into a fibre towards the optics for the

MOT on the vacuum table. The zeroth order of the single-pass AOM passes another double-pass AOM. It is coupled into a fiber and can be used for optical pumping during various steps of the experimental sequence. The second output beam from the 50/50 beamsplitter is used for the Zeeman slower and for imaging. The light traverses a single-pass AOM to yield the necessary frequency for the Zeeman slower. A motorized wave plate together with a polarizing beamsplitter can direct the beam either towards the optical fibre for the Zeeman slower or towards the preparation system for the imaging light. This preparation system consists of three AOMs, which allow to cover a wide range of frequencies together with the AOMs passed up to this point. Again, motorized wave plates allow to chose which AOMs are used. The resulting frequencies are used for imaging different spin states of Li at various magnetic fields. Computer controlled mechanical servo motor shutters are installed at the outputs of the tapered amplifiers and in front of all the fibre inputs. They allow to completely shut off the different laser beams after the fibres.

3.5.2 Laser System for Potassium

The transition used for laser cooling of K has a wavelength of 767 nm. The level diagram of the three K isotopes is shown in Fig. 3.12. Note, that the hyperfine structure of ^{40}K is inverted compared to ^{6}Li due to a negative nuclear g-factor.

For the ^{40}K MOT, we use the D2 line with the cycling $F = 9/2 \rightarrow F' = 11/2$ transition. The linewidth of this transition is 6 MHz. The energy spacing towards the next excited $P_{3/2}, F' = 9/2$ state is 43.4 MHz. This is close enough to pump some of the atoms into the $S_{1/2}, F = 7/2$ state, and a repumping laser is needed to bring them back to the cycling MOT transition. The frequency of the repumping light has an offset from the MOT transition corresponding to the hyperfine splitting of 1286 MHz.

Our spin-flip Zeeman slower for ^{40}K requires light with an offset of -160 MHz from the $F = 9/2 \rightarrow F' = 11/2$ transition. Equally shifted repumping light is needed as well.

For imaging the ^{40}K atoms, we can use a tunable laser to cover a large range of magnetic fields and spin states. Alternatively, a frequency close to the repumping transition can be used to image the K atoms at 760 G on the molecular side of the Li Feshbach resonance.

We use a system of semiconductor lasers and tapered amplifiers to generate all the required beams. The layout of the system is shown in Fig. 3.13. Three semiconductor lasers[31] are locked on the cooling, the repumping and the imaging transition. These Fabry Perot type diode lasers have one anti-reflection coated facet towards a grating in Littrow configuration, which is used as external cavity. The laser beam is coupled out of the second facet of the diode. This design allows to reach higher output powers compared to designs where only one facet is used for both purposes. Our lasers are each specified to deliver up to 100 mW of power at 767 nm. But to increase their lifetime, we only use them at around 60 mW, which is enough for our setup.

[31] model SYS-120-0765-100 from www.sacher-laser.com

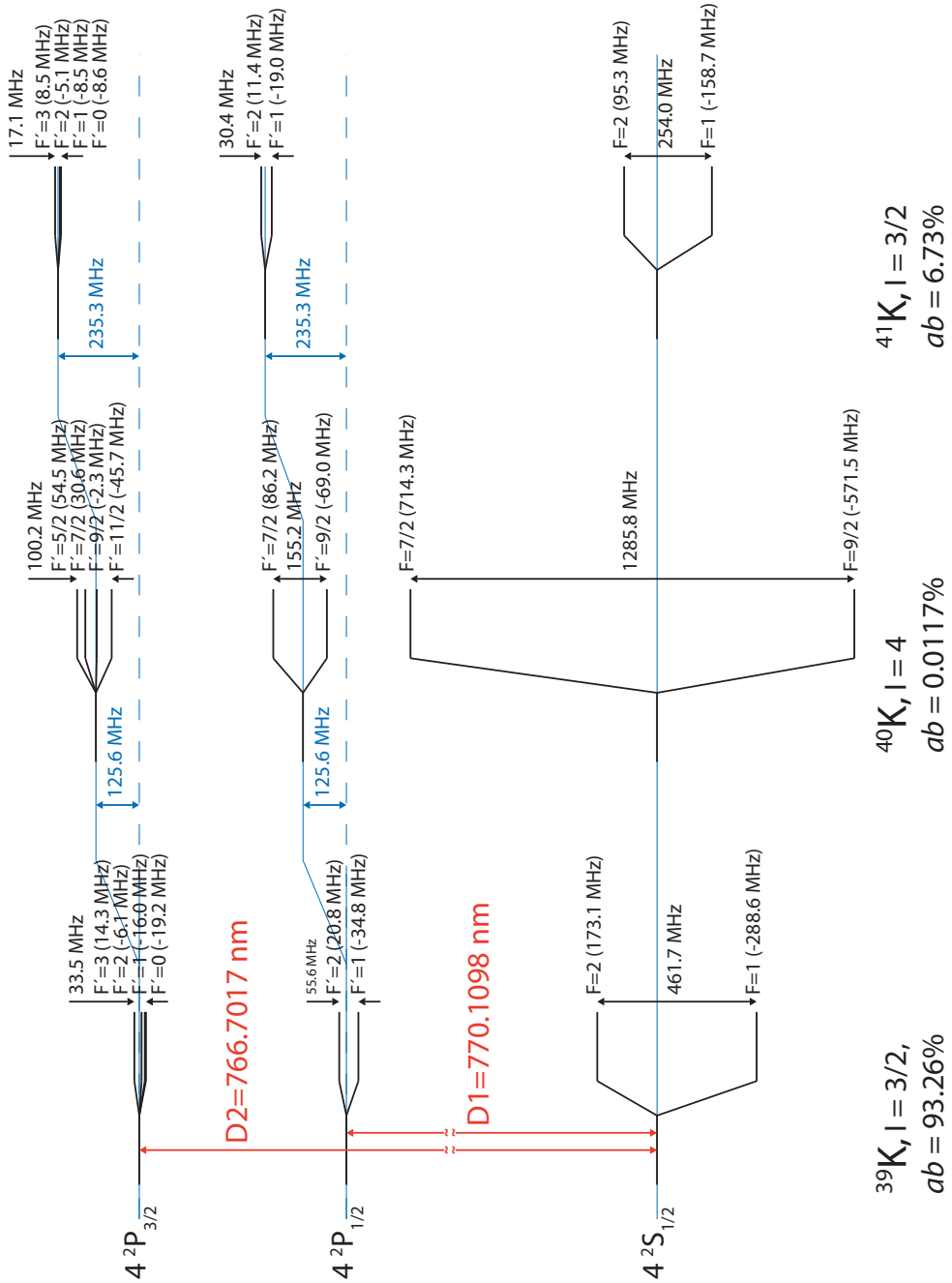

Figure 3.12: Diagram of energy levels for ^{39}K, ^{40}K and ^{41}K. The natural abundance ab of the isotopes is given at the bottom. The data is taken from [96].

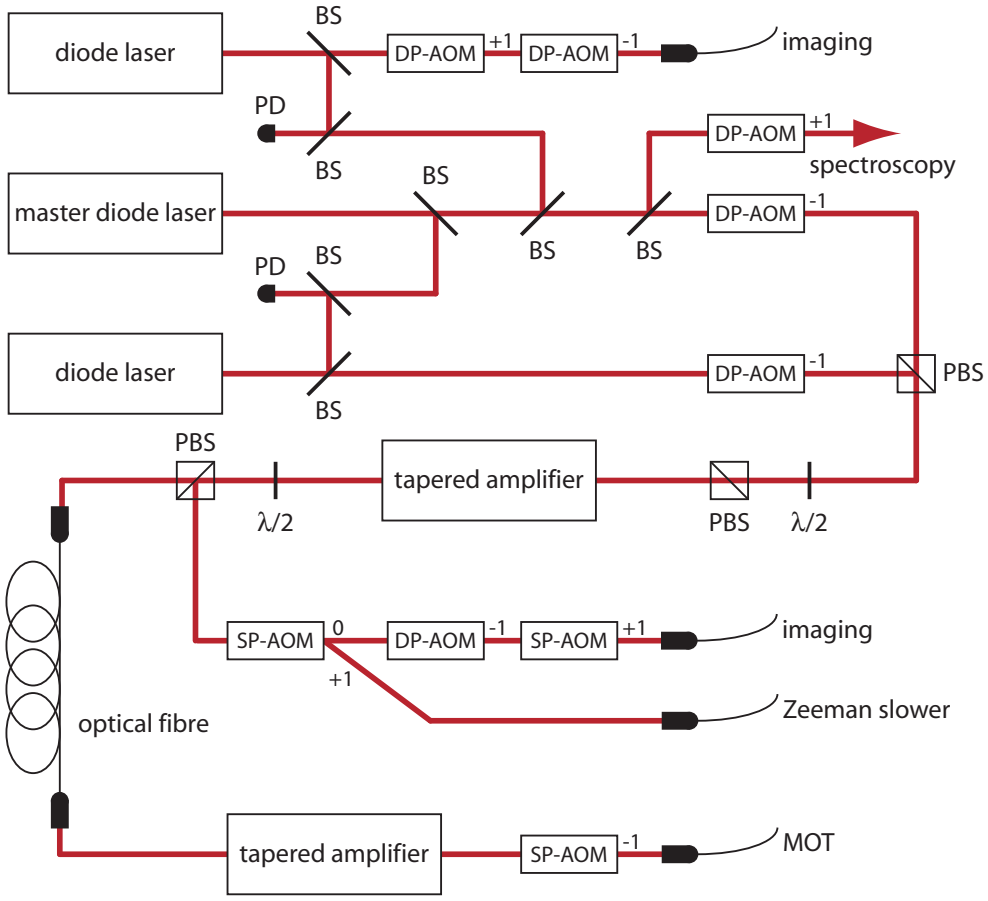

Figure 3.13: Optical concept for the 767 nm laser system. The propagation of the laser beams through the functional elements of the optical system is shown. For simplicity, mirrors, lenses, and shutters are not shown as well as some wave plates for polarization corrections.

The master diode laser is directly locked to an atomic transition as already described in section 3.5.1 for the 671 nm laser system. For K, we use the $F = 2 \rightarrow F' = 3$ transition of the ^{39}K isotope, because the low abundance of ^{40}K in the spectroscopy cell would result in a very weak signal. The laser beam used for locking passes a double-pass AOM in front of the spectroscopy setup. As in the 671 nm laser setup, this allows us to adapt the frequency to a comfortable value for the overall AOM scheme. In addition, this double-pass AOM can also be used to quickly change the laser setup from a setting suitable for ^{40}K to a setting suitable for working with ^{39}K. For this, we use two double-pass AOMs positioned in series very close to each other. Both are aligned in a different way. One is used for ^{39}K in $+1^{\text{st}}$ order and the other one is used for ^{40}K in -1^{st} order. The configurations can be toggled by simply switching one AOM off and the other one on without need of realignment.

The two other laser diodes are locked to the master laser using a beat lock as described in [97]. The beam of the master laser is overlapped with another laser beam and sent onto a fast photodiode (PD). The photodiode generates a beat signal with a frequency $\delta\nu$ equal to the frequency difference of the two lasers. This signal is mixed with a local oscillator of frequency ν_{LO}. The signal from the mixer is split in two signals and one of them is delayed by a time τ using a coaxial cable. Afterwards, the two signals are recombined using a second mixer. The resulting error signal is proportional to $\cos(2\pi\delta\nu - \nu_{\mathrm{LO}}\tau)$ and can be used by a PID to lock the laser. Varying the frequency of the local oscillator ν_{LO} allows to tune the frequency of the imaging laser to address the imaging transition at different magnetic fields.

The locking signal is not sensitive to the sign of the frequency difference $\delta\nu$. To obtain this information, we monitor the beat signal between the light from the master laser and the other lasers after having passed through the AOMs of the setup. As the light from the master laser experiences a different frequency shift as the light from the other two lasers, the beat frequency $\delta\nu + \Delta\nu_{\mathrm{AOM}}$ now depends on the sign of $\delta\nu$. $\Delta\nu_{\mathrm{AOM}}$ contains the overall frequency shifts after passing through the different AOMs. The beat signal is monitored using an electrical spectrum analyzer and is very useful for locking the two additional lasers to the master. As for the 671 nm lasers, we also monitor the lineshape of the lasers using a Fabry Perot spectrometer and we can measure the optical frequency using the wavemeter.

The light from the beat locked laser used for imaging is sent through a double-pass and a single-pass AOM for fast frequency and intensity manipulations. Finally, it is coupled into the fibre towards the imaging setup.

The master laser and the other beat locked laser are used to generate the light for the MOT and the Zeeman slower. In the settings for ^{40}K, the master laser generates the repumping light and the beat locked laser generates the light for the cooling transition. In the case for ^{39}K, the roles of both lasers are exchanged. Each of the laser beams pass a double-pass AOM before being combined using a polarizing beamsplitter. The two overlapped laser beams are now coupled into a first tapered amplifier[32]. The ratio of cooling versus repumping light can be adjusted using another polarizing beamsplitter and a quarter-wave plate. The tapered amplifier delivers up to 800 mW of optical power. Using a single tapered amplifier for a beam with two frequency components is less critical for ^{40}K as it would be for ^{6}Li. The nonlinear amplification process generates sidebands by mixing the two frequencies [98]. The power located inside the sideband components is lost for the laser cooling transitions and can even be disturbing for the MOT, optical pumping or imaging. The frequency separation of 1286 MHz for the hyperfine splitting of ^{40}K is large enough to keep the sidebands small. The hyperfine splitting of ^{6}Li is 228 MHz, which would create sidebands strong enough to deteriorate the system. The output from the tapered amplifier is split in two parts using a polarizing beamsplitter. The larger part passes a single-pass AOM and is coupled into the fibre towards the Zeeman slower. The zeroth order from this AOM can also be used for imaging. In this case, the single-pass AOM for the Zeeman slower is switched off and the zeroth order passes another two AOMs to adapt the frequency for

[32]model BoostTA from www.toptica.com

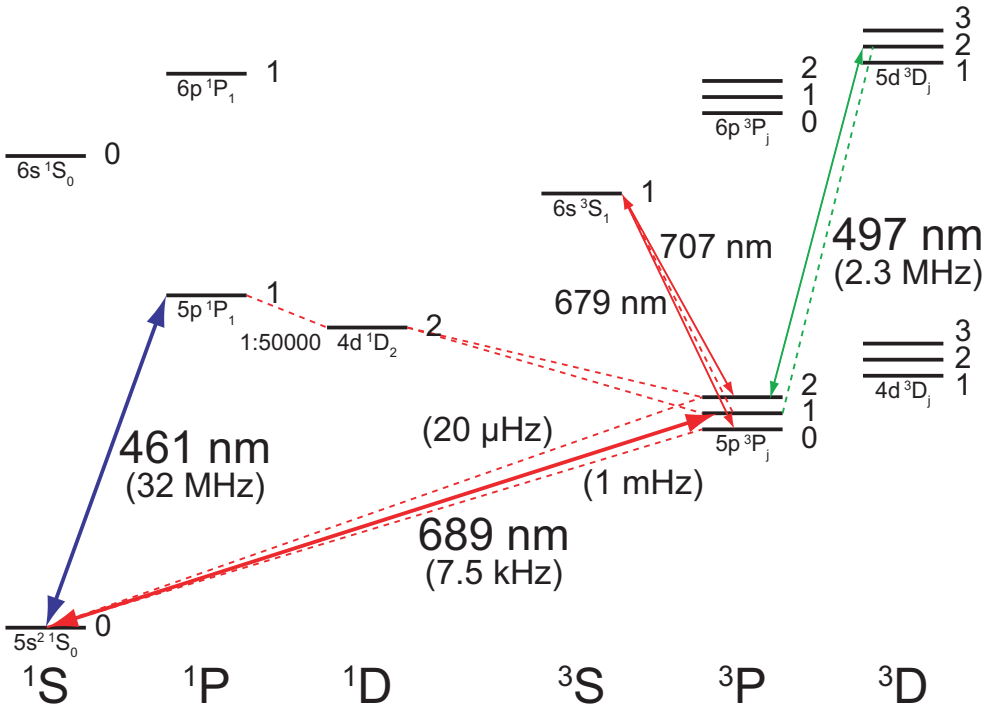

Figure 3.14: Optical transitions of Sr.

the imaging transition. The light for the MOT comes from the other output of the polarizing beamsplitter after the first tapered amplifier. It is sent through an optical fibre to obtain a good Gaussian profile. The power is then amplified to 500 mW using a second tapered amplifier[33]. A single-pass AOM for intensity control is placed in between the tapered amplifier and the fibre towards the MOT.

3.5.3 Laser System for Strontium

Strontium is an alkaline earth metal. Having two electrons in the outer *s*-shell results in a different energy level scheme compared to Li or K. Figure 3.14 shows the energy levels that are important for cooling and trapping of Sr atoms.

Exciting one of the $^1S_0$ electrons can result in either a singlet or a triplet excited state. The singlet transition of Sr has a wavelength of 461 nm with a linewidth of 32 MHz. The broadest of the triplet transitions has a wavelength of 689 nm with a linewidth of 7.5 kHz. The blue singlet transition is well suited to operate a Zeeman slower and a MOT similar to the case of alkali metals. The narrow linewidth of the red triplet transition allows to operate a MOT at very low temperatures down to 1 μK [99]. Since the capture velocity of the red MOT is too small to trap

[33] purchased from www.sacher-laser.com

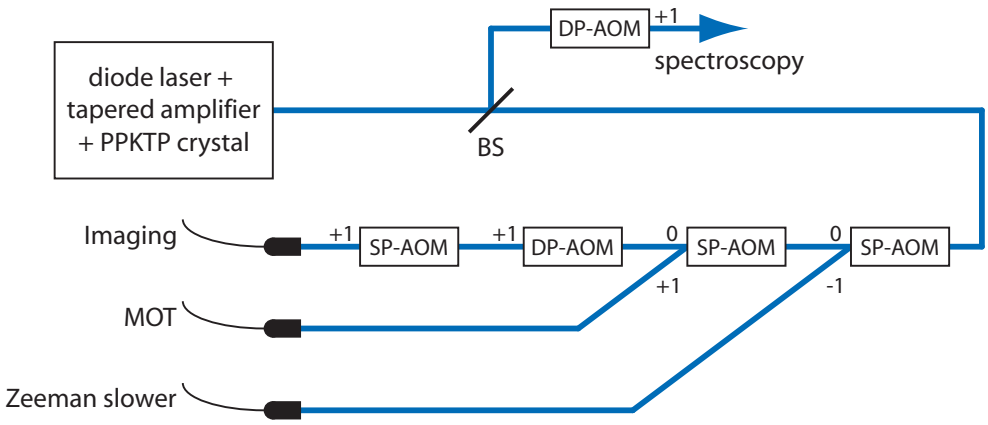

Figure 3.15: Optical concept for the 461 nm laser system. The propagation of the laser beams through the functional elements of the optical system is shown. For simplicity, mirrors, lenses and shutters are not shown as well as some wave plates for polarization corrections.

atoms out of a Zeeman slower, the typical sequence of a Sr experiment has two MOT phases. First, a blue MOT is produced, which is cold enough to be transferred into a red MOT.

The blue singlet transition is not a perfect cycling transition. It is possible to use it for a MOT but the loading rate and lifetime are very limited due to decay into a metastable state. The branching ratio from the $^1S_0$ into the $^1D_2$ state is 1:50000. From the latter state the atoms quickly decay into the two triplet states $^3P_{1,2}$. Since the lifetime of the $^3P_2$ state is on the order of several minutes, a repumping laser is required to bring the atoms back into the 461 nm cycling MOT transition. There are three possible repumping transitions. Light with 679 nm and 707 nm addressing the $^3S_1$ state can be used [100], a transition at 497 nm towards the $5d^3D_2$ state [101], or a 3 μm transition towards the $4d^3D_2$ state [102]. We decided to use the turquoise 497 nm, because a single laser would be easier to maintain. Furthermore, this repumper only requires a few mW of power, which can be achieved with a frequency-doubled diode laser without difficulty. The wavelengths of 497 nm is also well separated from all the other lasers used for Li, K and Sr and can be combined easily with the other beams using dichroic mirrors.

To summarize, our plan to work with Sr requires three laser systems at 461 nm, 497 nm and 689 nm. At the time of writing, only the blue singlet transition has been used to create a Sr MOT. But the design of many components of the setup required to take into account the future use of light with 497 nm and 689 nm wavelength.

The optical setup for Sr is much simpler than for Li or K, because no repumping light is needed at 461 nm. A conceptual drawing of this setup can be seen in Fig. 3.15. We use a frequency doubled diode laser system[34] to generate light at 461 nm. It consists of a Fabry Perot type semiconductor laser with an external grating for frequency stabilization. The output of the

[34]purchased from www.leosolutions.it

diode laser is amplified to 1300 mW using a tapered amplifier. The second harmonic of this light is generated with a periodically poled KTP crystal inside a bow tie cavity. This yields about 300 mW of light at 461 nm.

A part of the output power is split off to be used for locking the laser to the atomic transition of Sr. As for the 671 nm setup, we use the modulation transfer method [95] and a commercially available high-temperature spectroscopy cell[35] with Sr vapor. A Fabry Perot spectrometer and a wavemeter are used to monitor the lineshape and frequency of the laser.

The light for the Zeeman slower is produced using the -1^{st} order of a single-pass AOM. Its zeroth order is sent through a double-pass AOM giving the light needed for the MOT transition. During the imaging sequence, these two AOMs are switched off and the laser beam passes both devices. This light is sent through another two AOMs in double and single-pass configuration to be used for imaging.

3.6 Zeeman Slower

A Zeeman slower is used to decelerate the atoms in the atomic beam [76, 103]. Due to the high temperatures in the oven, the atoms have an initial velocity of several 100 m/s while the MOT can only trap atoms with few 10 m/s. A Zeeman slower decelerates the atoms using the light force of a counter-propagating resonant laser beam. As the velocity $v(z)$ of the atoms decreases along the z-axis, the Doppler shift of the laser beam is changed. To keep the light resonant to the atomic transitions, a magnetic field $B(z)$ is applied. The field varies along the beam axis corresponding to the local velocity of the atoms along this axis. Using one Zeeman slower for several species poses the question whether a design compatible with all our elements can be developed.

3.6.1 Theory of a Multi-Species Zeeman Slower

The force of a homogenous resonant laser beam with a wavevector $\vec{k}$ on an atom is caused by the absorption of photons from a certain direction and the spontaneous emission into an arbitrary direction. If many of these optical cycles are happening, the momentum transfer during the spontaneous emission cancels out and only the momentum of the absorbed photons is transferred to the atom. An analytic expression of this force can be calculated by solving the optical Bloch equations [103]. The resulting force is

$$\vec{F} = \frac{\hbar \vec{k} s_0 \gamma/2}{1 + s_0 + (2\delta/\gamma)^2}. \tag{3.1}$$

The parameter γ is the linewidth of the optical transition and δ the detuning between the laser frequency and the optical transition, s_0 is the so-called saturation parameter. It is defined as

[35] purchased from www.leosolutions.it

$s_0 = I/I_s$ with the saturation intensity $I_s = hc\gamma k^3/(24\pi^2)$. The saturation parameter reflects the effect that the force saturates for a higher laser intensity. At intensities lower than I_S, the rate of absorption - spontaneous emission cycles is limited by the laser intensity. At intensities above I_S, the rate is limited by the finite excited state lifetime (27 ns for Li and K, 5 ns for Sr). High intensities lead to an increase in stimulated emissions, but absorption - stimulated emission cycles do not contribute to the force. This limits the force and the acceleration $\vec{a}$ of an atom with mass M to a maximal value of

$$\vec{F}_{\text{max}} = \frac{\hbar\vec{k}\gamma}{2} \quad \text{and} \quad \vec{a}_{\text{max}} = \frac{\hbar\vec{k}\gamma}{2M}. \tag{3.2}$$

These maximum values restrict the possible deceleration and the magnetic field profile of a Zeeman slower.

The profile of the magnetic field should cancel the spatial variation of the Doppler shift of the decelerating atoms. To fulfill the resonance condition, the atomic angular transition frequency ω_0 shifted by the doppler effect by $-kv(z)$ and the Zeeman effect by $\mu' B(z)/\hbar$ must be equal to the laser angular frequency ck:

$$\omega_0 - kv(z) + \mu' B(z)/\hbar = ck. \tag{3.3}$$

$\mu' = (g_e m_e - g_g m_g)\mu_B$ is the effective magnetic moment between the ground state and the excited state with the magnetic quantum numbers m_g, m_e and the Landé g-factors g_g, g_e.

To calculate the axial profile of the magnetic field, we assume a constant deceleration of $a = \eta a_{\text{max}}$ with $0 < \eta < 1$. The velocity is decreased along the z-axis from an initial velocity v_0 to $v(z) = \sqrt{v_0^2 - 2az}$. Together with the resonance condition we get

$$B(z) = \frac{\hbar\delta}{\mu'} + \frac{\hbar k v_0}{\mu'}\sqrt{1 - \frac{2az}{v_0^2}} = \Delta B + B_0\sqrt{1 - \frac{z}{z_0}}. \tag{3.4}$$

$\Delta B = \hbar\delta/\mu'$ is an overall shift of the magnetic field related to the detuning between the laser beam and the optical transition. This shift does not influence the initial velocity or the deceleration. Therefore, the performance of the Zeeman slower is completely determined by the two variables B_0 and z_0. They are connected to the other parameters by the equations

$$B_0 = \frac{\hbar k v_0}{\mu'} \quad \text{and} \quad z_0 = \frac{v_0^2}{2a} = \frac{M v_0^2}{\eta\hbar k\gamma}. \tag{3.5}$$

z_0 is approximately the geometrical length of the Zeeman slower and B_0 defines the maximal velocity v_0 of atoms that are captured by the Zeeman slower. Both variables have to be chosen within a range that keeps $0 < \eta < 1$. Otherwise, the atoms could not be decelerated fast enough to follow the resonance condition. Most Zeeman slowers work well within the regime of about $1/3 < \eta < 2/3$. For higher values of η, field inhomogeneities may locally increase η above 1, leading to a breakdown of the slowing process. For lower values of η the slowing becomes

	^{6}Li	^{23}Na	^{40}K	^{87}Rb	^{133}Cs	^{88}Sr	^{174}Yb
^{6}Li	1	**0.65**	0.10	0.04	0.02	**1.14**	**0.78**
^{23}Na	**1.53**	1	0.16	0.07	0.03	**1.74**	**1.19**
^{40}K	9.68	6.31	1	0.43	0.19	11.00	7.51
^{87}Rb	22.55	14.70	2.33	1	0.43	25.62	17.50
^{133}Cs	51.86	33.82	5.36	2.30	1	58.92	40.26
^{88}Sr	**0.88**	**0.57**	0.09	0.04	0.02	1	**0.68**
^{174}Yb	**1.29**	**0.84**	0.13	0.06	0.02	**1.46**	1

Table 3.2: Ratio of the deceleration parameters, $\eta_{\text{leftcolumn}}/\eta_{\text{upperrow}}$, for a two-species Zeeman slower. Values between 0.5 to 2.0 are emphasized in bold.

inefficient. At the same time, v_0 needs to be high enough to capture a sufficient fraction of the atoms in the velocity distribution of the atomic beam to achieve a good loading rate for the MOT.

The model developed so far allows us to investigate the behavior of a Zeeman slower for different species. For a given design, the length of the slower cannot be changed and z_0 is fixed. In contrast, the magnetic field can be changed by varying the current in the Zeeman slower coils. However, the latter possibility would require several consecutive loading sequences of the MOT, which may be unfavorable. Therefore, our first question is: What elements can be decelerated by a common Zeeman slower without changing the magnetic field? The answer depends on the ratio

$$\frac{\eta_a}{\eta_b} = \frac{M_a \mu_a'^2 k_b^3 \gamma_b}{M_b \mu_b'^2 k_a^3 \gamma_a} \tag{3.6}$$

for a combination of two elements a and b. If this ratio is close to 1, both elements can be slowed with an efficient value around $\eta \approx 0.5$. If η_a/η_b is to small or to large, one element would not be slowed efficiently or one η would become larger than 1 leading to a breakdown of the slowing process for this element. Table 3.2 lists the values of η_a/η_b for some common elements. Values between $0.5 - 2.0$ are emphasized in bold. These combinations would work with $1/3 < \eta < 2/3$ for both elements.

If two elements cannot be decelerated efficiently with the same magnetic field, two loading stages with different magnetic fields may work. Therefore, the second question is: What length z_0 and what field B_0 do we need to reach a given capture velocity v_0? Figure 3.16 shows v_0/v_{rms} and B_0 in dependance of the length z_0 for $\eta = 0.5$. As different elements can have very different vapor pressures, the typical temperature used for the oven can vary widely. This leads to different velocities of the atomic beams. To take that into account, Fig. 3.16 shows the capture velocity

[36]The curve for the relative capture velocity of K overlaps with the one for Rb.

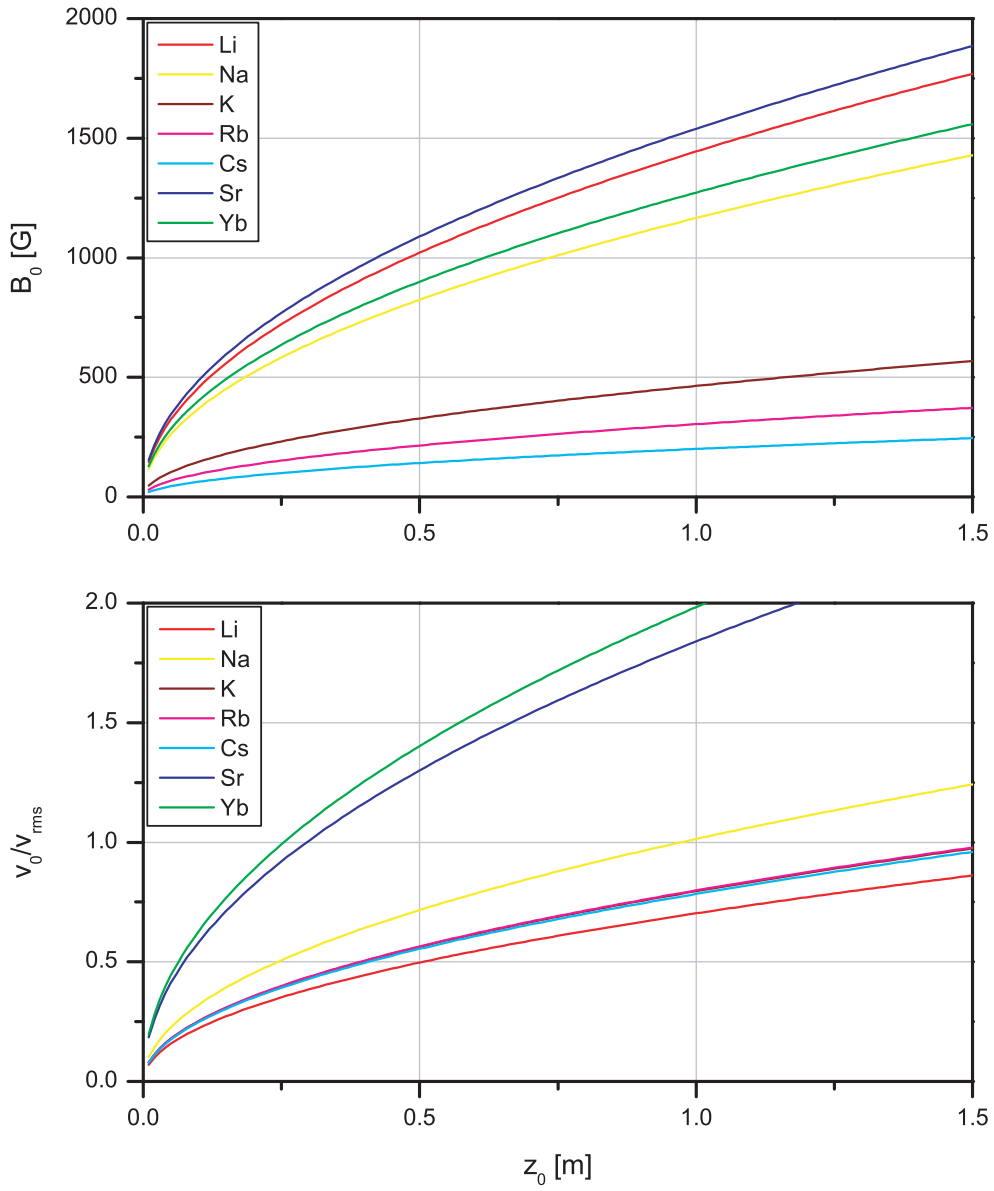

Figure 3.16: Required magnetic field and obtained relative capture velocity of a Zeeman slower with $\eta = 0.5$ in dependance of the length z_0 for different elements[36].

normalized by the root mean square velocity of the atomic beam

$$v_0/v_{\text{rms}} = \sqrt{\frac{\eta\hbar k\gamma z_0}{4k_B T}}. \tag{3.7}$$

The temperature for each element was set to a typical value[37]. The formula for the magnetic field is given by

$$B_0 = \sqrt{\frac{\eta\hbar^3 k^3\gamma z_0}{\mu' M}}. \tag{3.8}$$

The normalized capture velocity of ^{6}Li has the lowest value, mainly because the low mass causes high absolute velocities. Typical Zeeman slowers for Li have a length between 0.5 and 1.0 m with a capture velocity from 0.5 to 1.0 times v_{rms}. These configurations lead to sufficient loading rates for Li MOTs. Figure 3.16 shows, that length values between 0.5 and 1.0 m are enough to capture an even larger part of the velocity distribution for all other elements. The required fields for these dimensions are between 1000 G and 1500 G, which is technically feasible.

Another design parameter is the total shift ΔB of the magnetic field. Shifting the magnetic field by a constant value has several favorable consequences. The light used for slowing the atoms can be detuned by many linewidths and does not influence the atoms trapped in the MOT. Additionally, the maximum absolute value of the field profile $B(z)$ can be reduced. This leads to smaller coils and less power consumption and heating. In this case the field changes the direction within the length of the slower. The relative orientation between the atomic spin and the field flips at this position. A Zeeman slower of this type is therefore called spin-flip Zeeman slower. A disadvantage is the necessity of generating a larger field at the end of the Zeeman slower close to the MOT. This requires larger coils at a place where space is very restricted. The relation between the field shift and the light detuning also determines the final velocity of the atoms.

3.6.2 The Zeeman Slower Design for Li, K and Sr

For our three elements, Li, K and Sr, we can build a Zeeman slower that works simultaneously for Li and Sr. For slowing K, we have to lower the magnetic field by reducing the current. This fits our main strategy to optimize the machine for Li, which is used as the coolant for the K atoms. We have written a detailed simulation for the Zeeman slower based on the concept presented in [88]. The results showed, that small variation in the length or the magnetic field do not change the loading rate of the MOT a lot. More important is the distance between the end of the Zeeman slower and the MOT. The transversal velocity of the atoms leads to a very divergent beam if the atoms have slow longitudinal velocities as at the end of the slowing process.

A scheme of our design for the Zeeman slower can be seen in Fig. 3.17. The geometry of the windings is indicated by the blue and green dots. The optimal field is shown by the black line,

[37] Temperatures: ^{6}Li: 400°C, ^{23}Na: 350°C, ^{40}K: 200°C, ^{87}Rb: 180°C, ^{133}Cs: 100°C, ^{88}Sr: 500°C, ^{174}Yb: 400°C

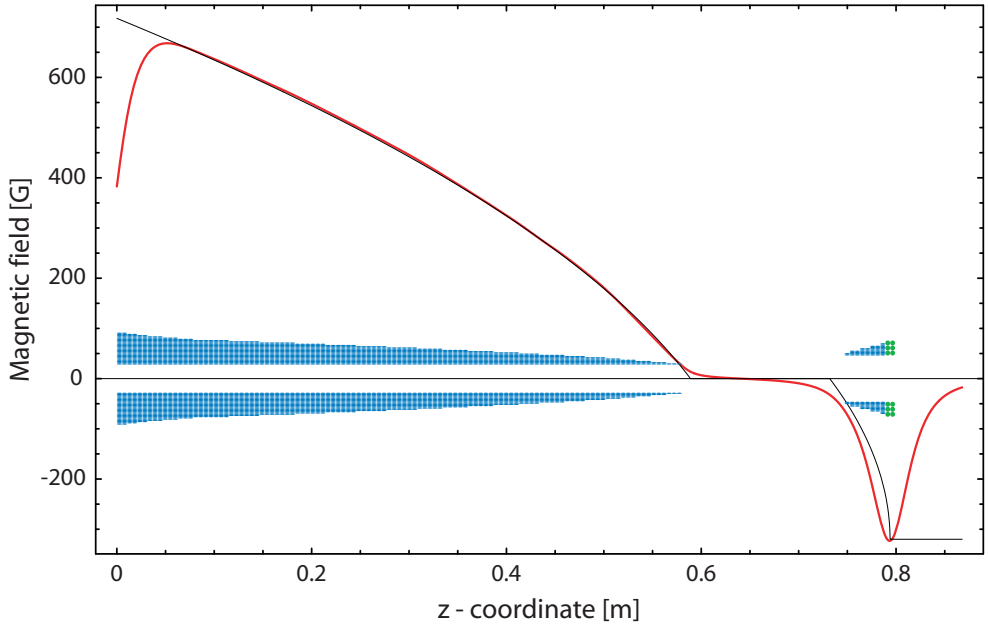

Figure 3.17: Magnetic field and coil profile of the Zeeman slower. The black line shows the calculated field for a uniform deceleration. The red line shows the calculated field of the coils. The geometry of the coils is indicated by the blue (low current sections 1 and 2) and green (high current section 3) circles.

while the field produced with the coils is drawn in red. We used the following design parameters for the field profile for Li atoms:

$$\eta = 0.4, \quad z_0 = 0.65 \text{ m}, \quad B_0 = 1040 \text{ G}, \quad \Delta B = -320 \text{ G}.$$

Our Zeeman slower consists of three sections. The first section uses several hundred windings of $5.0\text{x}1.0$ mm^2 copper wire (thickness of the isolation: 0.2 mm). This wire generates the first and largest part of the magnetic field that captures the atoms from the atomic beam. The wire has been wound in 12 pairs of radial layers resulting in 12 different coils with decreasing lengths. They are fixed using cable ties. The coils are connected in series but could be driven by individual currents for a detailed optimization of the slower or if one of the coils breaks. This first part is wound around a double wall steel tube of the vacuum chamber with an outer diameter of 28 mm. Water can flow through the space between the two walls of the tube to cool the wires from the center. The outer part of the coils is surrounded by a plastic box, which is cooled using air. The box also suppresses air turbulence on the optical table. The next part of the Zeeman slower is separated by the spin-flip zone, where no coils are installed. This zone is placed at the location of the relatively bulky bellow where no tight coils could be wound (see for example Fig. 3.7). The second part is made of the same $5.0\text{x}1.0$ mm^2 copper wire. It is wound around a shell made of non-magnetic steel, which is installed around the glass to metal transition of the glass cell. This allows us to place the end of the Zeeman slower as close to the MOT as possible. To realize the steep gradient of the end of the field profile, we use a third section, which consists of

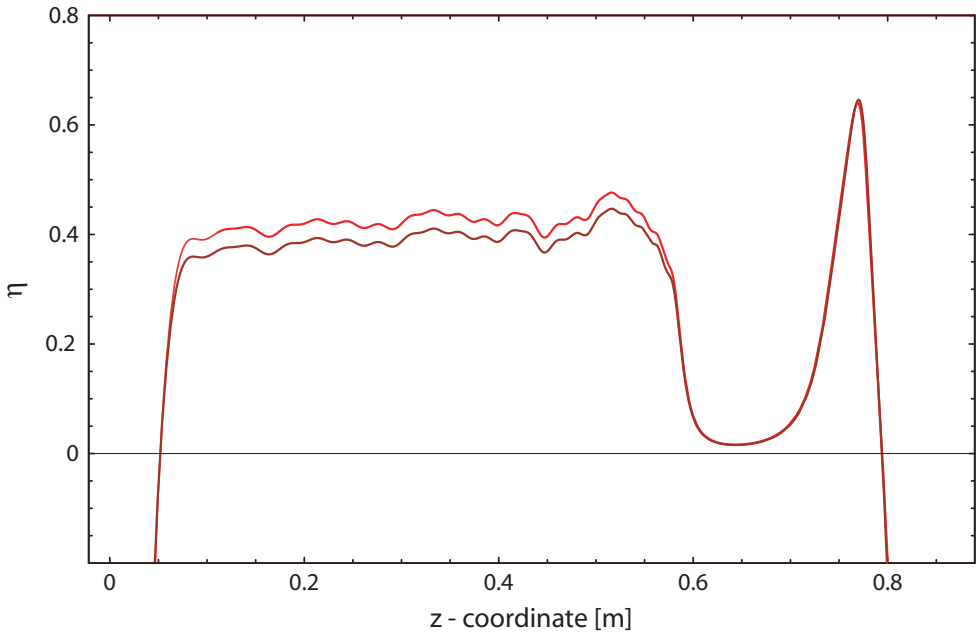

Figure 3.18: Deceleration parameter η for the Zeeman slower using two different current configurations with $I_{\mathrm{K}} = 0.3 \cdot I_{\mathrm{Li}}$. The red line shows the values for Li, the brown line for K.

six windings of a hollow copper wire with a square profile of 4.0x4.0 mm^2 (inner dimensions: 2.0x2.0 mm^2). The hollow wire can be water-cooled very efficiently, which allows to use high currents to get a steep gradient in a compact way close to the MOT. The current in this third part also allows us to optimize the escape velocity of the atoms that leave the Zeeman slower. This is an important parameter because if it is too high, the MOT cannot capture the atoms, if it is to low, the divergence of the atomic beam is very large and only few atoms reach the MOT. This last part of the Zeeman slower can be seen in the photos of Fig. 3.21b and c.

The field depicted in Fig. 3.17 was calculated using currents of $I_1 = 13.5$ A, $I_2 = -5$ A and $I_3 = -250$ A for the three sections. The final currents used in the experiment are found by optimizing the loading rate of the MOT. The deceleration parameter η for Li and K is shown in Fig. 3.18. For Li, it has been calculated with the field values used for figure 3.17 while for K, all currents have been multiplied with a factor of 0.3. Again, a detailed optimization is done experimentally by optimizing the MOT loading.

The Zeeman slower also produces a magnetic field at the location of the MOT. This field has to be compensated. We use a compensation coil installed on the other side of the glass cell. It is designed with the same wire as used for the high current part of the third section of the Zeeman slower and consist of 8 windings. They can also be seen in the photos of Fig. 3.21b and c.

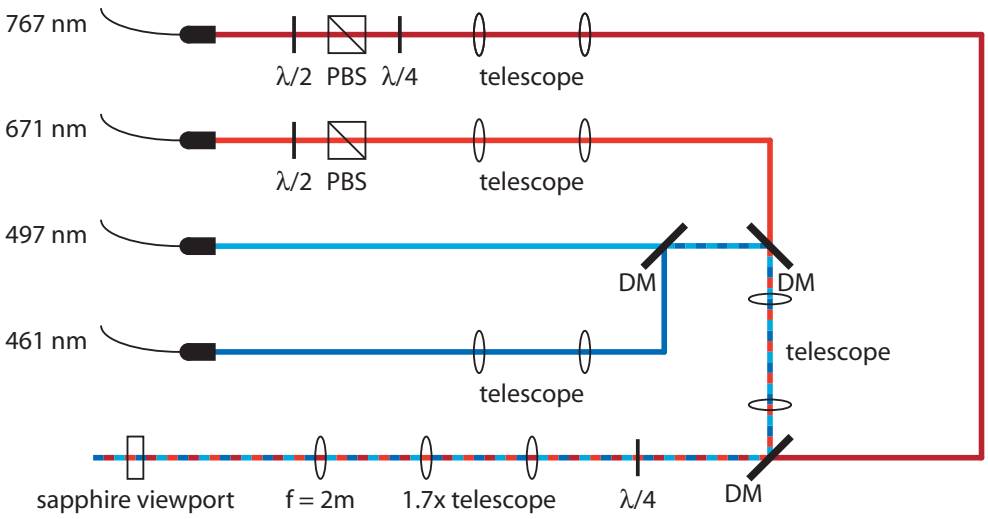

Figure 3.19: Optical concept for the Zeeman slower laser beam. The different wavelengths are overlapped using dichroic mirrors (DM). Telescopes are used to adjust the beam sizes individually. The polarization is controlled using polarizing beamsplitters (PBS) and wave plates. For simplicity, the beam steering mirrors are not shown.

3.6.3 The Zeeman Slower Laser Beam

The laser beam for the Zeeman slower must contain all the different wavelengths for Li, K and Sr. The required light is generated on different optical tables and sent to the vacuum chamber table using optical fibres. An optical setup combines all wavelengths using dichroic mirrors and forms a converging beam, which is directed into the vacuum chamber. An additional challenge is the sapphire viewport of the vacuum chamber. Sapphire is a birefringent material and the viewport will change the polarization of the Zeeman slower beam. As the various wavelengths will be affected differently, the polarization must be corrected by suitable wave plates.

The concept of the setup is shown in Fig. 3.19. After the fibre output collimators a combination with a half-wave plate and a polarizing beamsplitter assures stable linear polarization. This was implemented for the 671 nm and 767 nm beams to increase the shot to shot stability of the machine. The polarization of the 767 nm light can be modified using a subsequent wave plate. Afterwards, the beams are expanded using telescopes. This allows to individually adjust the beam size for optimal performance of each element. Also the 461 nm light passes a telescope after the output coupler. The 461 nm beam can be overlapped with the 497 nm beam using a longpass dichroic mirror. The 671 nm beam is now overlapped with the blue beams for Sr using another longpass dichroic mirror. Up to this point, the beam sizes where limited to be able to use 25 mm steering mirrors in order to keep the setup compact. Therefore, another telescope after the dichroic mirror now increases the beam size to a diameter of approximately 25 mm. Finally, a third longpass dichroic mirror adds the 767 nm light. All the dichroic mirrors are only specified for linear polarization. They can alter the polarization state of circular polarized light.

The Zeeman slower requires circular polarized light. This is produced after mixing the different wavelengths using a custom made achromatic quarter-wave plate[38] with a 1" aperture. To encounter the birefringence of the sapphire viewport for the individual colours, the polarization of the different beams is fine-tuned using this quarter-wave plate and the quarter-wave plate in the 767 nm beam by optimizing the MOT loading. The geometry of the Zeeman slower beam is defined by another 1.7x telescope to reach a beam diameter of 42 mm. This beam is now focused using a $f = 2$ m lens. This way, the converging Zeeman slower beam is better overlapped with the counterpropagating diverging atomic beam.

The fluorescence of the Zeeman slower beam and the atomic beam can be monitored through the viewports of the first differential pumping section using two CCD cameras in orthogonal directions. The fluorescence signal and the reflections of the laser beam off the steel parts of the vacuum chamber are very useful to align the laser beam coaxial to the atomic beam. Photos of the Li and the Sr beam can be seen in Fig. 3.6.

3.7 Electromagnetic Field Coils

Magnetic fields are a powerful tool for working with atomic quantum gases. They are used for trapping the atoms in magneto-optical traps or magnetic quadrupole traps. The magnetic field can be used to change the interaction properties between the atoms if a Feshbach resonance is addressed. Furthermore, a magnetic field shifts the resonance frequency for imaging and can be used for optical pumping. A curvature of the field can be used as additional axial confinement of atoms in an elongated dipole trap or a field gradient for Stern Gerlach separation of different spin states. To realize all these different applications, a system of many magnetic coils is required. The coils have to fulfill several criteria like producing high fields, fields in different directions, homogeneous fields or fields with a strong gradient or allowing fast field ramps. In addition, the stability of the magnetic field is an important factor for the shot to shot stability of the machine. We have build a powerful system of different coils to fulfill many of these requirements. A large part of the work was done by Clarice Aiello and is described in Ref. [72].

The major part of the coils for the magnetic fields is located in dedicated boxes very close above and below the glass cell. A CAD profile through the center of the coil box is shown in figure 3.20 and a series of photos is presented in figure 3.21. The box for the coils has to support them as stable as possible around the glass cell. At the same time, it is favorable to keep the walls of the box as thin as rigidity allows to be able to place the coils closer to the glass cell. Additionally, the box should not be made of conductive material to avoid eddy currents. We used glass fibre reinforced polyamide 66, an engineering plastic with high strength. The coils have been wound on an aluminium form to achieve the desired spiral form with high accuracy. Afterwards, they were placed inside the box and filled with epoxy[39]. Several thermistors are

[38] purchased from www.novaphase.com
[39] Loctite Hysol RE2039/HD3561

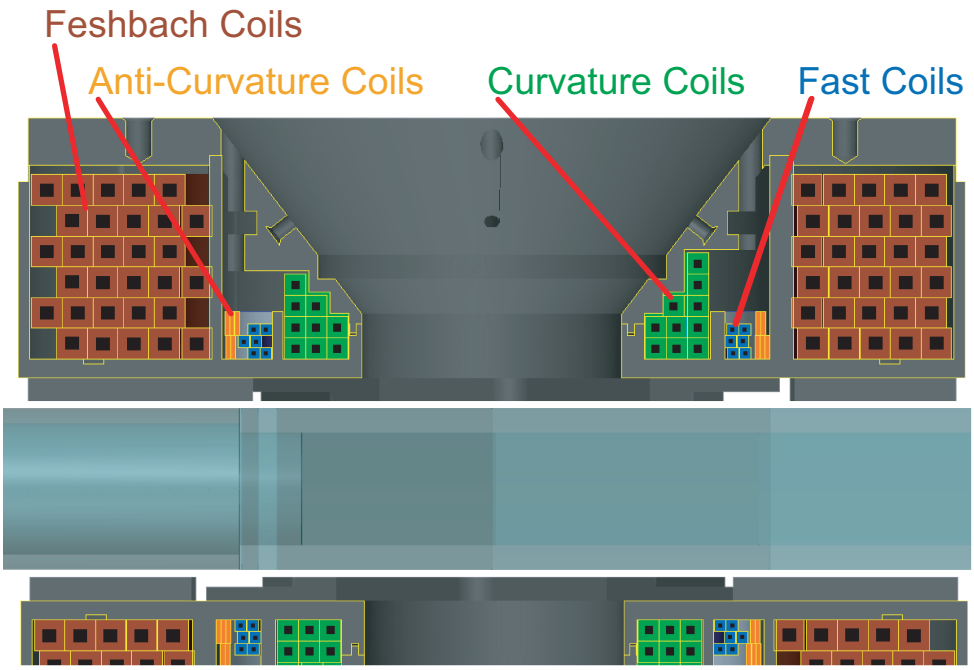

Figure 3.20: Profile of the main coils. The coils are located in a black polyamide box around the glass cell. The spiral shape of the coils breaks the mirror symmetry of the profile. More details of the box and the coils are discussed in the text.

installed inside the box to measure the operation temperature. The box cover presses the coils into the intended position during the hardening of the epoxy. The lower box is fixed with six steel posts onto the optical table. The upper box is fixed to the lower one by placing it onto four polyamide spacers and screwing both boxes together. The big central hole of the upper coil is protected by a cylindrical plastic tube (see the upper center of figure 3.21d). This prevents small parts (screws, optics. . .) from falling onto the glass cell. The box contains the following coils.

The "Feshbach coils" are designed to reach magnetic fields up to 4000 G with a current up to 1200 A. They are placed fulfilling the Helmholtz condition for a homogeneous field. They are made of 30 windings using a hollow copper wire with square profile isolated with a glass fibre cladding (outer profile: 6x6 mm^2, inner profile: 3x3 mm^2).

The "curvature coils" are designed to reach a high field gradient. They can produce axial field curvatures of up to 59 G/cm^2 using 600 A. They are made of 10 windings using a hollow copper wire with square profile isolated with a glass fibre cladding (outer profile: 4x4 mm^2, inner profile: 2x2 mm^2).

The "anti-curvature coils" are designed to apply small or fast field corrections opposite to the curvature coils. They are made of 6 windings of 5x1 mm^2 isolated copper wire.

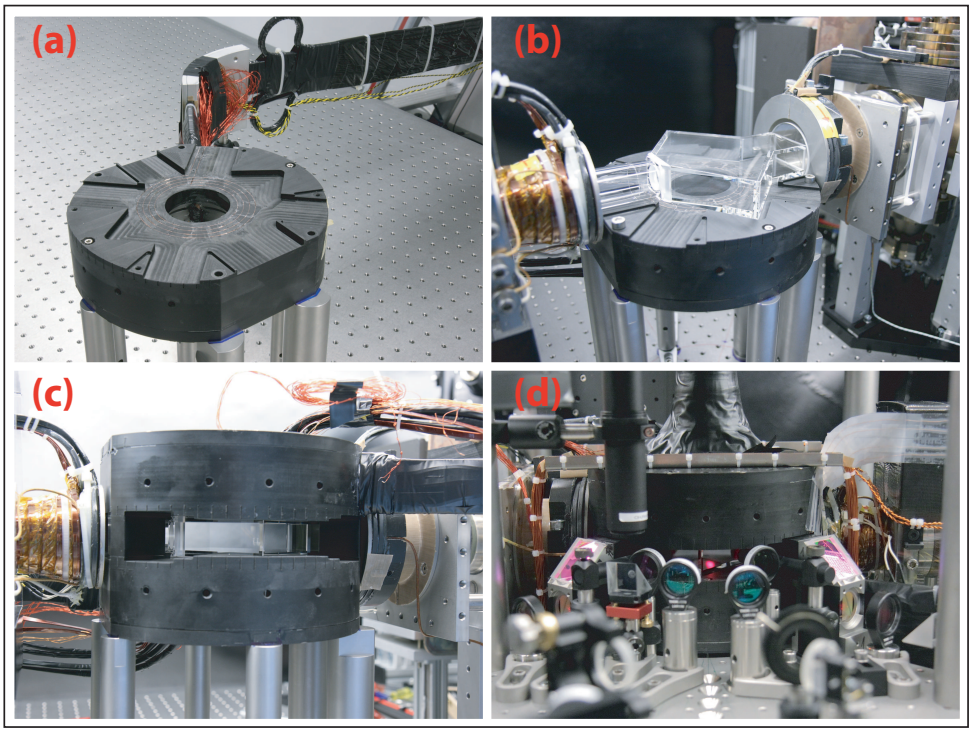

Figure 3.21: Figure (a): The lower coil box is placed on six steel posts. The milled cut for the glass cell is visible as well as the four windings of the thin rf-coils around the central hole. The connection wires of the Feshbach coils leave the box towards the top of the picture. Figure (b): The lower coil box installed below the glass cell. The picture also shows the last coils of the Zeeman slower and the compensation coils. Figure (c): Both coil boxes installed around the glass cell. The thick connections for the Feshbach coils leave the upper box on the right side. The connections of the other coils can be seen above and below the boxes. Figure (d): The glass cell with the coil boxes and optics. This picture also shows one horizontal field coil wound around both coil boxes. The upper box is shielded by a plastic cylinder and black plastic tape. The red Li MOT can be seen in the center.

The "fast coils" are designed for fast sweeps of the magnetic field in addition to the Feshbach coils. They are also placed fulfilling the Helmholtz condition. They are made of 6 windings using a hollow copper wire with square profile isolated with a glass fibre cladding (outer profile: 2x2 mm^2, inner profile: 1x1 mm^2).

Additional to these four main coils, four small coils are places inside the coil box, which can be used to generate radio frequency (rf) signals. Two more rf-coils are glued to the bottom of the box at a distance of less than 1 mm from the glass cell (see figure 3.21a and 3.21b). The rf-signal is generated using the DDS modules of the computer control system (see section 3.11).

The signal is amplified using our 2W rf amplifier module and a commercial 75W rf amplifier[40]. This system allows us to address a frequency range between 10 kHz and 135 MHz.

The coils described so far all produce fields vertical to the glass cell. Fields on the axis of the atomic beam can be produced using the last coil of the Zeeman slower and its compensation coil (see section 3.6). To address the third axis, we installed another pair of coils by winding it around the two coil boxes after they were installed around the glass cell. The vertical sides of these coils can be seen in Fig. 3.21d. The horizontal sides are covered by metal railings used for holding them in place. Finally, a big cage (1.5x1x0.8 m^2) made of 6 rectangular coils surrounds the central region of the experiment. These coils can be used to compensate the earth magnetic field or other external fields. Table 3.3 lists the available coils with some important specifications.

Special attention has been paid on the installation of the high current hollow copper wires and the cooling water connections. To avoid spilling water on the optical table, the hollow wires are routed to the edges of the optical table. They are connected to copper bars (cross section between 400 to 1200 mm^2), which can conduct the high current without water cooling. The hollow copper wires are routed further below the table where they are connected[41] to the flexible tubes[42] of the water cooling system. The current conducting copper bars are connected to flexible high current cables, which lead into the basement below the laboratory to the power supplies.

3.7.1 Power Supplies

We need several power supplies to generate the current for the magnetic field coils. All the power supplies are installed in the basement below the laboratory. This reduces the heat, noise and equipment in the laboratory leading to a more stable and comfortable environment. The analog controls of the power supplies are connected to the bus system of the computer control using optocouplers[43] to separate the electrical circuits. The power supplies are connected to a high-current switch board. This board uses several IGBTs[44] for a fast switch-off. Relays[45] can change between a Helmholtz and quadrupole configuration. A circuit diagram of the switch board is presented in figure 3.22. All IGBTs are protected with varistors. If a coil cannot be driven with the maximal current of an attached power supply, we add a fuse in series with the coil for protection. Water-cooled high current diodes[46] are used if a protection against currents in opposite directions is necessary. Each IGBT is driven by a dedicated driving circuit, which is connected to the computer control system via an opto-coupler. All IGBTs are installed on water-cooled copper plates.

[40] model FLL75 from www.frankonia-emv.com
[41] using connectors from www.swagelok.com
[42] model PB-8 from www.swagelok.com
[43] design by Todd Meyrath, see www.ph.utexas.edu/ meyrath/
[44] Mitsubishi CM1400DU-24NF, CM600DU-24NF, CM400DY-24NF
[45] model Schuetz S 195 SE/3/24V
[46] model SD600N/R SERIES from www.irf.com

	N	I_{max} [A]	$\frac{B}{I}$ $[\frac{G}{A}]$	$\frac{\partial B}{\partial zI}$ $[\frac{\text{G}}{\text{cmA}}]$	$\frac{\partial B}{\partial rI}$ $[\frac{\text{G}}{\text{cmA}}]$	$\frac{\partial^2 B}{\partial^2 zI}$ $[\frac{\text{G}}{\text{cm}^2\text{A}}]$	$\frac{\partial^2 B}{\partial^2 rI}$ $[\frac{\text{G}}{\text{cm}^2\text{A}}]$
Feshbach coils (Helmholtz)	30	1200	3.28	0	0	0	0
Feshbach coils (quadrupole)	30	1200	0	0.52	0.28	0	0
Curvature coils (Helmholtz)	10	600	1.51	0	0	0.20	0.098
Curvature coils (quadrupole)	10	600	0	0.64	0.35	0	0
Fast coils (Helmholtz)	6	200	1.0	0	0	0.0032	0.0015
Zeeman slower section 3	6	200	−0.0180	0.0040	0	0.0013	0.00063
Zeeman slower compensation	12	200	0.120	0.026	0	0.0072	0.0036
Horizontal coils (Helmholtz)	42	5	3.0	0	$n.c.$	0.29	$n.c.$
Horizontal coils (quadrupole)	42	5	0	0.38	$n.c.$	0	$n.c.$
Earth compensation vertical (Helmholtz)	20	6	0.25	0	$n.c.$	$n.c.$	$n.c.$
Earth compensation axial (Helmholtz)	20	6	0.19	0	$n.c.$	$n.c.$	$n.c.$
Earth compensation horizontal (Helmholtz)	20	6	0.091	0	$n.c.$	$n.c.$	$n.c.$

Table 3.3: Properties of the magnetic field coils: Number of windings N, maximal applied current I_{max}, magnetic field B per current I and its first two derivatives in axial (z) and radial (r) direction. Values not calculated are indicated by $n.c.$

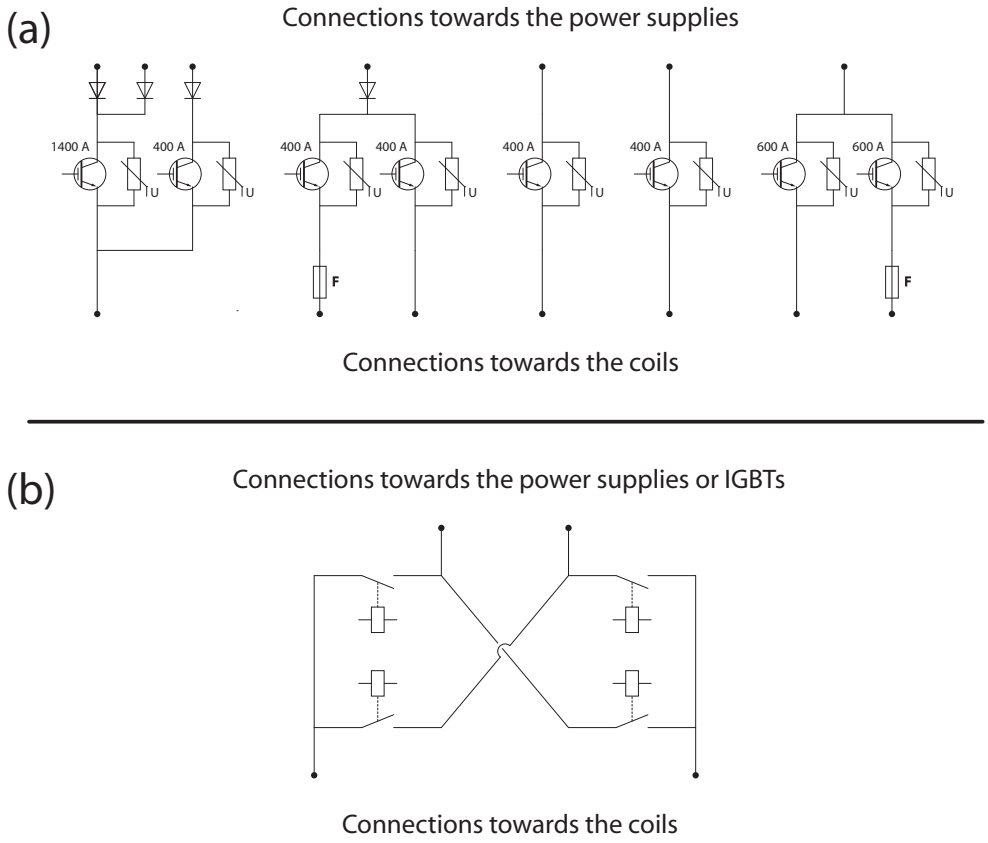

Figure 3.22: Circuit diagram of (a) the IGBT switch board and (b) the relays.

The current of the coils can be actively stabilized using current transducers either after or before the switching board. They measure the current and a PID controller regulates the power supply output. However, in many cases, the passive stability of the power supplies is sufficient.

We have a number of power supplies available, which are listed in table 3.4. The required magnetic fields for the different coils depend on the experiments. Therefore, the power supplies are connected to the coils depending on these requirements. The table lists the most typical configurations.

3.7.2 Water Cooling System

Five of the coils, the Feshbach coils, the curvature coils, the fast coils, the high current coil of the Zeeman slower and its compensation coil are made of hollow copper wires and can be water-cooled. Water cooling is indispensable for working with high currents to produce high

	$I_{\max}$	$U_{\max}$	typically used for
Lambda ESS 30-500	500 A	30 V	Feshbach coils
Lambda ESS 30-500	500 A	30 V	Feshbach coils
Delta SM30-200	200 A	30 V	Zeeman slower high current section
Delta SM30-200	200 A	30 V	anticurvature coils
Delta SM30-200	200 A	30 V	fast coils
Danfysik 858	90 A	5 V	ultrastable fields with Feshbach or curvature coils
Delta SM1540-D	40 A	15 V	Zeeman slower low current section
Delta SM1540-D	40 A	15 V	Zeeman slower compensation coil
EA-PS 3016-20 B	20 A	16 V	Zeeman slower low current section

Table 3.4: Available power supplies with their maximal current $I_{\max}$ and their maximal voltage $U_{\max}$.

fields or curvatures. Therefore, we installed a powerful cooling system[47] in the basement below the laboratory. It has three separated circuits, one for high pressure (up to 20 bar) and two for low pressure (up to 4 bar) cooling water. The high pressure system has eight channels, which can be used in parallel. Six of them are used for the Feshbach coils. Each of the two coil parts consists of three double windings. The double windings can be cooled in parallel while the electrical connection is made in series. The remaining two high pressure channels are used for the curvature coils. The low pressure circuits have 8 and 10 available channels, which are used for the cameras, the spectroscopy cells, beam dumps, the Zeeman slower coils, the fast coils, the IGBT switching board and for cooling some lasers. The pressure of the low pressure system can be regulated individually for all 18 channels. The water channels are also equipped with individual flux meters. If the flow through one of the coils (or other devices) falls below a certain threshold, an alarm signal is sent to the security system. Another possibility for failure are leaks. Therefore, two precision flux meters measure the water flowing through the inputs and through the outputs. The security system is presented in more detailed in section 3.11.

3.8 Optical Access Multiplexing

An experiment with two or more elements has to handle laser beams with several optical wavelengths. At the same time, the optical access into the glass cell is very limited, especially for directions with low aberrations. The design of our glass cell (see section 3.4) includes three orthogonal axis for which at least one wall of the glass cell is perpendicular to the laser beams. These axis are required to achieve optimal imaging quality and high resolution dipole traps. Additionally, the six laser beams for the MOT also require a large aperture. This section presents

[47] custom system purchased from www.van-der-heijden.de

our concept, which allows us to combine all the different laser beams for the MOT, for imaging and for the dipole traps.

The overall concept is sketched in Fig. 3.23. In a first step, the light for the MOT is split up into six parts using a commercial fibre cluster system for each of the three wavelengths. The next step is to combine the three wavelengths for all six beams. This is done using six MOT mixing boxes with dichroic mirrors. The beams for the imaging pulses are also combined using dichroic mirrors. To overlap the beams for the MOT with the beams for the imaging pulses, a polarizing beamsplitter is used. Finally, laser beams for dipole traps (with 532 nm or 1064 nm) can be added with another dichroic mirror. To focus the dipole trap laser beam, we use a 70 mm lens right in front of the glass cell. As the MOT and imaging beams require convergent beams, compensating lenses are placed in front of the polarizing beamsplitter. The counterpropagating beam is combined the same way, but the imaging pulse optics is replaced by the camera and its optics. In the following, the different parts will be presented in more detail.

The fibre port clusters for generating six MOT beams out of one input beam were developed by Schäfter+Kirchhoff GmbH[48] (see Fig. 3.24). They have one input fibre, which delivers a collimated beam. The beam passes several half-wave plates and polarizing beamsplitters. The five wave plates allow to distribute the power among the six output ports. The six output beams are coupled into six optical fibres. The whole system is very compact, completely closed and has a very good long term stability. A build in photodiode allows to monitor the input power. Using optical fibres for the output beams results in a clean Gaussian profile of the MOT beams. The main disadvantage is the loss of optical power due to the additional fibre coupling. But for our three species setup, stability, compactness and ease of operation are very important and we decided to use these systems despite of the additional power loss. Stability and compactness allows us to place the six-way distribution systems on a higher platform (above the optical setup for the Zeeman slower) of the optical table. This saves space for more critical optical elements.

We use a $1 \rightarrow 6$ fibre port cluster for 461 nm and for 767 nm. For 671 nm we use a customized version, the "Innsbruck configuration", that was developed for us by Schäfter+Kirchhoff GmbH. This version has two input ports, which can be distributed among the six output fibres. While the first input is used for the ^{6}Li light at 671 nm, the second input port can be used for a different frequency. This includes the intercombination line of Sr at 689 nm to create a MOT using this triplet transition. Another possible application for the second port would be using it for the ^{7}Li isotope. The integrated photodiodes send the signal to a PID, which stabilizes the total power of the MOT beams by regulating the rf-power of the corresponding single-pass AOM in the laser setup. This is necessary to reach a good shot to shot stability.

The six MOT mixing boxes were designed and build in house. The fibre outcouplers from the fibre port clusters are attached to the solid aluminium box by a flange system. They directly deliver collimated beams with the diameters required for the MOT. The beam diameters are 15 mm, 25 mm and 21 mm for 461 nm, 671 nm and 767 nm. We chose a smaller diameter for the Sr MOT because our laser source is not powerful enough to reach saturation intensity. For

[48] www.sukhamburg.de

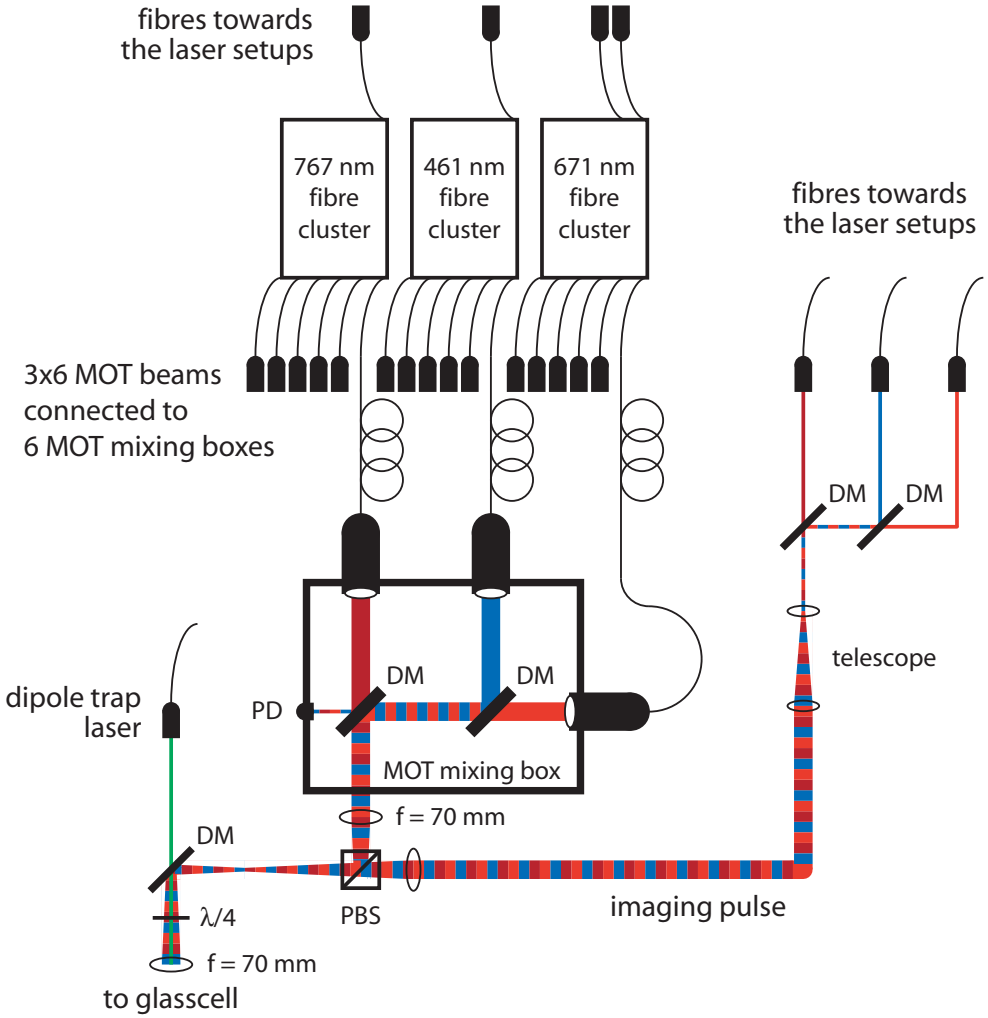

Figure 3.23: Concept of the combination of the beams for the MOT, the imaging and the dipole trap. The 3x6 MOT beams are provided by three fibre cluster systems. The three wavelengths are overlapped using six mixing boxes (only one shown in the figure) with dichroic mirrors (DM). The MOT beams and the beams for imaging are overlapped using a polarizing beamsplitter (PBS). The beam for the dipole trap is inserted using another dichroic mirror. Lenses control the collimation or focusing of the beams and an achromatic quarter-wave plate creates the circular polarization necessary for the MOT. The figure only shows the concept of the system with its most important optical elements. More details are found in the text and the following figures.

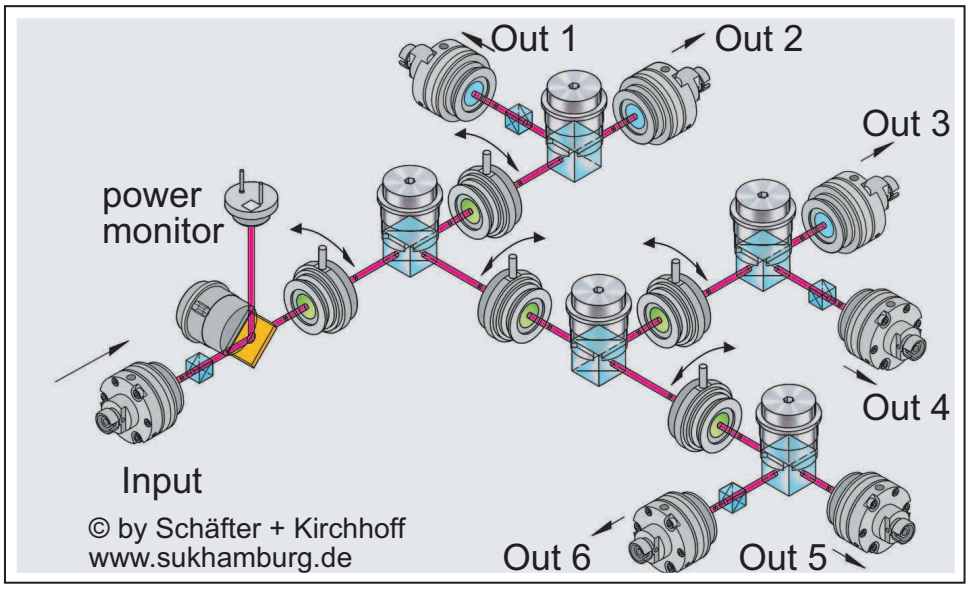

Figure 3.24: Drawing of the Schäfter+Kirchhoff fibre cluster system. The input beam is split into six output beams. Shown are the fibre connectors, the rotatable half-wave plates and the polarizing beamsplitters. The figure is used with permission by Schäfter+Kirchhoff .

the Li and K MOT we chose relatively large diameters, to get a smaller intensity variation inside the central part of the Gaussian beam profile. The two 2" dichroic mirrors overlap the three beams. The mirrors are fixed to the MOT mixing box. Therefore, there is no adjustable element to overlap the beams. The design of the box accounts for the chromatic dependent shifts of the different wavelengths that pass the mirror substrates. Only small corrections are necessary by putting thin metal slices inside the flange during the initial installation. After a good overlap is achieved, no more alignment is needed during the operation. A small part of the 671 nm and the 461 nm (767 nm) part is transmitted (reflected) by the second dichroic mirror. The light is measured using a photodiode on each of the six boxes. These six photodiode readouts allow an easy and reproducible alignment of the six MOT beams by tuning the half-wave plates of the fibre cluster systems.

The MOT mixing boxes are positioned around the vacuum chamber but not in the vicinity of the glass cell where space is very limited. Therfore, the six MOT beams have to be passed towards the optics near the glass cell. We use periscopes within these beam pathes to reach the required polarization if necessary. The glass cell is surrounded by a nonmagnetic steel breadboard in the horizontal plane. All the optics in the vicinity of the glass cell have to be positioned on this board (see Fig. 3.21d for a photo). To save valuable space for future extensions, we designed a very compact mount for the final optical elements of the MOT, imaging and dipole trap beams. It contains the polarizing beamsplitter, the dichroic mirror, the wave plate and the final lens, which were already presented above in Fig. 3.23. A more detailed drawing is depicted in

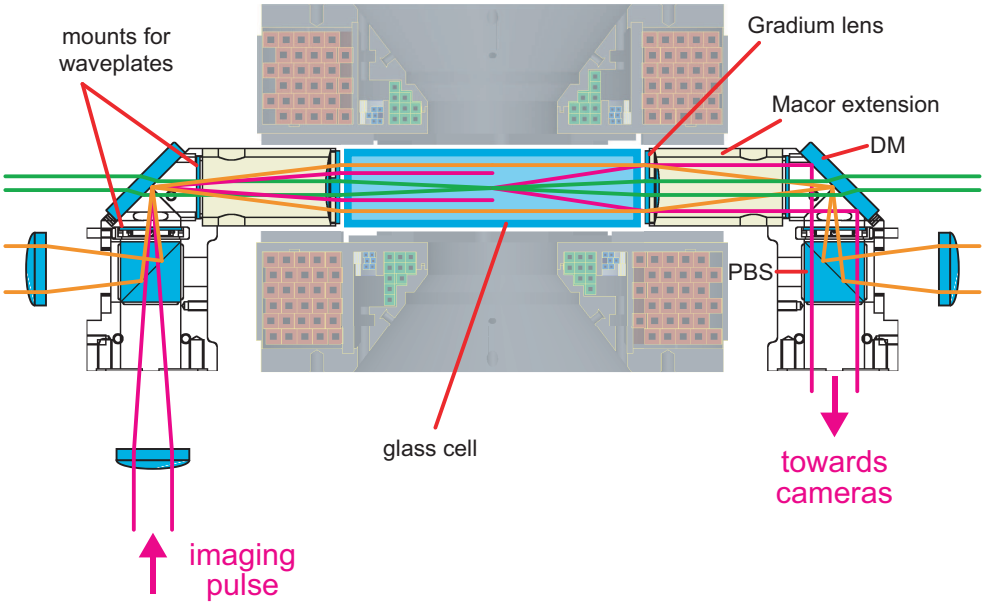

Figure 3.25: Mounting construction for the optics near the glass cell. The figure shows the CAD drawings of the two opposing optic mounts for the Gradium lens, the dichroic mirrors (DM), the polarizing beamsplitters (PBS) and the wave plates. The beam pathes of the MOT beams (yellow), the dipole trap (green) and the imaging beams (pink) are drawn. The imaging pulse crosses the glass cell being collimated. But the scattered photos for the image formation continue the imaging path in the conjugate way as depicted in the figure.

Fig. 3.25. The mount consists of two parts. A tower made of nonmagnetic steel and an extension arm made of the glass ceramic Macor. The polarizing beamsplitter is glued inside the steel tower. The achromatic quarter-wave plate[49] is mounted into a small steel ring, which is placed inside a steel drawer. The drawer can be put in and out of the mounted tower. This allows to exchange the wave plate without causing a misalignment of the other optical elements. The ring mount inside the drawer allows to rotate the wave plate even if it is mounted inside the tower. The dichroic mirror is placed on top of the steel tower and fixed with a few drops of epoxy glue. The coating of the dichroic mirror is reflective for the wavelengths 461 nm, 671 nm, 689 nm and 767 nm and transparent for 532 nm and 1064 nm. A second possibility for mounting a wave plate is after the dichroic mirror in the vertical direction directly in front of the Marcor arm. The extension arm positions the final lens close to the glass cell in between the coil boxes. Marcor is a non conductive glass ceramic material and no eddy currents can be induced inside the extension arm.

Combining so many different laser beams with only few optical elements in tight space requires some compromises. As can be seen in Fig. 3.25, the MOT beam is not collimated when it passes the beam splitter, the wave plate and the dichroic mirror. This requires these optical ele-

[49] custom made by www.novaphase.com

ments to work within a range of the angle of incidence between 45°±7° for reflection and 0°±7° for transmission. The beamsplitter works well within this range and small inhomogeneities of the beam profile do not affect the MOT performance a lot. The angle of incidence of the wave plate is also not critical for the polarization properties. But the dichroic mirror is a more complex element. The reflectance and transmission properties are designed to work within the necessary range of angles. But a precise design of the phase shift properties for s- and p-polarization was not possible for such a complex coating. As a consequence, the mirror works well for linear polarized light in s- and p-direction. But for any other polarization, the different components in the s- and p-direction get a different phase shift during reflection. Additionally, the phase shift depends significantly on the angle of incidence. This is especially important if the incident beam is circular polarized due to the achromatic quarter-wave plate. After testing the optical system for 671 nm and 767 nm, we found, that the phase shift is close enough to zero for 671 nm but about 180° for 767 nm at an angle of incidence close to 45°. Although MOTs are not very sensitive to moderate polarization deviations, no setting of the wave plate could be found to achieve sufficient circular polarization for both wavelengths simultaneously. As a consequence we have to place the wave plate in the second position after the dichroic mirror. In this case, the mirror only reflects light with a linear polarization very close to the s- or p-directions. This does not change the polarization properties significantly. The disadvantages of this solution are the following. First, the antireflection coating of the wave plate does not cover the 1064 nm of the dipole trap beam. The loss of power is not critical. But interference effects due to multiple reflections on the wave plate surfaces could critically affect the performance of the dipole trap. A second disadvantage is that the wave plate can only be exchanged by removing the glued dichroic mirror. This is possible without unmounting the tower. As the dipole traps have not yet been characterized in this configuration, we cannot say, how problematic the reflectance of the wave plate will be. A possible solution would be a different coating for the wave plate, or even the dichroic mirror, or a custom made wave plate in the first position, which allows to reach sufficient polarization properties for Li and K together. Of course, this problem only affects the input side of the dipole trap beam. The MOTs do still work sufficiently even if one or two of the beams have very bad polarization. Therefore, the five MOT beams with a good circular polarization can compensate the sixth beam if the wave plate would have to be positioned in front of the polarizing beamsplitter.

3.9 Diagnostic Tools

Several methods exist to collect information about a cloud of cold atoms. We use different types of imaging systems to take pictures of the clouds. These systems are described in the following sections.

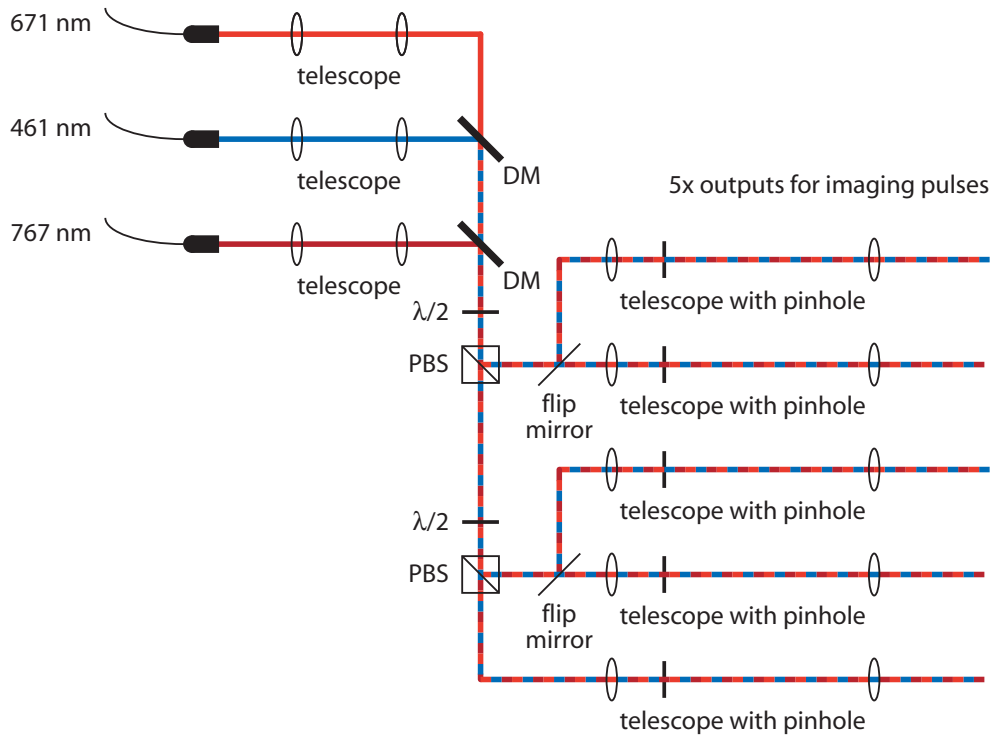

Figure 3.26: Optical concept for the combination of the imaging pulses. The three wavelengths are combined using dichroic mirrors (DM). The multicoloured beam can be distributed to five different outputs using half-wave plates with polarizing beamsplitters (PBS) and flip mirrors. Different telescopes are used to provide multiple beam sizes.

3.9.1 Absorption Imaging

Absorption imaging is one of the most powerful tools to image clouds of cold atoms. The cloud is illuminated with a short puls and the shadow is recorded with a camera. This measures the optical column density of the cloud and many other properties like the atom number, temperature and the density profile for individual spin states can be derived. Our absorption imaging system consists of two parts. The first part generates the pulse for the different wavelengths and sends it onto the atom cloud. The second part collects the pulse and the scattered light of the cloud and images it onto a camera. The concept of the optical setup to combine the different wavelengths for the imaging pulses for Li, K and Sr is shown in Fig. 3.26. The light for the pulses comes from the laser systems described in section 3.5 and is sent to the vacuum chamber table using optical fibres. After the fibres, each beam is enlarged using individual telescopes. This allows us to change the size and collimation of the different imaging beams without affecting the others. But we cannot upscale the probe beams to their final size because it is larger than the aperture of the following mixing and distribution optics. The three wavelengths are overlapped using two dichroic mirrors. Subsequently, the beam can be split into up to three different parts using achro-

matic half-wave plates and polarizing beamsplitters. Splitting up the probe beam allows us to take simultaneous pictures from three different directions. The following achromatic telescopes enlarge the beams to their final diameters. To get an even illumination of the imaging plane, the size of the beams has to be much larger than the size of the image. The following apertures allows us to use beams with a diameter of up to 22 mm. A pinhole inside the focus of the telescope is used as a Fourier filter to obtain a clean Gaussian beam profile. Two of the three imaging beams can be directed in two different directions using flip mirrors. Although only three pulses can be used simultaneously, the other two pathes can offer alternative beam sizes or different imaging directions. The flip mirrors allow to change between different configurations without involving time consuming alignment of the pinhole and the telescopes. The five outputs for the imaging pulses are directed towards the glass cell.

We can take simultaneous absorption images in three orthogonal direction but in most cases, two imaging directions are sufficient. Figure 3.27 shows the concept of the imaging setup around the glass cell for the horizontal directions. The imaging pulse is sent into the glass cell via the multiplexing system described in section 3.8. The first lens for imaging is a $f = 70$ mm Gradium lens[50]. The lens is made of glass with a spatially varying index of refraction. This allows to design a lens with a large aperture, a high damage threshold and low spherical and chromatic aberrations. A first image of the atoms is created with a second lens, a $f = 140$ mm achromat. In between these two lenses we find the elements required for overlapping the imaging beam with the MOT beam and the dipole trap beam. The first image is already magnified by a factor of two. But it is located too close to the glass cell for positioning the cameras. Therefore, we use a second 1:1 imaging system using two more $f = 140$ mm achromats to transport the image 560 mm further away. After these lenses, a dichroic mirror separates the light of two wavelengths. This splits the image into two images of the different elements in the atomic cloud. These two images are now projected onto two separate CCD cameras using exchangeable microscope objectives. Fast electronic iris shutters are installed to block the CCD chips from light before the imaging pulse is sent. A 850 nm short-pass filter is used to block light from the dipole traps. A narrowband line filter blocks any other light not intended for the CCD sensor, especially the resonant light for the other species. A knife edge allows us to cover a part of the CCD chip from being exposed to light. This reduces the effective size of the picture in one dimension. But it allows to quickly shift the image from the exposed chip area into the covered area and take a second image. This process can be repeated depending on the size of the covered area of the CCD chip.

The imaging system is set up in one horizontal and the vertical direction. It can be easily adapted for different elements by exchanging the dichroic mirror and the line filters. The magnification can be selected by exchanging the microscope objectives. The cameras can be exchanged between the different imaging directions. It is also possible to use a single camera for two or three species by using a normal mirror instead of a dichroic one. However, this induces focal shifts between the different wavelengths if images of different elements are taken.

[50] model GPX-30-70 purchased from www.lightpath.com with a custom ultrawideband antireflection coating for 460-1080 nm

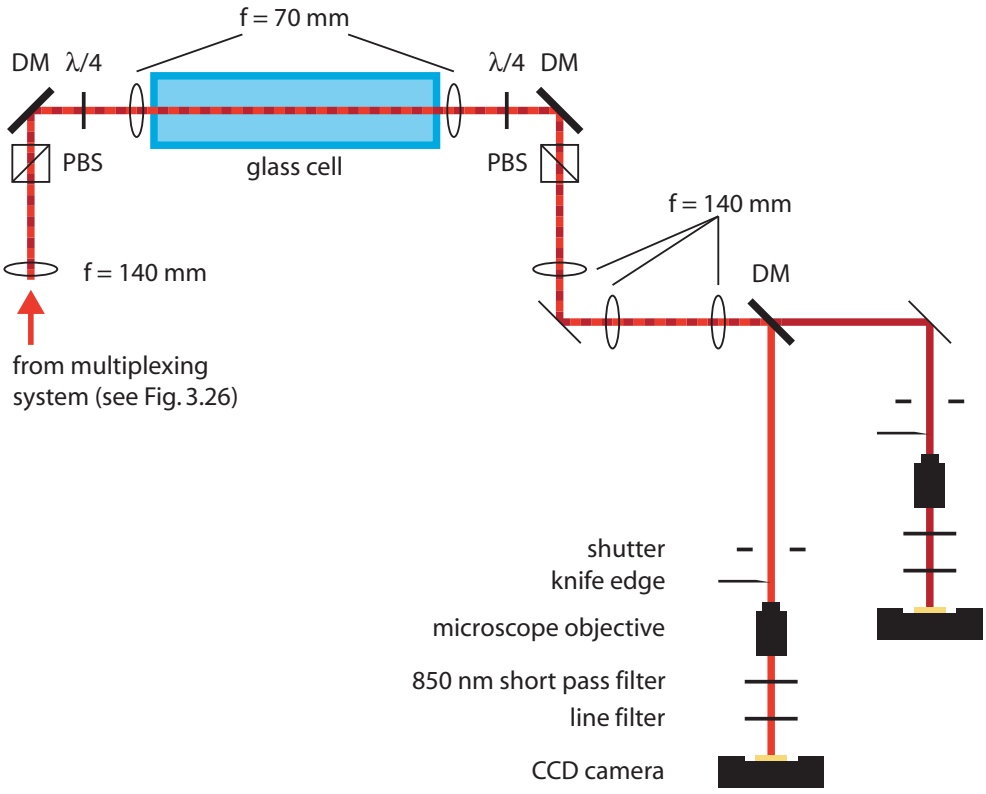

Figure 3.27: Concept of the horizontal absorption imaging system. The imaging pulse enters the glass cell from the left side. A first image is created using a 2x telescope with a $f = 70$ mm Gradium lens and a $f = 140$ mm achromat. This image is transported over a distance of 560 mm using two $f = 140$ mm achromats. A dichroic mirror (DM) splits the image into two images for each colour (shown is the case for 671 nm and 767 nm). These two images are recorded with two CCD cameras using microscope objectives.

We have four scientific cameras of the model A-DV437-BV from Andor[51] for the absorption imaging system and the fluorescence imaging. The cameras have a back illuminated CCD chip with 1024x512 pixels of 13x13 μm^2 size. One half of the chip is covered with an aluminium coating and is used as storage and readout area. We can extend the covered area using the knife edge in the image plane. Using the fast kinetic mode of the camera, we can shift images into the covered area faster than 1 ms. This allows to take several subsequent images within few milliseconds. We use the fast kinetic mode to take several pictures of different spin states of the atoms or to image several species on a single camera.

In an absorption picture, the atomic cloud appears as a shadow. To obtain the optical density of the cloud, the fraction of absorbed photons has to be calculated. Therefore, a second

[51] www.andor.com

picture of the pulse without the cloud is required. The fast kinetic mode allows us to take this reference picture only a few milliseconds after the first picture. This reduces the image noise significantly as mechanical vibrations and other external perturbations do not change a lot during a millisecond. Another degradation of the image can happen due to residual background light, or crosstalk between the different imaging pulses and the exposure areas. These kind of effects can be cancelled by taking dark frames of the same series of images but without the imaging pulse. Any signal on these images is subtracted from the former two images with imaging pulses. The final optical density of the atomic cloud is calculated by

$$OD = \log \frac{I_{\text{without atoms}} - I_{\text{dark frame 1}}}{I_{\text{with atoms}} - I_{\text{dark frame 2}}}$$

for each pixel. I is the light intensity recorded by the camera.

3.9.2 Fluorescence Imaging

Another method to image the atoms is to use their fluorescence signal. For this, the atoms are trapped in a MOT. For low atom numbers, the fluorescence signal is proportional to the atom number. This method is very sensitive even for atom numbers below 1000 where absorption images are difficult to take. Atoms trapped in a dipole trap can be recaptured by a MOT to record their fluorescence signal. In that case, the fluorescence images do not give information about many parameters like the density distribution or the temperature of the atoms inside the dipole trap. As this method does not involve the imaging laser beams, it is easier to achieve a good shot to shot stability of the experiment. We use a setup as shown in Fig. 3.28 to record the fluorescence. A $f = 200$ mm lens collects the light from the MOT and collimates it. A dichroic mirror splits it up and two $f = 150$ mm lenses focus it onto two CCD cameras. A combination of filters protects the CCD chips from light not coming from the MOT. To subtract the background light, not only a fluorescence image is taken, but also a reference image without atoms.

3.9.3 Auxiliary Imaging Systems

We installed several auxiliary imaging systems to increase the stability of the experiment and to make the alignment and operation more user-friendly.

A good shot to shot stability depends on the initial number of atoms that are loaded into the MOT. Especially the flux of the oven can vary on the timescale of some minutes. Therefore, we use the fluorescence of the MOT to trigger the end of the loading phase. The system is similar to the scientific fluorescence system as shown in Fig. 3.28. The fluorescence is collected by a 200 mm lens close to the glass cell. Here we use two dichroic mirrors that separate the 461 nm, the 671 nm and the 767 nm light. Using three 25 mm lenses, each of the beams is focused onto a large area photodiode[52]. A number of filters suppress ambient light and crosstalk between the

[52] model S8746-01 from www.hamamatsu.de

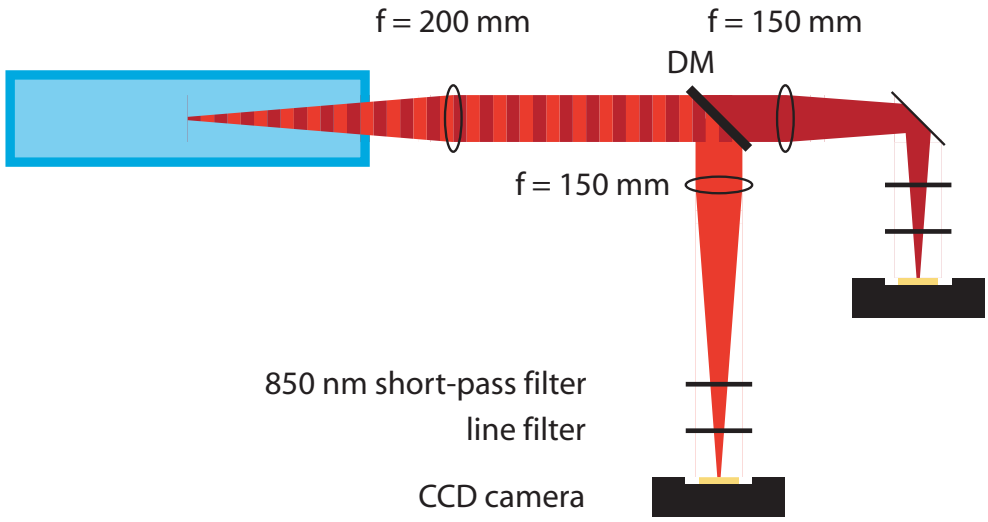

Figure 3.28: Optical concept of the fluorescence imaging system. A $f = 200$ mm lens collects the fluorescence from the MOT and collimates it. The signal is split into two colours (shown is the case with 671 nm and 767 nm) using a dichroic mirror and recorded on two different CCD cameras.

three beams. All the 25 mm lenses, mirrors, filters and photodiodes are installed inside a compact aluminium box. That allows an easy installment of this multi-colour fluorescence measurement device. The voltage of the photodiodes is measured and triggers the end of the MOT loading as soon as a threshold is reached.

The same box design is used to record images of the MOT. Instead of the photodiodes, three 1/3" CCD cameras are installed. Two of these boxes allow to monitor the different MOTs of Li, K and Sr from different directions. The image is displayed on surveillance monitors. This helps aligning the MOTs and to supervise the smooth operation of the experiment.

The alignment of the dipole traps (see the following section) can be supervised using several 1/3" CCD finger cameras. The residual transmission of the dipole trap laser beams through a mirror is used to image the focus of the dipole trap. The image is shown on a monitor and allows to control the alignment and the correct operation of the trap.

3.10 Dipole Traps

After capturing the atoms in a multi-species MOT they are transferred into an optical dipole trap for evaporation towards lower temperatures. Our experiment is designed to offer the possibility of using three different kinds of dipole traps. They are presented in the following sections.

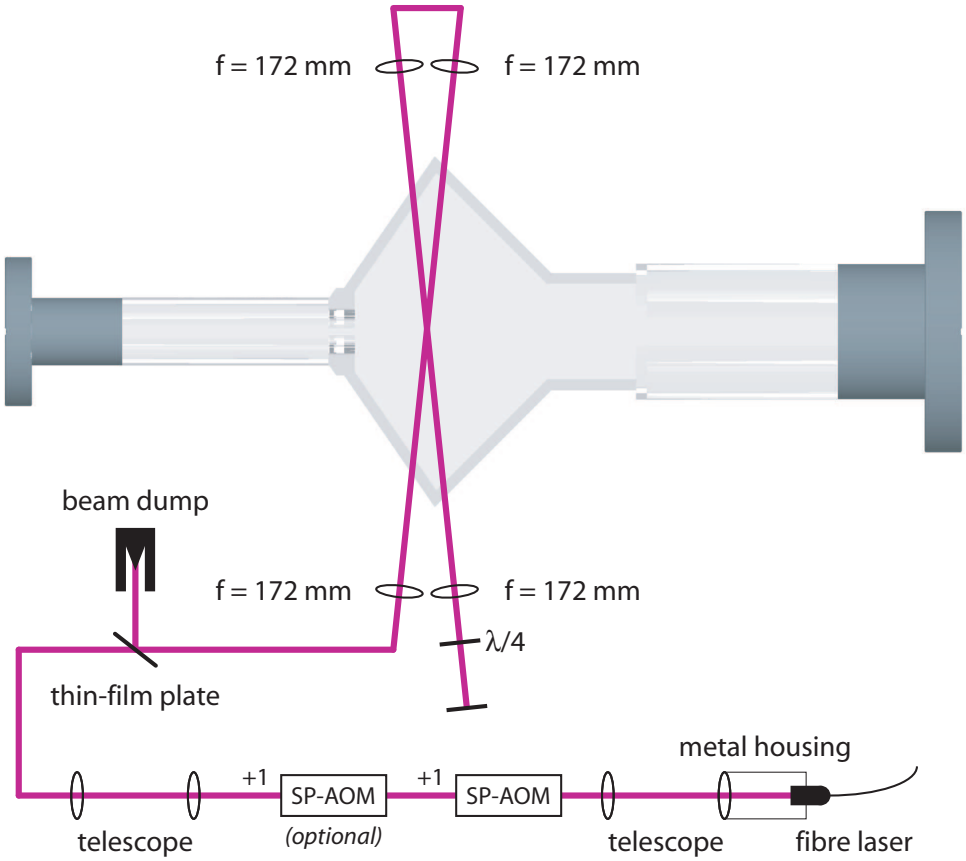

Figure 3.29: Optical concept of the high-power dipole trap. A 1070 nm fibre laser provides a beam of 100 W. The intensity is controlled using AOMs. The beam is focused into the glass cell during up to four passages. The back reflected beam is dumped by turning its polarization and reflecting it with a thin film plate.

3.10.1 High-Power Dipole Trap

The most important trap of our experiment is a high-power optical dipole trap based on a 100-W single-mode ytterbium fibre laser[53] with a wavelength of 1070 nm. The optical setup for this dipole trap is shown in Fig. 3.29. The fibre laser itself is placed in the basement below the lab and its fibre is running up onto the optical table. The output coupler of the fibre laser is fixed inside a closed aluminium housing to protect the collimation lens from dust. The output of this housing is the first lens of a telescope to decrease the beam diameter from 6 mm to 0.7 mm. The small beam passes one or two single-pass AOMs to control the intensity. Using two AOMs decreases the optical power for the dipole trap but it allows to reach a lower attenuation. If the power is more important, we use only one AOM, but in this case, the dipole trap cannot be switched off completely without using a mechanical shutter. The zero orders of the AOMs are

[53] model YLR-100-SM-LP purchased from www.ipgphotonics.com

dumped in water-cooled beam dumps using small pick up mirrors. After passing the AOMs, a second telescope increases the beam diameter to 4.0 mm. The s-polarized beam passes a thin film plate, which is used to dump the p-polarized back reflection into a water-cooled beam dump. The optics described so far are placed inside an aluminium box on the optical table. This minimizes dust on the optical components, it shields from stray light and is a security protection against the high-power beam. The beam leaves the box and is focused into the center of the glass cell using a $f = 172$ mm lens. The beam exits the glass cell and is recollimated using another $f = 172$ mm lens. Afterwards, it is focused a second time crossing the glass cell in the opposite direction. The two beams cross under an angle of $12°$[54]. A retroreflecting mirror now sends the laser back the same way. A double-pass quarter-wave plate turns the polarization into the p-direction. This gives us two more focal points in the center of the glass cell.

This setup can be used in different ways depending on the alignment of the four focal points. If only one or two focal points are desired, the beam can be blocked at a suitable position. This gives us four useful configurations. First, we can make a single-focus dipole trap. Second, we can overlap the first two focal points resulting in a crossed dipole trap. Third, we can overlap all four focal points to get a larger crossed dipole trap. Fourth, we can use the first and the third passage to overlap these two focal points, while the other two focal points cross the glasscell outside the center. These four possibilities have different advantages and disadvantages. The main differences are the total trap depth, the directions in which the two beams cross each other (co- or counterpropating) and the polarization of the crossing beams. This has strong effects on the number and lifetime of the trapped atoms and will be discussed in chapter 4. During the different passages several Fresnel reflections occur at the glass surfaces. This has two consequences. The reflected beams can still have powers of several watts and have to be dumped. It also reduces the power in the different focal points. Relative to the power incident on the glass cell, the power of the four focal points is 97%, 88%, 74% and 56%.

For typical focus diameters of about 60 μm the dipole trap reaches maximal trap depths for Li of few mK. This is sufficient to capture enough atoms from the MOTs to perform efficient evaporative cooling at the Li 834 G Feshbach resonance. But this trap also has significant disadvantages. The most severe restriction is due to thermal lensing of the 100 W beam. Especially in the crossed configurations, the induced focal shift can significantly alter the position and geometry of the dipole trap. The shape of a crossed trap will also deviate from a harmonic potential complicating the interpretation of the results. To overcome these problems, we can use another dipole trap, which is presented in the following section.

3.10.2 Low-Power Dipole Trap

The low-power optical dipole traps are implemented to provide a stable trap with well-known properties for the studies of the quantum gases. After evaporation in the high-power dipole trap, the atoms can be loaded into these subsequent traps. We use a 5-W single-mode ytterbium fibre

[54]The small angle is chosen to achieve a good overlap with the resonator dipole trap, see section 3.10.3.

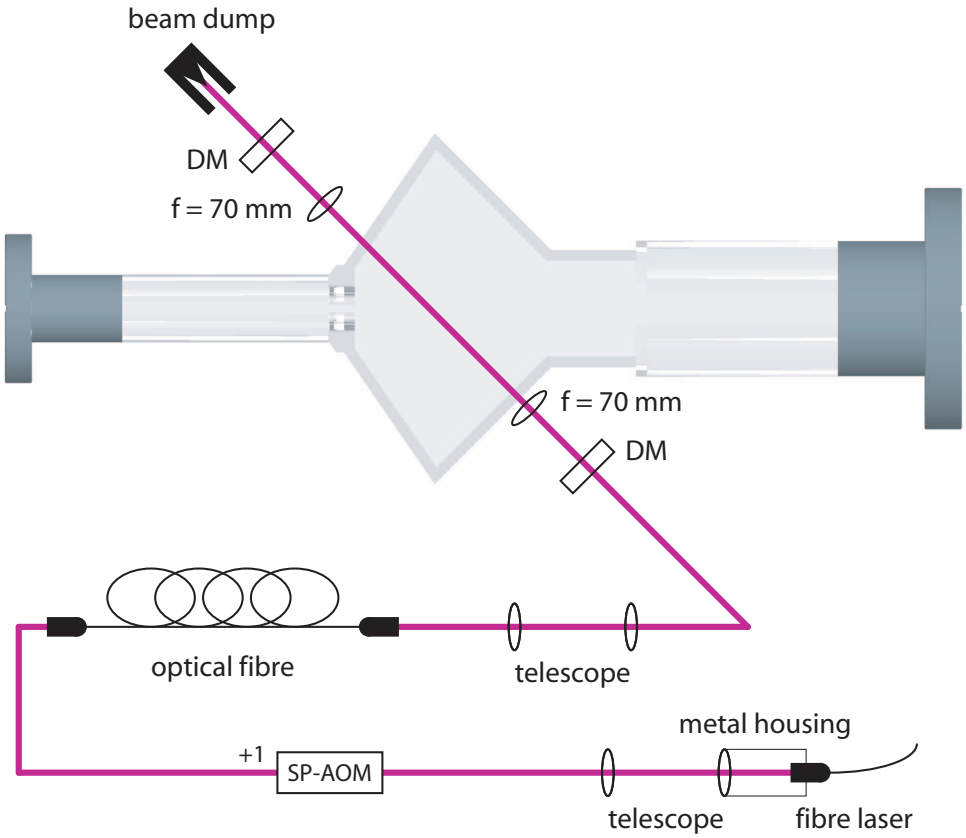

Figure 3.30: Optical concept for the low-power dipole trap. After passing the AOM, the laser beam is spatially filtered using a single-mode fibre. It enters the glass cell via the dichroic mirror (DM) that overlaps it with the MOT and imaging axis. The wall of the glass cell is crossed under 90° reducing aspheric aberrations. The same setup can be realized in the orthogonal direction (not shown).

laser[55] with a wavelength of 1064 nm. The optical setup is shown in Fig. 3.30. As for the 100-W laser, the 5-W laser is placed in the basement below the lab and its fibre is running up onto the optical table and the outcoupler is put inside a closed metal box. A first telescope scales down the beam diameter to be able to pass a single-pass AOM for intensity regulation. Afterwards, the light is coupled into a single-mode fibre to gain a clean Gaussian profile. A second telescope enlarges the beam and sends it through the dichroic mirror to overlap it with the axis of the MOT and the imaging system. The Gradium 70 mm lens produces the focus of the dipole trap. Depending on the diameter of the collimated laser beam, focus diameters below 20 μm can be achieved. The laser beam crosses the wall of the glass cell orthogonally to minimize aspheric aberrations. Additionally, all three main axis of this dipole trap are also orthogonal to the imaging directions. This simplifies the analysis of the pictures, especially for measuring the profile or oscillations of

[55] model YLD-5-LP purchased from www.ipgphotonics.com

the cloud. The experiment offers the space to install a second low-power optical dipole trap by using the same setup on the second horizontal axis.

3.10.3 Resonator Trap

The depth and size of an optical dipole trap are limited by the available laser power. One possibility of increasing the power of a dipole trap is using a Fabry Perot type resonator [92]. Andreas Trenkwalder designed an optical dipole trap of this kind for our experiment during his diploma thesis [73]. The trap is based on a frequency stabilized 25 W Yb:YAG thin disk laser[56]. The laser is stabilized on an external cavity to obtain a linewidth of less than 100 kHz. The Fabry Perot resonator is built around the glass cell and enhances the power by three orders of magnitude. The concept of the optical setup is shown in Fig. 3.31 and a detailed report is published in form of the diploma thesis [73].

The resonator dipole trap can reach trap depths of several millikelvin with the waist of the trap being about 300 μm. This trap should be able to capture a significantly larger number of atoms from the MOT than the single-focus dipole trap. A partial evaporation in the resonator trap is possible. But the atoms are distributed over many (≈ 1000) separate pancake-shaped dipole traps made of the antinodes of the standing wave. They have to be transferred into a single-focus dipole trap as for example the high-power dipole trap. This latter trap has to cross as many of the antinodes as possible. This is realized by the small crossing angle of 6° between the high-power dipole trap and the resonator axis.

The design of the resonator trap is finished and ready for installation. However, as the high-power dipole trap alone already loads enough atoms from the MOT for performing experiments in the ultracold regime, we did not yet use the resonator trap. But it is a powerful option to increase the atom numbers for more demanding experiments on our machine.

3.11 Control System

Controlling an experiment performed with the FeLiKx machine requires powerful soft- and hardware. During the sequence of an experimental run, which takes about 30 s, a large number of different devices has to be operated with a timing accuracy of less than 10 μs. Our control system is based on a concept by Florian Schreck and Todd Meyrath and further developments by Gerhard Hendl. The scheme of the control network is shown in Fig. 3.32.

The central part of the control system is the *Control PC* with a NI6533 card. This computer is used to program the sequence of actions for a specific experiment using the software Control[57]. Nearly all commands are sent from the NI6533 card over a home build bus system to operate the

[56] VersaDisk purchased from www.els.de

[57] programmed by Florian Schreck, available at www.nintaka.com/Control

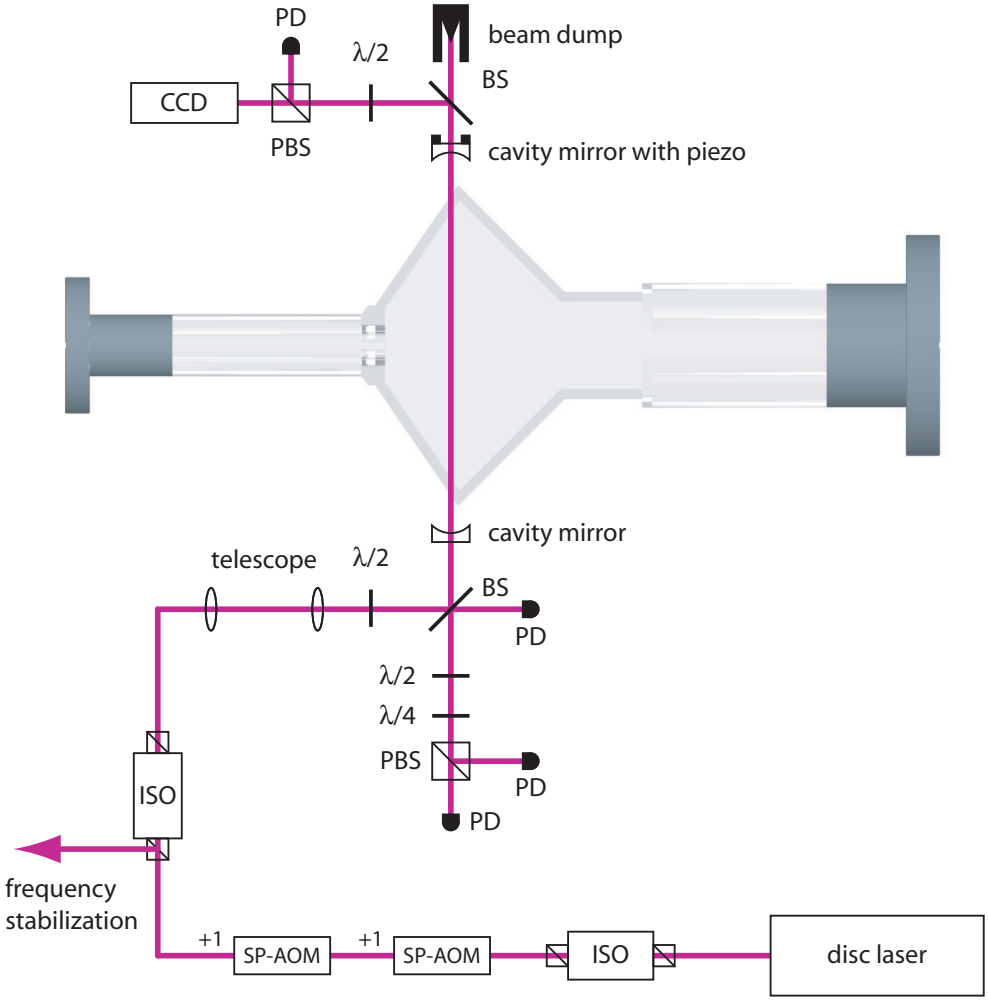

Figure 3.31: Optical concept of the resonator dipole trap. This dipole trap is placed orthogonal to the glass cell axis. The resonator beam crosses the glass cell under Brewsters angle. More information can be found in Ref. [73].

electrical, optical and mechanical parts of the experiment. This bus operates with a clock cycle of 2 MHz and has a data bandwidth of 16 bit. It can address up to 256 devices (i.e. having 8 address bits). To increase the number of addresses, we use five sub-buses giving us 1280 available addresses. Bidirectional communication with few other devices is done using a GPIB bus or the serial port, if the operation is not time critical. The parallel port is used for reading analog signals. Additionally, the *Control PC* is connected to six other computers via a gigabit ethernet. The *Vision PC* is running the software Vision[58] to display the pictures taken with the CCD cameras and to perform and display scientific analysis of these pictures. It also saves the pictures and protocols of the sequence on its hard disc. The *Camera Master PC* is mainly used

[58]programmed by Florian Schreck, available at www.nintaka.com/Control

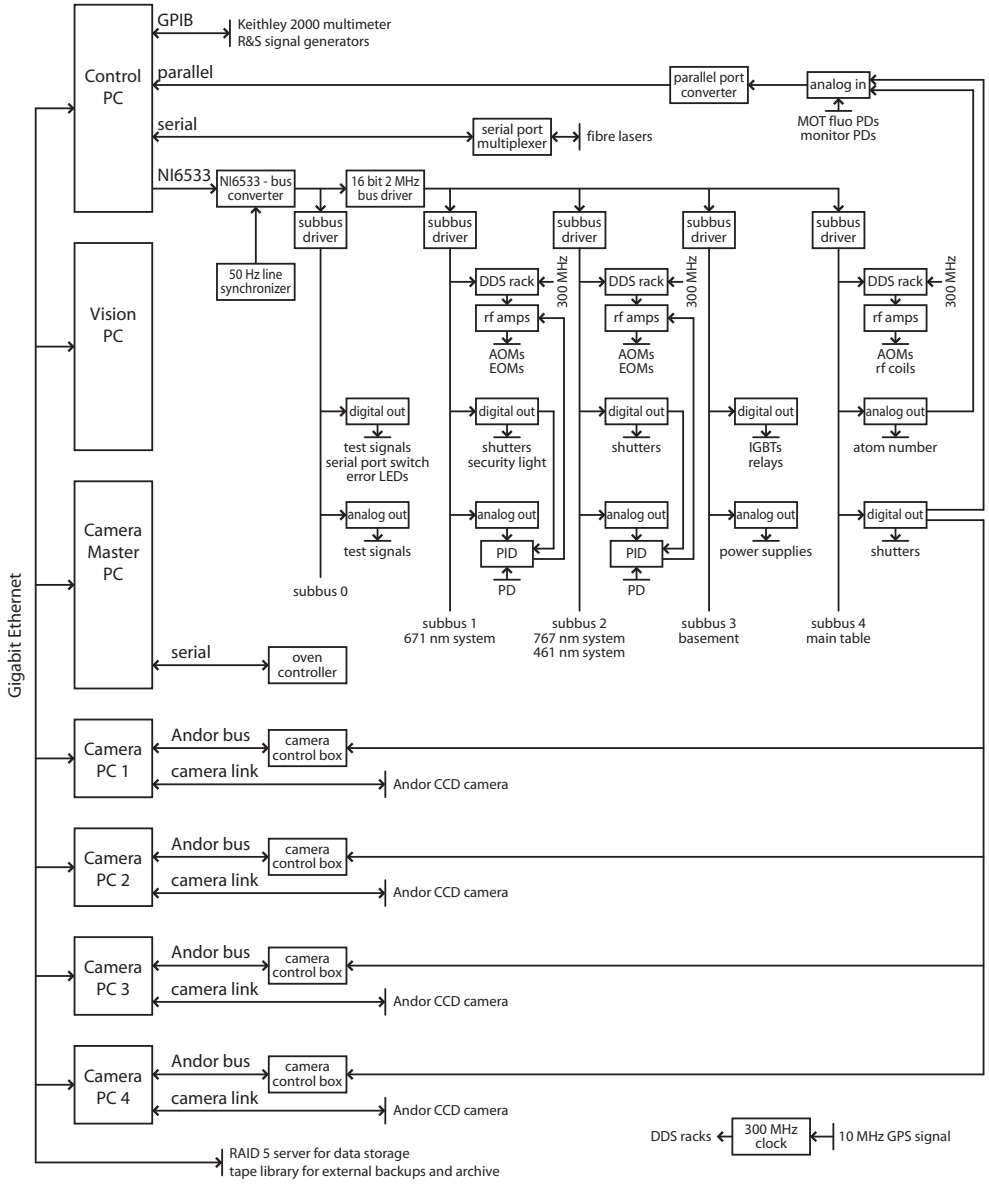

Figure 3.32: Concept of the electronic control network. The diagram shows the seven computers that control the electronic hardware of the experiment using different in- and outputs.

to control the four *Camera PCs* using remote desktops. Beside of that, it runs the oven control software to programme the PIDs of the oven controller via the serial port. Each of the four *Camera PCs* communicates with one of the CCD cameras using a dedicated controller card[59]. The *Camera PCs* are used to programm the settings of the cameras and to read out the images and transfer them to the *Vision PC*. Triggering the cameras is timing critical and therefore done over the bus system using the trigger input of the controller cards. An ethernet connection towards the RAID5 server of the IQOQI allows to save the data on a secure hard disc. As the experiment can produce more than 500 GB of data per month, old data is compressed and stored on the tape drive library of the University of Innsbruck.

After the user has set all parameters for the experiment in the Control software, the *Control PC* calculates the bit stream with the commands for all the devices. This data is written to the NI6533 card, which sends it to the bus. The start of each sequence is triggered by the 50 Hz line synchronizer to improve the shot to shot stability. The bus signal is amplified by a bus driver box distributed to the different sub-buses for each optical table and the basement. The sub-bus drivers select the data for each sub-bus and again amplify the signals. The bus controls three different types of outputs: the DDS frequency generators, the digital outputs and the analog outputs.

The DDS[60] can be programmed to generate frequencies from DC to 135 MHz with an amplitude between 0 and 63 mV (-11 dBm). Higher frequencies can be obtained using frequency doublers. We use the DDSs to drive the AOMs, EOMs and for the radio frequency pulses for the rf-coils. The output signal from the DDS is amplified using home build 2 W amplifiers[61]. The DDS use a 300 MHz clock signal provided by a signal generator[62], which itself is connected to the 10 MHz GPS signal line of the IQOQI.

The digital outputs of the bus generate TTL signals suitable to drive 50 Ω loads. They are used to switch the IGBTs, the relays of the coils and the shutters. They trigger the CCD cameras and operate the sample hold function of the PIDs. The digital outputs are also used to select the channels of the analog inputs (see below) and the channels of the serial port multiplexer. Additionally, they drive several LEDs to display error messages and they control the laser security warning sign of the laboratory.

The analog outputs of the bus system are used to control the current of the power supplies for the coils and for the PID settings that control the laser power for the MOTs. The analog outputs can drive up to 250 mA from -10 to +10 V. The PIDs for the MOT intensity compare the signal of the analog output with the photodiode signal of the fibre cluster and regulate the attenuation of the 2 W amplifier that feeds the double-pass AOM for the MOT laser beam. The analog outputs are also used as reference signal for the analog inputs (see below). Another useful option of the analog outputs is to provide a voltage proportional to a result from the Vision software as for example the atom number derived from an absorption image. This signal can be

[59] model A-CCI010 PCI card

[60] design by Todd Meyrath, see www.ph.utexas.edu/ meyrath/

[61] designed by Florian Schreck, available at www.nintaka.com/Control

[62] model SMB-B101 from www.rohde-schwarz.com

used to optimize an alignment for high atom numbers without having eye contact with the screen of the *Vision PC*.

Although the bus can also be operated bidirectional, we use it only to write signals. For reading signals from the experiment, we use an analog input box working as follows. Up to eight different analog input signals can be connected to one box. A 3 bit digital input selects one of the eight channels. The voltage of this channel is now compared to a reference voltage. The reference voltage is supplied by an analog output of the bus. The analog input box sends the result of the comparison to the parallel port of the *Control PC* via a 1 bit digital signal. By varying the reference voltage using the bisection method, the input voltage can be determined. We use the digital input to measure the fluorescence of the MOTs, and to monitor the intensity of several laser beams.

The serial port of the *Control PC* is used to switch the fibre lasers on or off as they are placed in the basement. The computer control allows to combine the switching procedure directly with an acoustic warning signal and the illumination of the laser security sign.

The GPIB bus is used to communicate with the signal generators used for the beat locks of the diode lasers. This allows to sweep the reference frequency to shift the laser frequency over a range not accessible using AOMs. A precision multimeter[63] is used with the GPIB bus to record additional data once in a while like air or water temperatures.

For supervision and debugging of the experiment, we have connected copies of many electrical signals to a 64x BNC patch panel close to the control desk. This facilitates the flexible display of important signals on digital oscilloscopes. Additionally, several small CCD cameras monitor the MOTs, the atomic beam, the positions of the laser beams for the dipole traps and the displays of several instruments. The images are displayed on a number of surveillance monitors located over the control desk. This enables an operator to control and overview the whole experiment from a single place.

The electronic devices are located at different places inside the laboratory and in the basement. The large extension increases the importance to avoid ground loops. Therefore, the different parts of the electronic system are separated using optocouplers[64] or transformers.

3.12 Security System

The implementation of a powerful security system for FeLiKx is important for several reasons. First, many of the crucial parts of the experiment can only be replaced with a lot of work or big financial efforts. They have to be protected from technical and human errors. Second, the complexity of the machine makes it difficult for the operator to know all the limits of the different parts. This requires a security system working independently from the operator. Third, it is

[63] model Keithley 2000 from www.keithley.com

[64] design by Todd Meyrath, see www.ph.utexas.edu/ meyrath/

desired to operate the machine autonomously for many hours without the presence of an operator. This requires to detect malfunctions and to initialize a controlled switch off to prevent further damage.

We have four different categories of devices, which can be the origin of dangerous problems: power supplies, cooling water, high-power lasers and the vacuum chamber. We implemented an emergency shut down via the interlocks of the power supplies, the pumps for the water, the lasers or to close the gate valves. The interlock lines are shown as thick lines in the concept of our security system in Fig. 3.33. Several sensors on the left of the figure measure the critical parameters and either interrupt the interlocks directly or via a dedicated circuit board. We do not want, that every error switches off the whole machine. Therefore, we need a network to relate the sensor detecting an error to the possible source(s). This network is realized using several circuit boards. Naturally, the logic of all interlocks is implemented in a way that any problem with the security system itself (like power outages or defective cables) trigger the necessary actions.

Leaks can lead to a contamination of the vacuum chamber. Leaks are more likely to occur at the oven or at delicate parts like viewports. We installed gate valves to separate the important UHV part of the chamber from the rest to reduce the damage in case of a leak. The gate valves are closed using pressurized air if the currents of the ion pumps reach a certain threshold.

A second hazard are the high-power infrared lasers. The beams have to be dumped using water-cooled beam dumps. If the cooling fails, the lasers have to be switched off to prevent the plastic tubes of the beam dumps from melting. We use a temperature relay on each beam dump, which is connected to the specific laser interlock. The common water flux through all beam dumps is measured with a fluxmeter. If it falls below a certain limit, all high-power lasers are switched off.

The most complex part of the security system is to protect the magnetic field coils. Different malfunctions like overheating, water leaks, insufficient water flux or water temperatures require different counter measures. Additionally, different power supplies can be connected to different coils depending on the position of the relays. We measure the water flux in the high pressure (HP) circuit and in the two low pressure (LP1 and LP2) circuits. The flux in each circuit is measured using two precision flux meters, one after the pumps and a second in the backflow tube. If the two fluxes are not equal, water is lost through a leak. Additionally, insufficient water flux in each circuit can be detected. The situation is analyzed electronically by a water guard circuit. This circuit can individually operate the interlocks of each power supply and the two pumps. If a leak in one of the circuits occurs, the associated pump and power supplies are shut down. If the flux drops below the limit, only the associated power supplies are shut down while the pumps keep running. The temperatures of the coils are measured using thermistors. They are connected to a temperature guard that controls each channel to be within a programmable range. If any of the temperatures is out of the working range, the power supplies are switched off while the pumps keep running. The precision flux meters only measure the overall flux of the three big circuits and their main purpose is the detection of leaks. Each of the three water

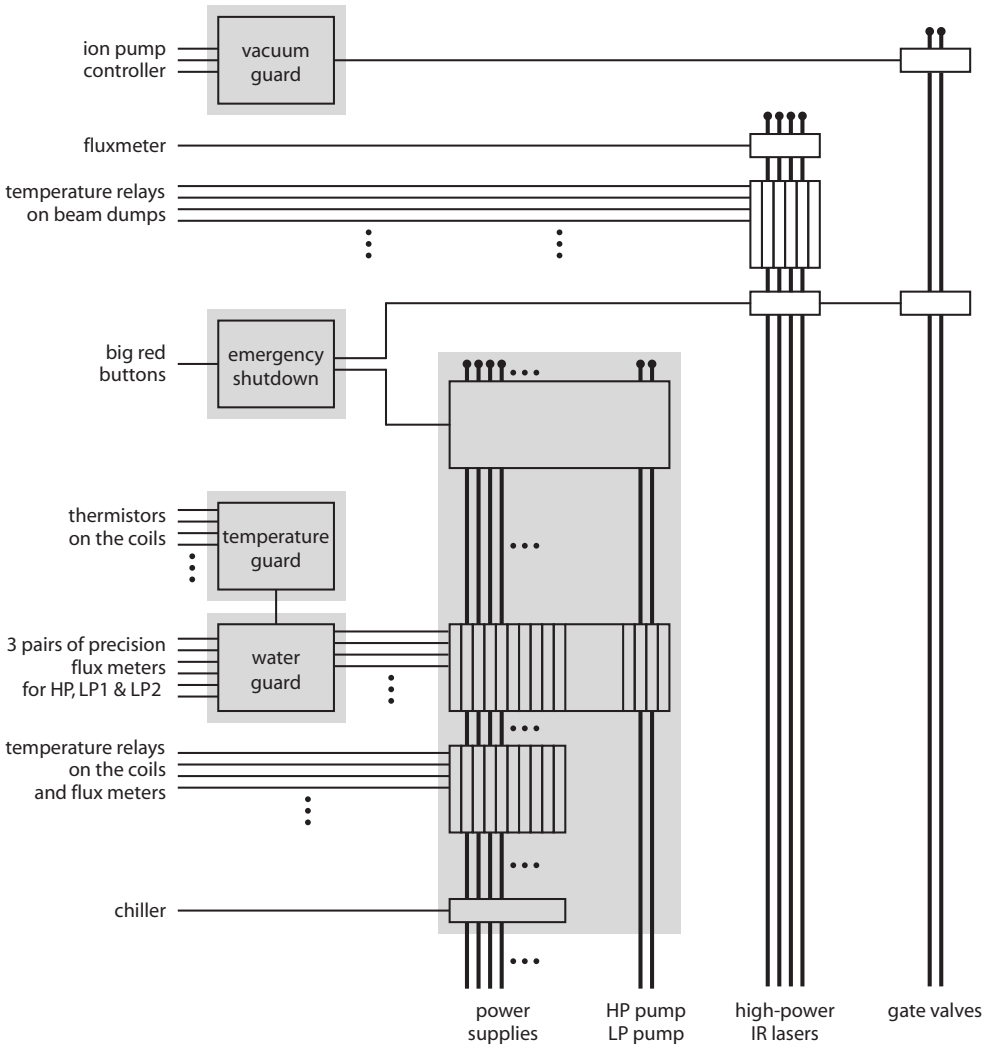

Figure 3.33: Concept of the security system. The thick vertical lines indicate the interlock lines of the different devices. An empty box indicates that the interlocks can be interrupted by the attached controller or detector. Boxes filled with vertical lines indicate that the different interlocks can be addressed individually depending on the input signals. The devices listed on the left-hand side provide the signals to operate the interlocks. Systems within a shaded area are each build on a common circuit board.

circuits contains between 8 and 10 parallel circuits of the different coils (and other devices). To detect plugging of any coil, every parallel circuit has its own flux meter. These flux meters are simple mechanical switches, which stay open as long as the flux is above a preset value. They are connected to the interlocks of the power supply of the associated coils. Additionally to the thermistors, we installed temperature relays on the coils. They are connected together with the flux meters to the interlocks of all the power supplies, which are connected to the specific coil.

Another possible error is a malfunction of the chiller. In this case, the water would not be cooled anymore. Therefore, an error of the chiller will trigger the interlocks of all power supplies but not the pumps.

We also need big red panic buttons for the people working in the lab. Operating a panic button in the case of an emergency assures, that all dangerous parts are immediately switched off. Especially, the operator can push the panic button without being afraid of causing any damage by doing something wrong. Being more specific, all power supplies for the coils, the pumps and all high-power lasers are switched off and the gate valves are closed.

In addition to the interlocks, the power supplies, lasers and the gate valves can be operated by the *Control PC*. They can be switched off during automated operation if the experiment is interrupted due to an unlocked laser or similar problems. This safes energy and increase the lifetime of the devices.

Chapter 4

Experimental Procedures

The setup described in the last chapter has been designed to offer a wide range of possibilities for making and studying Fermi mixtures. This chapter presents a procedure to produce an ultracold mixture of ^{6}Li and ^{40}K. It should be noted, that working with a mixture of these two species just started during the last two years [80, 62, 81]. Therefore, the optimization of the experimental sequence is still an ongoing process and future work will certainly show improved methods.

This chapter is divided into three parts corresponding to the successive steps of the experimental sequence. The first part presents the loading of a multi-species magneto-optical trap. The second part discusses the transfer into a dipole trap. The evaporative cooling is covered in the third section. The technical details of the setup have been covered in the preceding chapter and should not be repeated here. This chapter concentrates on the description of the parameters and the timing of the different steps of the experiment and presents the related results.

4.1 A Multi-Species MOT

The first step of trapping and cooling the atoms is usually done by using a MOT. The FeLiKx experiment is designed to create multi-species MOTs of Li, K and Sr. Different species have different settings for optimal performance of a MOT. Combining two or more species therefore requires compromises to get an optimal overall performance. Earlier examples of double and triple species MOTs for different species can be found in the references [104, 105, 106, 107, 108, 109, 110, 111]. In this section we will first present the individual settings for the ^{6}Li and ^{40}K MOTs. Afterwards, the sequence for creating a combined ^{6}Li-^{40}K MOT is discussed. At the end, we will present the first results with Sr.

One main strategy of the FeLiKx project is to use ^{6}Li atoms and the broad Feshbach resonance between ^{6}Li $|a\rangle$-^{6}Li$|b\rangle$ at 834 G to sympathetically cool ^{40}K during the evaporation. This requires a large number of ^{6}Li atoms while the requirements for ^{40}K are less demanding.

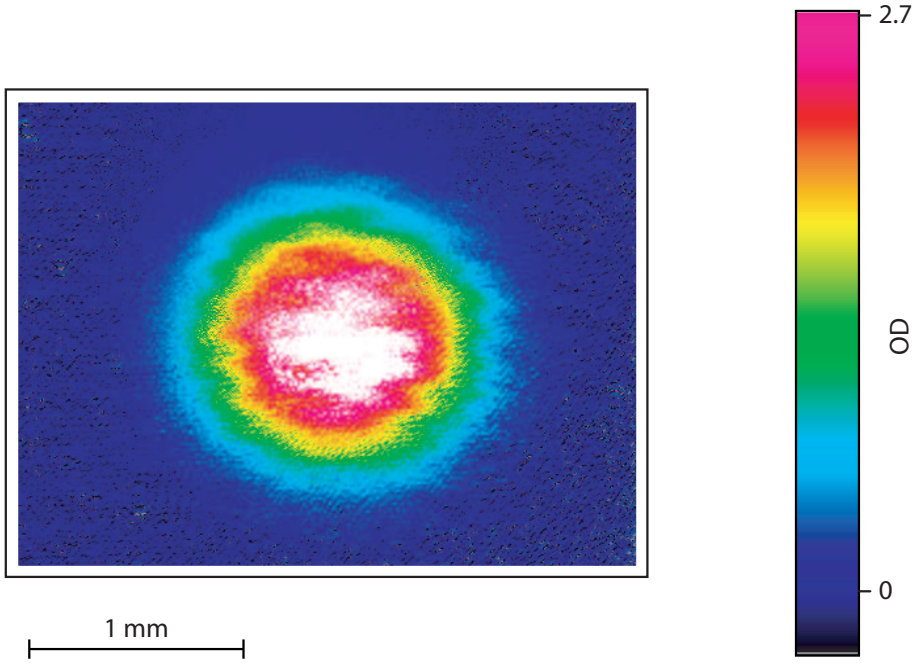

Figure 4.1: False colour absorption image of a ^{6}Li MOT. The MOT contains about 10^9 ^{6}Li atoms. The optical density (OD) is encoded in the colour palette on the right.

All the MOTs are loaded from the atomic beam created from the multi-species oven described in section 3.2. The atoms are slowed down in the Zeeman slower (section 3.6) and trapped by the MOT inside the glass cell. The relevant parameters for the Zeeman slower and the MOTs are shown in table 4.1 and 4.2, respectively. The polarization of the Zeeman slower light is adjusted experimentally by using the wave plates to compensate the birefringence of the sapphire viewport.

These values are determined experimentally by optimizing the loading rate of the single species MOTs. For ^{6}Li, we can achieve a loading rate of more than 10^8 atoms/s and MOTs with several 10^9 atoms. Figure 4.1 shows an absorption picture of the ^{6}Li MOT of about 10^9 atoms. The picture was taken with an early, improvised wide field imaging system not described in the last chapter.

While we can easily load a sufficient number of ^{6}Li atoms, a large ^{40}K MOT is more difficult to achieve. In the laser setup presented in section 3.5.2, the cooling and repumping light are overlapped in front of the first tapered amplifier. The alignment of the injection crucially affects the output. A given power ratio of the injected light does not necessarily result in the same power ratio of the amplified light output. Furthermore, the output beams for the two frequencies may not be perfectly overlapped, which can result in different efficiencies for coupling into a fibre. Consequently, the power ratio before the injection into the tapered amplifier has to be optimized together with the optical alignment of the injection into both, the amplifier and the

Parameter	unit	^{6}Li	^{40}K
Wavelength	nm	671	767
Power	mW	100	150
Cooling/Repump ratio	-	1:1	3:1
Cooling transition (D2-line)	-	$F = 3/2 \rightarrow 5/2$	$F = 9/2 \rightarrow 11/2$
Repumping transition (D2-line)	-	$F = 1/2 \rightarrow 3/2$	$F = 7/2 \rightarrow 9/2$
Linewidth $\Gamma/2\pi$	MHz	5.9	6.0
Detuning of cooling transition	MHz	-494 MHz	-188 MHz
Detuning of repumping transition	MHz	-497 MHz	-192 MHz
Current in first section	A	13	5
Current in second section	A	5	5
Current in third section	A	140	70
Current in compensation coil	A	40	20

Table 4.1: Parameters of the Zeeman slower for loading the ^{6}Li and ^{40}K MOTs.

Parameter	unit	^{6}Li	^{40}K
Wavelength	nm	671	767
Beam diameter	mm	25	21
Power per beam	mW	12	12
Peak intensity	mW/cm^2	4.9	6.9
Saturation intensity	mW/cm^2	2.5	1.7
Cooling/Repump ratio	-	1:1	3:1
Cooling transition (D2-line)	-	$F = 3/2 \rightarrow 5/2$	$F = 9/2 \rightarrow 11/2$
Repumping transition (D2-line)	-	$F = 1/2 \rightarrow 3/2$	$F = 7/2 \rightarrow 9/2$
Linewidth $\Gamma/2\pi$	MHz	5.9	6.0
Detuning of cooling transition	MHz	-40 MHz	-28 MHz
Detuning of repumping transition	MHz	-43 MHz	-32 MHz
Axial B-field gradient	G/cm	25.8 G/cm	36.6 G/cm
Radial B-field gradient	G/cm	13.8 G/cm	20.1 G/cm

Table 4.2: Parameters of the MOTs for ^{6}Li and ^{40}K.

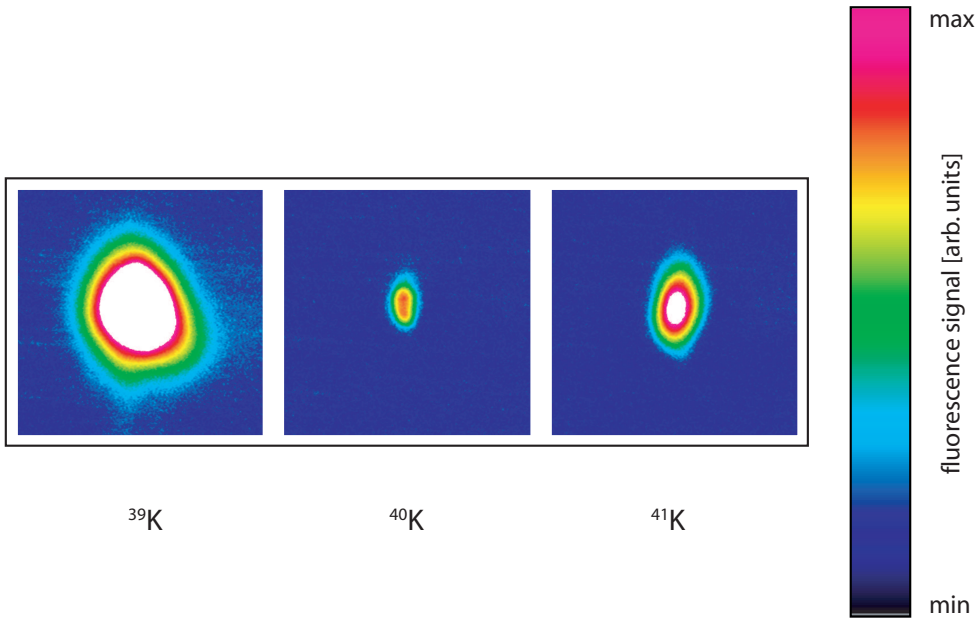

Figure 4.2: False colour fluorescence images of MOTs with different isotopes of potassium. The pictures were taken with the MOT surveillance camera system.

following fibres. This is done by maximizing the loading rate of the ^{40}K MOT. We can load more than 10^6 ^{40}K atoms into the MOT with a loading rate of about 10^5 atoms/s. Figure 4.2 shows fluorescence pictures of the ^{40}K MOT together with the MOTs of ^{39}K and ^{41}K. The latter two isotopes can easily be trapped without realigning the 767 nm laser system by only changing the parameters in the control software. Especially the large and robust ^{39}K MOT is useful to obtain a first signal of a K MOT after installation of the experimental setup. However, as this thesis concentrates on work with the fermions ^{6}Li and ^{40}K, we will not give details about the other two potassium isotopes here.

To create a double-species MOT of ^{6}Li and ^{40}K, we use the following strategy. As outlined in section 3.6, the simultaneous loading of both elements is not favorable with a single configuration of the Zeeman slower. In addition, the optimal magnetic field gradients for the MOT are different for both elements. Therefore, we first load the ^{6}Li MOT and afterwards the ^{40}K MOT. In between, the magnetic fields of the Zeeman slower and the MOT coils are switched to the ^{40}K values. Additionally, the frequencies of the laser beams for the ^{6}Li MOT are adjusted to the new magnetic fields to reduce the loss of ^{6}Li atoms during the loading time of the ^{40}K MOT. The new detuning values are -42 MHz and -45 MHz for the cooling and repumping frequency. This reduces the loss of ^{6}Li atoms to less than 10% per 10 seconds. The fluorescence signal is shown in Fig. 4.3. After switching to the ^{40}K loading, the fluorescence signal of ^{6}Li is lower due to the larger detuning. We did not observe a degradation of the loading rate or lifetime of the ^{40}K MOT due to the presence of ^{6}Li. The loading times depend on the numbers of ^{6}Li and ^{40}K atoms required for the specific experiment. Typical values are between 5 to 30 seconds.

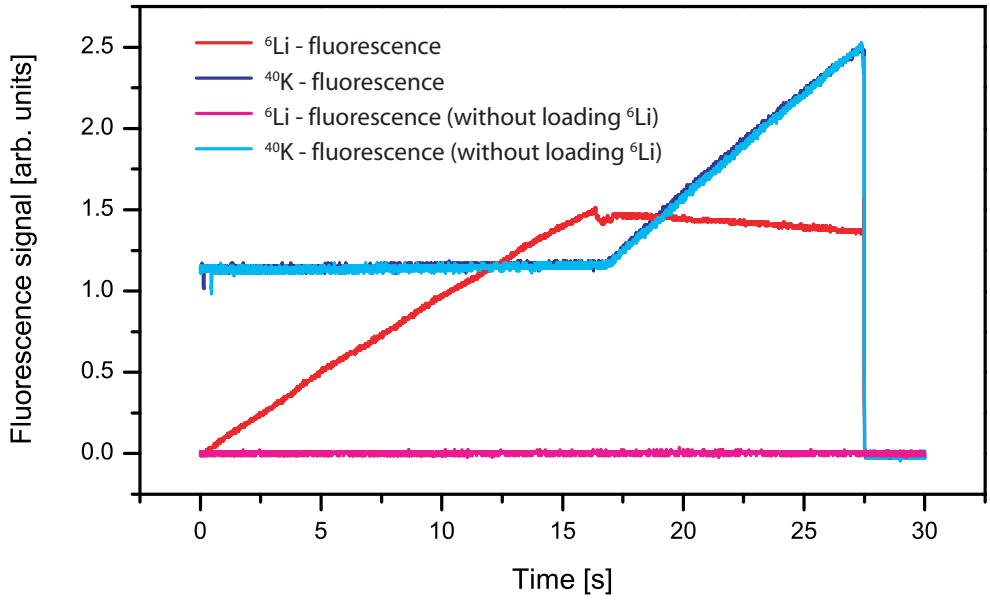

Figure 4.3: Fluorescence signal during the loading sequence for the ^{6}Li-^{40}K MOT. A double MOT is loaded sequentially by first loading ^{6}Li (red) and afterwards ^{40}K (blue). Less than 10% of ^{6}Li is lost during the ^{40}K loading time. A second sequence without loading ^{6}Li (magneta) shows, that the ^{40}K (cyan) does load equally well. The offset of the ^{40}K signal is due to stray light from the MOT beams.

To increase the shot-to-shot stability of the experiment, we do not fix the loading times of the MOT. This could lead to variable atoms numbers for different runs due to variations of the oven flux or other parameters. Therefore, we monitor the fluorescence of the MOT and stop the loading as soon as a specific threshold is reached. Also see section 3.9.3 for technical details, especially the continuous intensity stabilization of the MOT beams is important for this method.

After a two-species MOT is loaded, the atoms are transferred into the dipole trap by compressing the MOT to get higher densities and lower temperatures. This is done by decreasing the detuning of the cooling/repumping laser light to -4 MHz/-7 MHz (-2 MHz/-4 MHz) for ^{6}Li (^{40}K) within 5 ms. Simultaneously, the power of the laser beams is attenuated by a factor of ten. The final temperature of the ^{6}Li atoms is about 300 μK, which is sufficiently cold to keep the atoms trapped in the dipole trap (see next section).

Besides the work with ^{6}Li and ^{40}K, we also tested the operation of the strontium part of the experiment. As only the blue 461 nm laser system was installed at the time, only a relatively short lived Sr MOT was feasible. A repumping laser and/or the laser system for the red intercombination line MOT would allow to create larger and long lived MOTs of Sr. Within these restrictions we could trap the three most abundant isotopes of Sr. Figure 4.4 (a) shows fluorescence pictures. The atom number of the ^{88}Sr MOT was determined to be 10^{6} atoms by taking absorption pictures. In addition, we were able to create the first double MOT of ^{6}Li and

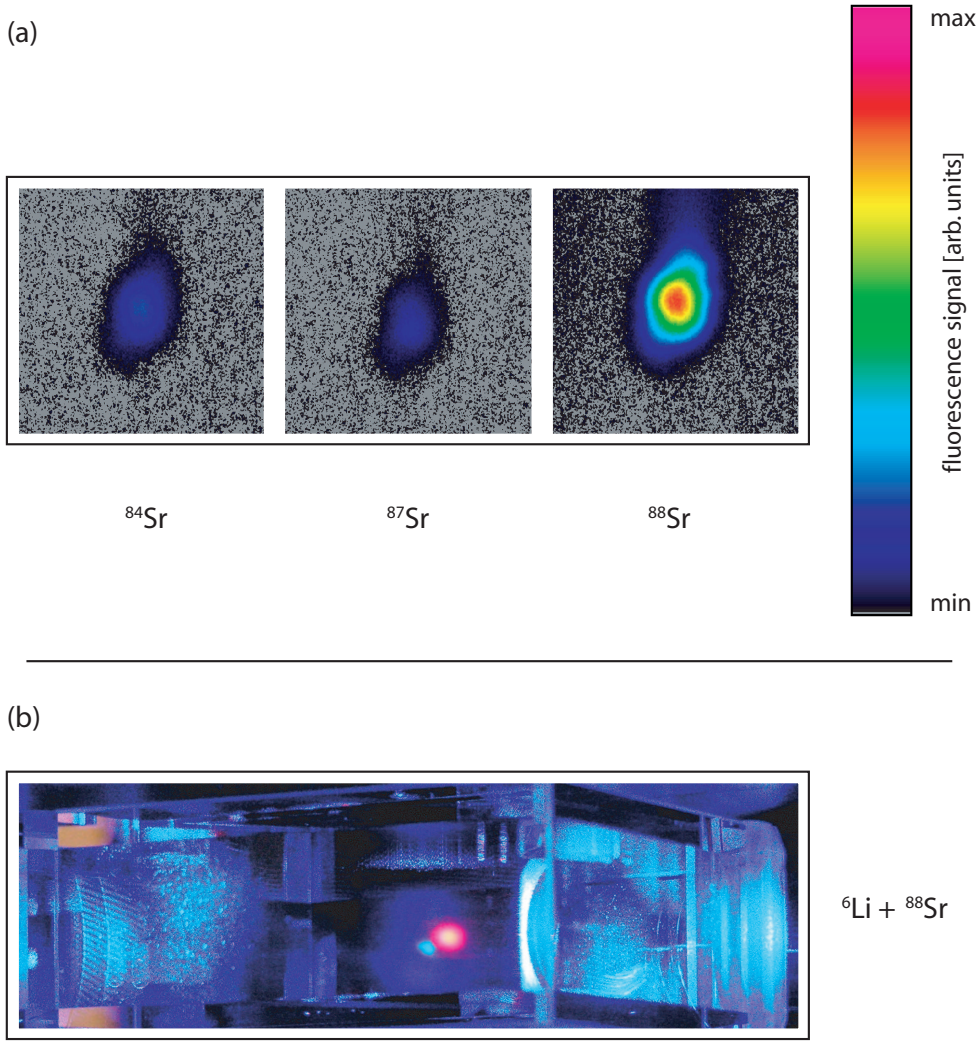

Figure 4.4: (a) False colour fluorescence images of MOTs with different isotopes of strontium. The pictures were taken with the MOT surveillance camera system. Part (b) shows a photo of the first two-species MOT with ^{6}Li and ^{88}Sr.

^{88}Sr. The optimal parameters of the Zeeman slower are very close for both elements, which allows for a simultaneous loading of both MOTs. A photo of this double MOT is shown in Fig. 4.4 (b). The two MOTs are shifted by adjusting the beam balance for better visibility on the photo. To our knowledge, this is the first two-species MOT between an alkali and an alkaline earth element. The similar mixture of Rb-Yb (alkali metal - rare earth metal) is used by the group of A. Görlitz in Düsseldorf [112].

4.2 Trapping and Evaporation in Optical Dipole Traps

Optical dipole traps are a powerful tool to trap atoms and to perform evaporative cooling (see [113] for a review). Using optical instead of magnetic fields allows to use a magnetic field to tune the scattering length. The technical realization of the different dipole traps of the FeLiKx machine are presented in section 3.10. This section will cover the actual performance of the dipole traps with a mixture of ^{6}Li and ^{40}K atoms. Before that, we will briefly introduce the theoretical background of optical dipole traps.

4.2.1 Basics of Optical Dipole Traps

An atom in an oscillating electromagnetic field in the optical regime senses a force. This is caused by the interaction of the induced dipole moment and the field itself. The potential depends on the detuning of the trapping laser frequency ω_{laser} from the optical resonance frequency ω_{atom} of the atom, the linewidth $\Gamma/2\pi$ of the transition and the laser intensity $I(\vec{r})$. In the case the atom can be modelled by a two-level system, and for large detunings, the potential U_{dip} is given by [113]

$$U_{\text{dip}}(\vec{r}) = -\frac{3\pi c^2}{2\omega_{\text{atom}}^3}\left(\frac{\Gamma}{\omega_{\text{atom}}-\omega_{\text{laser}}}+\frac{\Gamma}{\omega_{\text{atom}}+\omega_{\text{laser}}}\right) I(\vec{r}). \tag{4.1}$$

Figure 4.5 shows the potential depth for ^{6}Li, ^{40}K and ^{88}Sr in dependance of the wavelength of the trapping light for a Gaussian beam of 100 μm waist and 100 W power.

For a far-detuned optical dipole trap, the scattering rate can be neglected. The different dipole traps around 1070 nm used in the FeLiKx setup all fulfill this condition. It is useful to know the difference of the trapping potential for the different elements. Table 4.3 shows the ratios for different two-species combinations with a trapping wavelength of 1070 nm.

	^{6}Li	^{40}K	^{88}Sr
^{6}Li	1	2.1	0.91
^{40}K	0.47	1	0.43
^{88}Sr	1.1	2.3	1

Table 4.3: Ratio of trap depth for different dual species dipole traps at 1070 nm. The values in the table are defined as $U_{\text{dip}}^{\text{upperrow}}/U_{\text{dip}}^{\text{leftcolumn}}$.

Another important parameter of optical dipole traps are the oscillation frequencies of the trapped atoms. As most optical dipole traps are created with a single-mode laser beam, the shape $I(\vec{r})$ of the trap corresponds to the shape of a Gaussian laser beam. A useful approximation is possible, if the atoms have an energy much lower than the total trap depth and are only located in

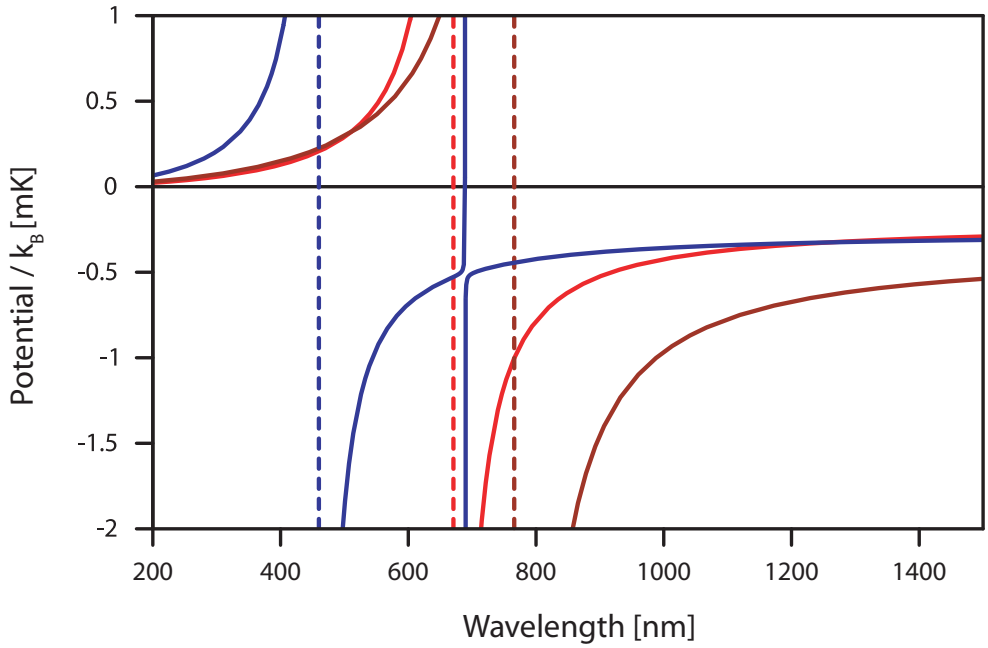

Figure 4.5: Optical dipole trap potentials for Li (red), K (brown) and Sr (blue). The resonance positions are indicated with dashed lines. The potential was calculated for a single-focus 100 W beam with a waist of 100 μm.

the center. This allows to use a harmonic potential for the dipole trap. The trapping frequencies ω_{rad} and ω_{ax} in the radial and axial direction become [113]

$$\begin{aligned} \omega_{\text{rad}} &= \sqrt{\frac{4U_{\text{max}}}{mw_0}} \\ \omega_{\text{ax}} &= \sqrt{\frac{2U_{\text{max}}}{mz_0}}, \end{aligned} \tag{4.2}$$

where U_{max} is the trap depth, w_0 the waist and z_0 the Rayleigh length. Using the harmonic potential approximation also simplifies the theoretical treatment of trapped gases in many cases. Table 4.4 shows the frequency ratios for different two-species combinations with a trapping wavelength of 1070 nm.

While the ground state of an atoms in a dipole trap is shifted to lower energies due to the presence of the red detuned light, the shift of the excited states can be different. Therefore, optical dipole traps also induce a light shift on the optical transitions. In many cases, the light shift for a far-detuned dipole trap is below the typical linewidth of about 10 MHz for alkali elements and can be neglected. But the combination of ^{40}K with infrared dipole traps is different. ^{40}K has two optical transitions between the excited $4^2\text{P}_{3/2}$ state and the $5^2\text{S}_{1/2}$ and $3^2\text{D}_{5/2}$ states with wavelengths of 1252 nm and 1177 nm and linewidths of 2 MHz and 4 MHz, respectively. For high intensities of the dipole trap laser at 1070 nm, these resonances shift the $4^2\text{P}_{3/2}$ state

	^{6}Li	^{40}K	^{88}Sr
^{6}Li	1	0.56	0.25
^{40}K	1.8	1	0.44
^{88}Sr	4.0	2.3	1

Table 4.4: Ratio of trap frequencies for different dual species dipole traps at 1070 nm. The values in the table are defined as $\omega_{\text{dip}}^{\text{upperrow}}/\omega_{\text{dip}}^{\text{leftcolumn}}$. The ratio is identical for radial and axial trapping frequencies.

by several 100 MHz. An additional complication occurs as the light shift in the dipole trap is inhomogeneous because of the laser beam profile. Consequently, the shift for an atom depends on its location in the trap. This shift can strongly affect the behavior of the CMOT, optical pumping and imaging and has to be taken into account. A small light shift is also present for ^{6}Li but it does not affect the experimental procedures significantly.

4.2.2 Optical Dipole Traps in the FeLiKx Setup

This section describes different optical dipole trap configurations that have been studied on the FeLiKx project so far. We have tested different crossing configurations of the four passages through the glass cell (see section 3.10.1). A trap with a crossing of two counter-propagating beams with orthogonal polarization showed the longest lifetime of the trapped atoms. All other configurations (four crossings, co-propagating beams and/or parallel polarization) showed a significant loss of atoms within a few seconds. Possible explanations for the losses are heating due to residual interferences[1] of the beams or Raman processes. However, the two-beam crossing configuration mentioned above was sufficient for many experiments and did not show unusual losses. Therefore, we did not investigate the details of the other configurations.

The crossed high-power dipole trap is formed by one 68 W and one 52 W laser beam with a wavelength of 1070 nm. The losses of the second beam are mostly due to reflections at the glass cell. Assuming a precise overlap of the two focal points, the trap depth is about 1.7 mK for ^{6}Li and 3.6 mK for ^{40}K. The oscillation frequencies for ^{6}Li have been determined to be $\omega_{\text{rad}}/2\pi = 13$ kHz and $\omega_{\text{ax}}/2\pi = 1.7$ kHz. For ^{40}K this results in $\omega_{\text{rad}}/2\pi = 7.3$ kHz and $\omega_{\text{ax}}/2\pi = 1.0$ kHz.

The depth of the trap is large enough to capture a large amount of atoms from the compressed MOT. We can easily load 10^7 ^{6}Li atoms and 10^5 ^{40}K atoms. To obtain a stable dipole trap, the trapping beams are already switched on during the end of the MOT loading sequence. This gives enough time after which the thermal lensing of the high-power beam does not change anymore. Switching on the CMOT reduces the temperature of the atoms to 300 μK. The CMOT

[1] The coherence length of the fibre laser is below 10 μm and interference effects should be very small.

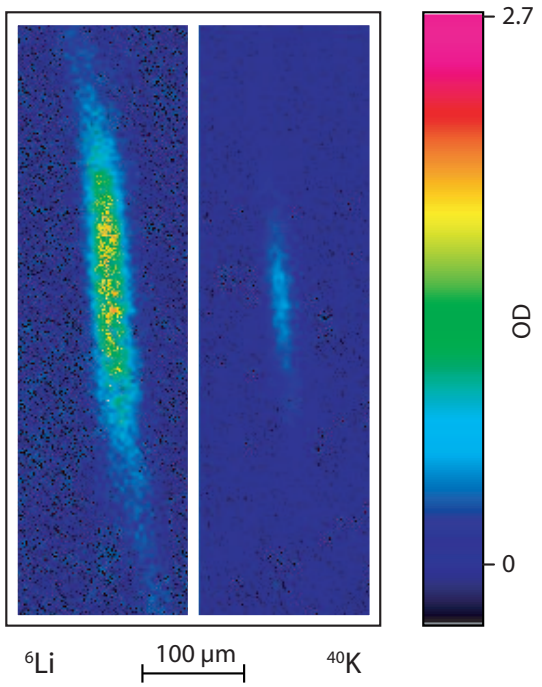

Figure 4.6: Absorption pictures of a ^{6}Li$|a\rangle$-^{40}K$|a\rangle$ mixture in a crossed dipole trap. The trap is made of two high-power infrared laser beams, which cross under an angle of 12°. The ^{6}Li atoms also populate the outer region of the stronger one of the two crossed laser beams.

sequence lasts 10 ms during which the atoms are transferred into the dipole trap. As the CMOT delivers atoms in different spin states, optical pumping is performed to transfer them into the lowest hyperfine state. For ^{6}Li, the optical pumping is implemented by switching off the repumping laser beam 100 μs before the cooling laser. For ^{40}K, the situation is more complicated because of the strong inhomogeneous light shift. We could implement optical pumping by using a bias field of 570 G after the MOT is switched off. At this magnetic field, light with a frequency offset of -300 MHz from the $4^2S_{1/2}|F = 9/2, m_F = -9/2\rangle$ to $4^2P_{3/2}|F = 11/2, m_F = -11/2\rangle$ transitions transfers most (up to 90%) of the trapped atoms into the ground state. Working at large detuning allows to address all ^{40}K m_F-states similarly, but requires one second of pumping time for light intensities of 0.5 mW/cm^2. In addition to the optical pumping, the spin relaxation between ^{6}Li$|b\rangle$ and the K-atoms in the higher Zeeman levels takes place as described in section 2.2.3. The detailed dynamics of the population of the ground state in presence of ^{6}Li$|b\rangle$ and the pumping light is not yet fully understood and further investigations are in progress. We optimized the procedure to reach optimal atom numbers of both species. This allows us to prepare a ^{6}Li$|a\rangle$-^{6}Li$|b\rangle$-^{40}K$|a\rangle$ mixture with the atom numbers mentioned at the beginning of this paragraph. Figure 4.6 shows absorption pictures of ^{6}Li$|a\rangle$ and ^{40}K$|a\rangle$ in the crossed high-power dipole trap.

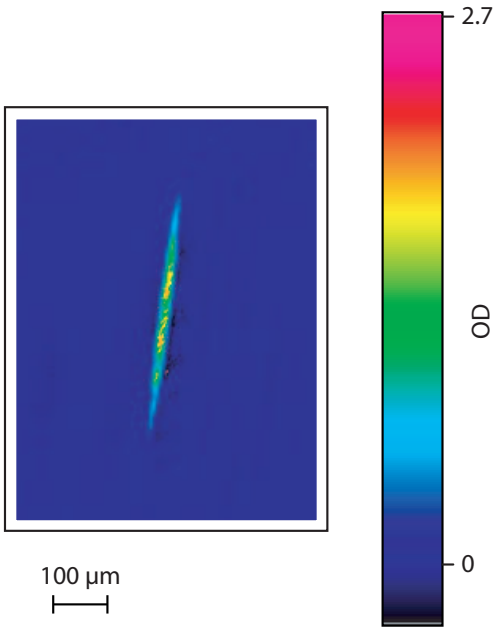

Figure 4.7: Absorption image of ^{6}Li inside a high-power optical dipole trap with an axial confinement using a magnetic field curvature.

Using a crossed optical dipole trap has two significant advantages. First, the two beams add up their intensity and give a deeper trap compared to a single focus. The second benefit is the better axial confinement due to the crossing. But especially together with high optical powers, the crossed configuration also has some important disadvantages. The high-power beam causes thermal lensing in the different optical elements it passes. The thermal lensing leads to a shift of the focal position of the dipole trap if the laser power is changed. This can be well reproduced for repeating sequences and does not influence the shot-to-shot stability. But it significantly shifts the crossing during the evaporation sequence. Although the evaporation performs well, the precise shape of the trap changes as the two focal points do not overlap during the whole sequence. This behavior is difficult to measure. The trap is much less harmonic under these conditions. This makes interpretation based on the shape of the atomic cloud very difficult. Therefore, an alternative trap is required to work with a well-known trap geometry.

The FeLiKx setup offers two possible solutions. First, a single-focus high-power optical dipole trap can be used while a magnetic field curvature is used for additional axial confinement. This solution gives a more shallow trap depth and the single focus still shifts. However, this shift does not change the trap shape in a very complicated way. An alternative solution is to transfer the atoms from the high-power dipole trap (crossed or single-focus) into another trap with higher precision. This is the purpose of the low-power dipole trap described in section 3.10.2. At low power no significant thermal lensing occurs and single-focus or crossed configurations can be

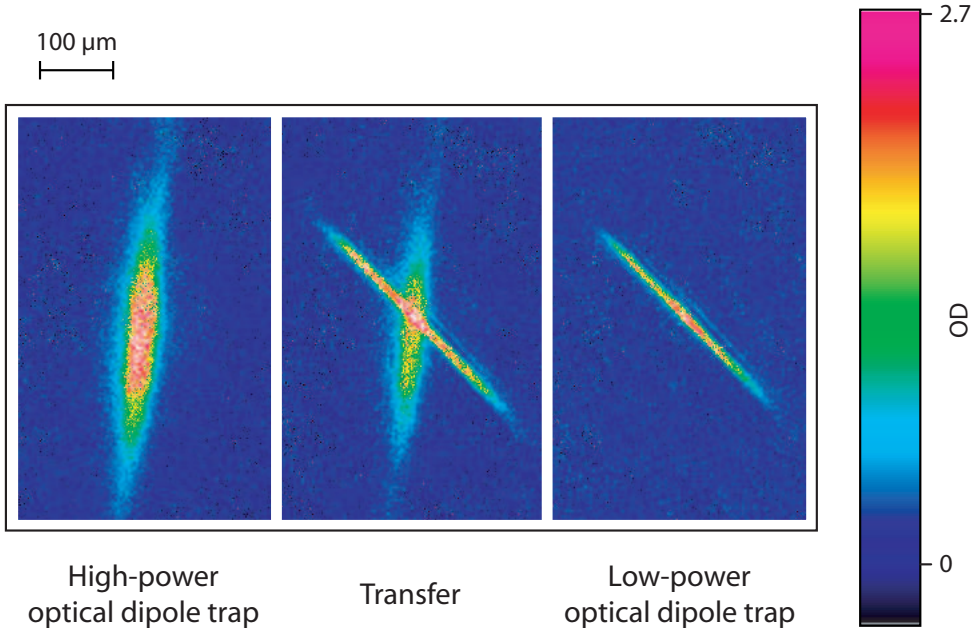

Figure 4.8: Absorption images of ^{6}Li during the transfer from the high-power crossed beam trap into the low-power single-focus trap.

implemented precisely and stable. The precise characterization of the different possibilities will be presented in future publications. First results of trapped atoms in a single-focus high-power dipole trap and a low-power trap are shown in Fig. 4.7 and Fig. 4.8.

4.3 Sympathetic Cooling of ^{40}K with ^{6}Li

After the transfer into the dipole trap, the atoms have a temperature of several 100 μK. This is still higher than the corresponding Fermi temperature. Evaporative cooling is used to approach the quantum-degenerate regime [21]. The evaporative cooling process is most efficient, if the elastic collisions are much higher than inelastic processes leading to atom loss. This is the case for a mixture of ^{6}Li$|a\rangle$-^{6}Li$|b\rangle$ around the Feshbach resonance at 834 G. If the scattering length of a single species is not high enough for evaporative cooling, it can be cooled sympathetically by a second species [114, 115, 116, 117]. In this case, the second species is evaporated and the first species stays in thermal equilibrium during the process. ^{40}K$|a\rangle$ can be cooled sympathetically by the ^{6}Li atoms, if the scattering length between both atoms is high enough. As the ^{6}Li-^{40}K scattering properties were unknown before our experiments, showing the feasibility of sympathetic cooling is an important step.

The evaporation sequence is first optimized for the homonuclear ^{6}Li$|a\rangle$-^{6}Li$|b\rangle$ mixture. The atoms are loaded into a crossed beam high-power optical dipole trap. We prepare the ^{6}Li atoms

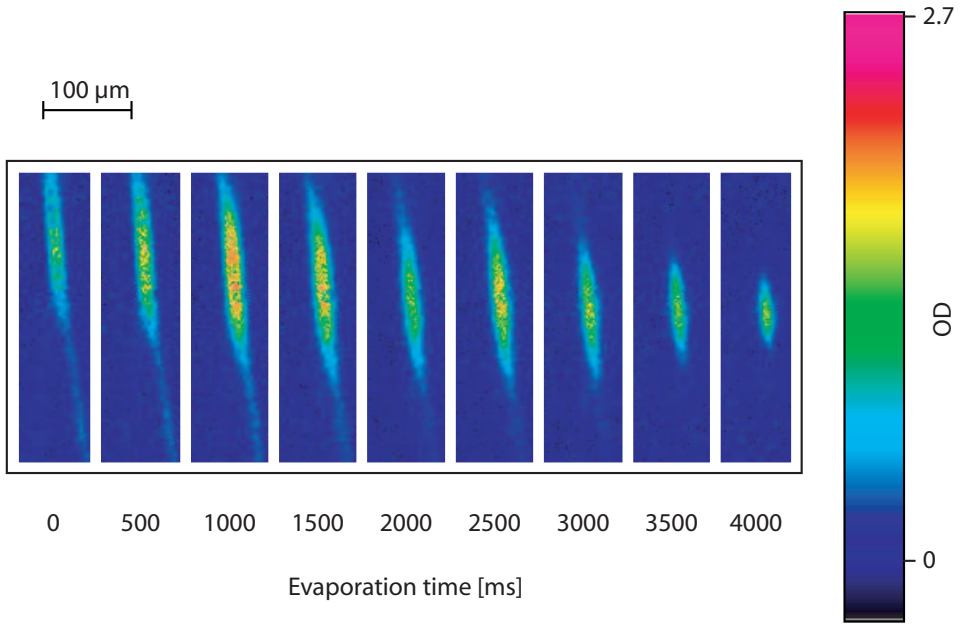

Figure 4.9: Evaporative cooling of ^{6}Li. The figure shows absorption pictures of $^{6}\text{Li}|a\rangle$ inside the crossed high-power optical dipole trap.

in a 50/50 ratio of the lowest two Zeeman levels by applying a sequence of 40 radiofrequency sweeps with a frequency from 76.05 MHz to 76.25 MHz at a magnetic field of $B = 762$ G [54]. Afterwards, the power of the dipole trap laser is attenuated by exponentially decreasing the radiofrequency power of the single-pass AOMs (see section 3.10.1). A typical sequence lowers the laser power by a factor of 160 within a time of 4000 ms. It is important to note, that the trap depth is not proportional to the laser power due to the thermal shifting of the crossing. The evolution of the evaporation is shown in Fig. 4.9. The absorption pictures of $^{6}\text{Li}|a\rangle$ have been taken inside the dipole trap. The light shift is clearly visible at the beginning and leads to a weakened signal. The focal shift due to the thermal lensing is also visible in the vertical shift of the cloud. During the evaporation, the number of ^{6}Li atoms decreases from a few 10^6 to 10^5.

As soon as the temperature drops below the molecular binding energy of $^{6}\text{Li}|a\rangle$-$^{6}\text{Li}|b\rangle$ (2 μK at 762 G), bosonic ^{6}Li pairs start to form. Further evaporation decreases the temperature below the BEC transition. At the end of the evaporation, we can create a molecular BEC of $^{6}\text{Li}_2$ as shown in Fig. 4.10. The unknown geometry of the crossed dipole trap makes it difficult to characterize the BEC. A discussion of the creation of degenerate gases of ^{6}Li and ^{40}K will be the topic of future work. Here, we will proceed with the sympathetic cooling process of ^{40}K.

For sympathetic cooling of ^{40}K, the atoms are loaded into the crossed dipole trap together with a mixture of $^{6}\text{Li}|a\rangle$-$^{6}\text{Li}|b\rangle$. The loading process is described in the previous section 4.2.2. After the simultaneous loading of both species, the evaporation sequence is performed in the

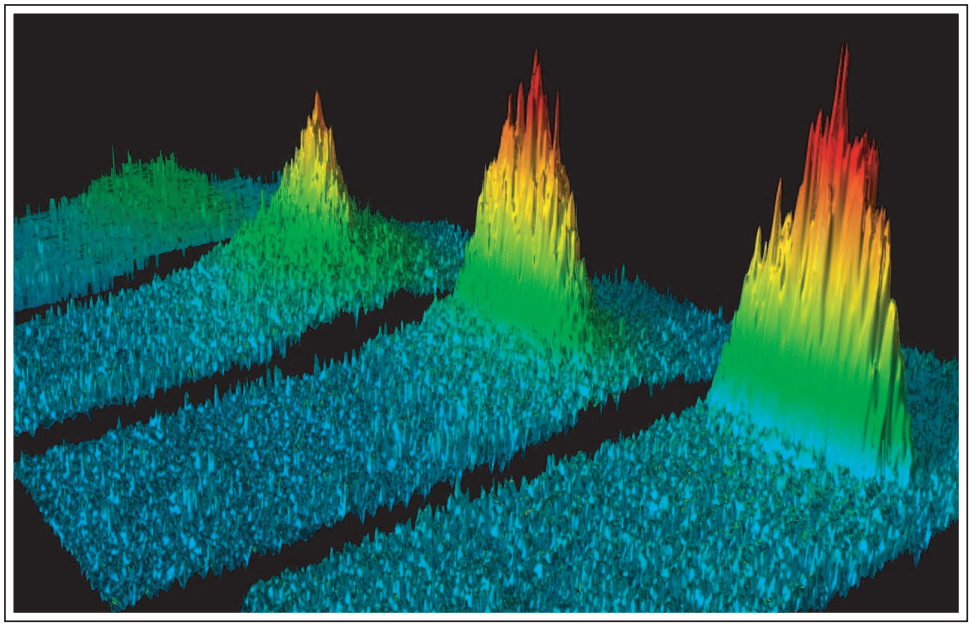

Figure 4.10: Three dimensional representation of the absorption images during the formation of a molecular $^6Li_2$ BEC. The evaporative cooling was stopped after 4.3 s, 4.7 s, 4.8 s, and 5.1 s from the upper to the lower picture. The absorption images were taken 10 ms after releasing the atoms from the dipole trap.

same way as described above for the homonuclear case of ^{6}Li. The evolution of the evaporation is shown in Fig. 4.11. The ^{6}Li atoms are evaporated in the same way as without the presence of ^{40}K. Only the overall number of ^{6}Li is reduced by 20% due to the addition of ^{40}K. The ^{40}K atom number of the example shown in Fig. 4.11 decreases from initially 30,000 atoms to about 4000 at an evaporation time of 3750 ms.

The temperature of a thermal cloud of atoms can be easily determined by measuring the size of an expanding cloud after being released from the trap. The size of the cloud is determined by fitting a Gaussian function with a width σ_x to the radial profile of the absorption picture. The width is related to the temperature T by [114]

$$\sigma_x^2(t) = \sigma_x^2(t=0) + \frac{k_B T}{m} t^2, \tag{4.3}$$

where t is the time of flight after the release from the trap and m is the mass of the atomic species. Taking absorption pictures for several values of t allows to fit equation (4.3) and to extract the temperature. However, this relation is only valid for a thermal gas of atoms. For lower temperatures and higher densities, the mean field energy and quantum statistics can severely influence the expansion. Furthermore, the formation of molecules would require to use twice the mass for the expanding particles. Therefore, we only use this procedure for the initial phase of the evaporation. The temperature at the end of the evaporation can be determined by taking

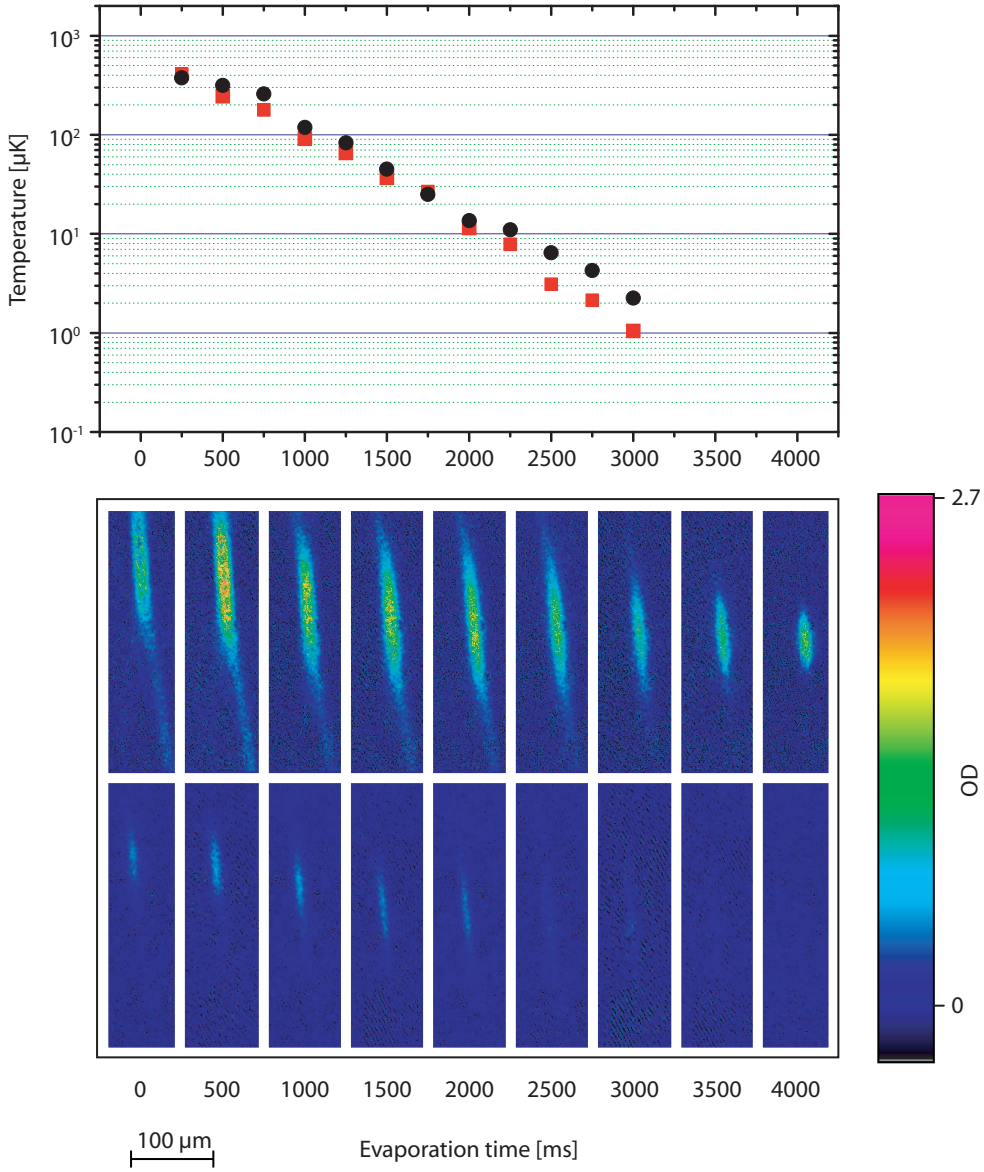

Figure 4.11: Evaporative cooling of ^{6}Li with ^{40}K. The lower part of the figure shows absorption pictures of $^{6}\mathrm{Li}|a\rangle$ (upper row) and $^{40}\mathrm{K}|a\rangle$ (lower row) inside the crossed high-power optical dipole trap. Above, the temperatures of the ^{6}Li atoms (red squares) and ^{40}K atoms (black dots) is shown.

into account the effects mentioned above. But this requires a better knowledge of the geometric shape of the trap as available for the high-power crossed beam configuration.

The resulting temperatures for the first 3000 ms of the evaporation are presented in the upper part of Fig. 4.11. During this time, the temperature decreases by more than two orders of magnitude. Initially, the temperature of ^{40}K (black dots) is the same as for ^{6}Li (red squares) although the trap is two times deeper for ^{40}K. The ^{40}K atoms thermalize with the ^{6}Li cloud and are sympathetically cooled during the evaporation. At the end of the evaporation, the temperature of ^{40}K does not completely follow the cooling process anymore. Here, the evaporation was too fast. A slower evaporation ramp can be used to achieve full thermalization.

The presented results prove the feasibility of sympathetic cooling of $^{40}\mathrm{K}|a\rangle$ by a mixture of $^{6}\mathrm{Li}|a\rangle$-$^{6}\mathrm{Li}|b\rangle$ on the molecular side of the Feshbach resonance at 834 G. The preparation of ultracold heteronuclear mixtures of fermions is possible with this technique. Studying the physics of this three component Fermi-mixture around the Feshbach resonance will be a topic of future work. This thesis concentrates on the exploration of heteronuclear Feshbach resonances, which are presented in the following chapter.

Chapter 5

Interspecies Feshbach Resonances of ^{6}Li and ^{40}K

Feshbach resonances can be detected by several different methods [24]. We use the detection of inelastic losses of the trapped atoms in dependence of the magnetic field. Around a Feshbach resonance, the inelastic losses are strongly enhanced due to the coupling with a bound state of the closed channel.

Before our experiments, no predictions about ^{6}Li-^{40}K Feshbach resonances were available. To achieve a complete understanding about the structure of the resonances, it is required to measure as many resonances as possible. If only very few resonances would be measured, the theoretical models may not give an unambiguous assignment. It is especially helpful to find resonances for different open channels, because the structure across the different channels can give valuable information for the difficult fitting procedure of the models. Our method of preparing the atoms in different open channels and performing inelastic loss spectroscopy are presented in section 5.1. The experimental results are presented in section 5.2 and discussed in section 5.3.

5.1 Spin Selective Inelastic Loss Spectroscopy

The starting point for the inelastic loss spectroscopy is the preparation of a cold ^{6}Li$|a\rangle$-^{6}Li$|b\rangle$-^{40}K$|a\rangle$ mixture. The detailed procedure is described in chapter 4. For the Feshbach resonance measurements, the evaporation is stopped after 2500 ms. This results in a mixture with 10^5 ^{6}Li atoms in each of the two spin states and about 10^4 ^{40}K$|a\rangle$ atoms at a temperature of 4 μK. At this temperature, the formation of ^{6}Li$_2$ molecules is negligible.

Starting with this three-component Fermi mixture, different two-component Fermi mixtures can be prepared. We restricted our experiments to several of the lowest Zeeman levels of the two elements, as they are most easy to prepare.

The ^{6}Li$|a\rangle$ or ^{6}Li$|b\rangle$ component is selected by removing the unwanted atoms using resonant light from the imaging beam at a magnetic field of $B = 762$ G. The ^{6}Li$|c\rangle$ state can be prepared by transferring a sample of pure ^{6}Li$|b\rangle$ atoms using adiabatic rf-sweeps. We use a 100 ms sweep from 83.557 MHz to 83.561 MHz at a magnetic field of 605.3 G[1]. Afterwards, atoms left in the lower spin states are cleaned using resonant light at $B = 762$ G. These methods allow to prepare pure samples of any of the lowest three ^{6}Li Zeeman states.

The preparation of the ^{40}K spin states works very similar. After the evaporation, the ^{40}K atoms are all in the lowest Zeeman state as discussed in section 4.2.2. Higher lying states are prepared using rf-sweeps at 476.6 G. The transition to the ^{40}K$|b\rangle$ state is done with a 25 ms sweep from 74.900 MHz to 75.100 MHz. The next transition to the ^{40}K$|c\rangle$ state requires 79.690 MHz to 75.890 MHz. Residual atoms in the lower states are again cleaned with resonant light at 769.5 G.

With a suitable order of the above rf-transitions and cleaning pulses, any two-component mixture with the lowest three Zeeman states of ^{6}Li-^{40}K can be created. The following combinations are stable against spin relaxation and are ideal candidates to perform inelastic loss spectroscopy:

$$\begin{aligned}
^6\mathrm{Li}|a\rangle &- {}^{40}\mathrm{K}|a\rangle \\
^6\mathrm{Li}|b\rangle &- {}^{40}\mathrm{K}|a\rangle \\
^6\mathrm{Li}|c\rangle &- {}^{40}\mathrm{K}|a\rangle \\
^6\mathrm{Li}|a\rangle &- {}^{40}\mathrm{K}|b\rangle \\
^6\mathrm{Li}|a\rangle &- {}^{40}\mathrm{K}|c\rangle
\end{aligned}$$

After preparing one of those two-component mixtures, the intensity of the dipole trap laser is increased by 5 dB to achieve a higher density of the atoms. The temperature rises to 12 μK and the peak density of ^{6}Li and ^{40}K increases to 10^{12} cm^{-3} and 10^{11} cm^{-3}, respectively.

In the next step, the magnetic field is set to a value between 0 G and 750 G. During 10 s, the magnetic field is increased by 0.3 G. During this time, atoms are lost mainly due to three-body processes. In addition to the loss of atoms, the sample is also heated. The heated atoms are removed by lowering the dipole trap laser power by 4.5 dB (i.e. 0.5 dB above the initial evaporation end-value) after the 10 s scan. This lowering of the trap depth is always done at a magnetic field of 55.6 G to exclude the effect of different residual magnetic potentials. The remaining atoms are recaptured in a dual-species MOT and the fluorescence is recorded using two CCD cameras (see section 3.9.2). The whole procedure is repeated across the magnetic field range of $0 - 750$ G with a step size of 0.3 G.

[1]The rf-sweeps are often done at magnetic fields at which absorption imaging is easily feasible for the different spin states with an available resonant laser beam. This simplifies testing of the rf-transfers.

5.2 Measurement Results

The fluorescence signal of the recaptured atoms is in a good approximation proportional to the number of atoms remaining in the dipole trap. A low fluorescence signal for a specific magnetic field is an indicator of increased loss. If this loss is due to a heteronuclear Feshbach resonance, the atom number for both species, ^{6}Li and ^{40}K, decreases. Consequently, the density of both elements also decreases during the holding time. With decreasing densities, the loss rates also becomes smaller, even to the extend that background loss processes not related to the Feshbach resonances dominate. This limits the signal to noise ratio of the fluorescence signal.

This limit can be overcome by using a large reservoir of 10 times more ^{6}Li atoms than ^{40}K atoms. The density of ^{6}Li does not change a lot while the density of ^{40}K can decrease exponentially with nearly constant rate. In this case, it is possible to loose practically all ^{40}K atoms due to inelastic collisions with ^{6}Li. With this method, the ^{40}K atoms are used as a probe that gives a good signal to noise ratio of the loss signal around a heteronuclear resonance.

The fluorescence signal of the recaptured ^{40}K atoms is shown in the Figs. 5.1 to 5.4 on the following pages for the four different channels $^6\mathrm{Li}|b\rangle$-$^{40}\mathrm{K}|a\rangle$, $^6\mathrm{Li}|a\rangle$-$^{40}\mathrm{K}|a\rangle$, $^6\mathrm{Li}|a\rangle$-$^{40}\mathrm{K}|b\rangle$ and $^6\mathrm{Li}|a\rangle$-$^{40}\mathrm{K}|c\rangle$. The holding time in the dipole trap was 10 s.

Regions of the magnetic field with low fluorescence values have been measured several times. Reproducible loss features are indicated with arrows. Fluorescence values significantly below the background signal that were not reproducible have been removed from the figures. They can be attributed to technical perturbations. The irregularities of the background signal are caused by changing operating conditions of the FeLiKx machine during the many weeks of data taking.

The preparation of the ^{40}K atoms in the $|c\rangle$-state shows a much larger shot-to-shot instability compared to the other rf-transfers. As all the heteronuclear resonances in the other channels were located below 300 G, only this region of the magnetic field was measured for the $^6\mathrm{Li}|a\rangle$-$^{40}\mathrm{K}|c\rangle$ combination (see Fig. 5.4).

Having a dual-species mixture of ^{6}Li-^{40}K, it is important to distinguish between homonuclear losses and heteronuclear ones. Homonuclear losses of one species occur also if the other species is not present. This is the case at the magnetic fields of the known homonuclear Feshbach resonances presented in section 2.3.3. All reproducible loss features of ^{40}K have been measured also without the presence of ^{6}Li to decide about their homo- or heteronuclear character. In the Figs. 5.1 to 5.4, homonuclear resonances are marked with blue arrows, while red arrows show heteronuclear resonances.

In total, we could identify thirteen different heteronuclear resonances in the four different channels $^6\mathrm{Li}|b\rangle$-$^{40}\mathrm{K}|a\rangle$, $^6\mathrm{Li}|a\rangle$-$^{40}\mathrm{K}|a\rangle$, $^6\mathrm{Li}|a\rangle$-$^{40}\mathrm{K}|b\rangle$ and $^6\mathrm{Li}|a\rangle$-$^{40}\mathrm{K}|c\rangle$. The details of these resonances are listed in table 5.1, together with the results of two different theoretical models [62]. The two models are able to attribute all thirteen loss features to heteronuclear Feshbach

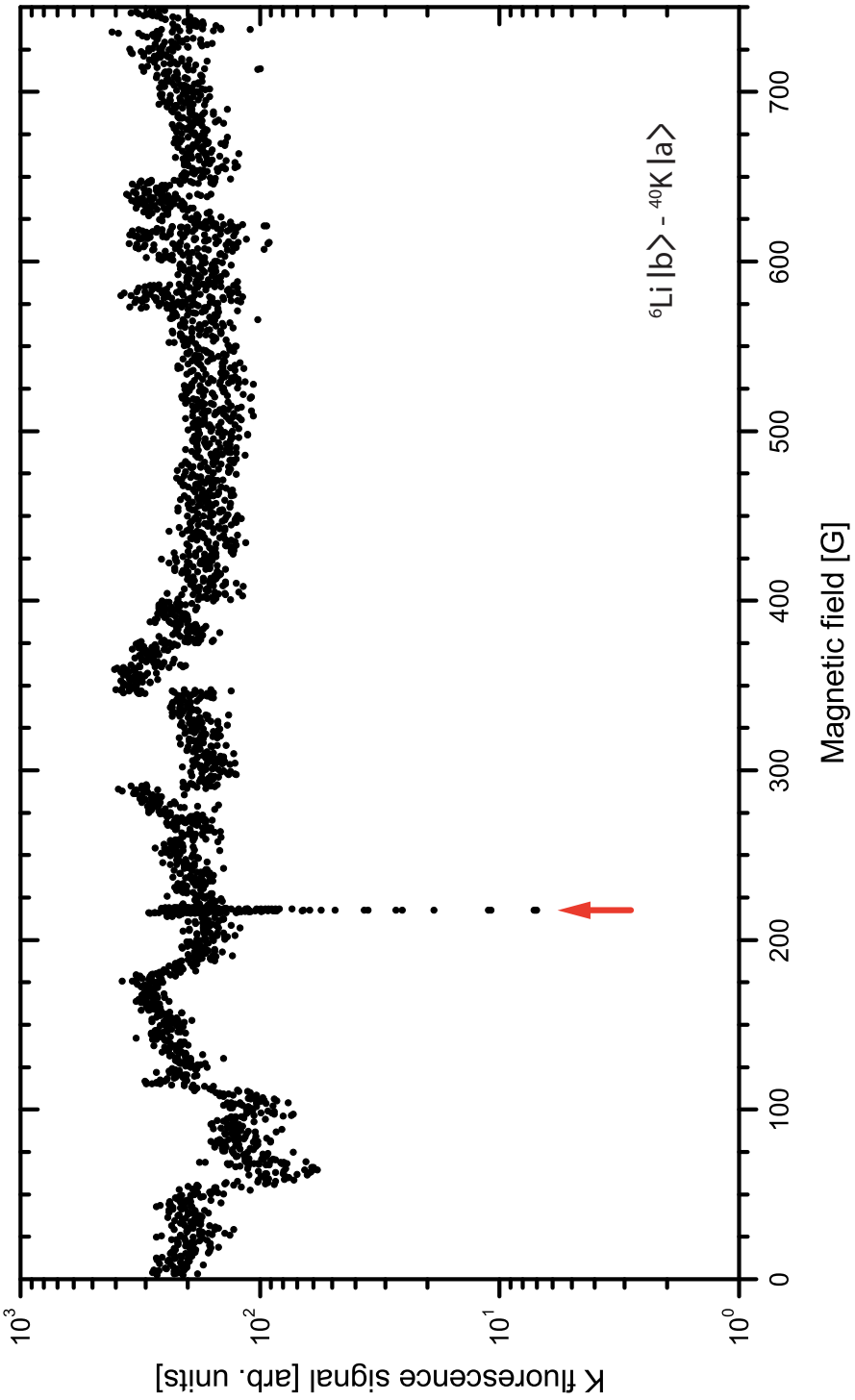

Figure 5.1: Inelastic loss spectroscopy scan for ^{40}K in a ^{6}Li$|b\rangle$-^{40}K$|a\rangle$ mixture. Arrows indicate heteronuclear (red) or homonuclear (blue) resonances.

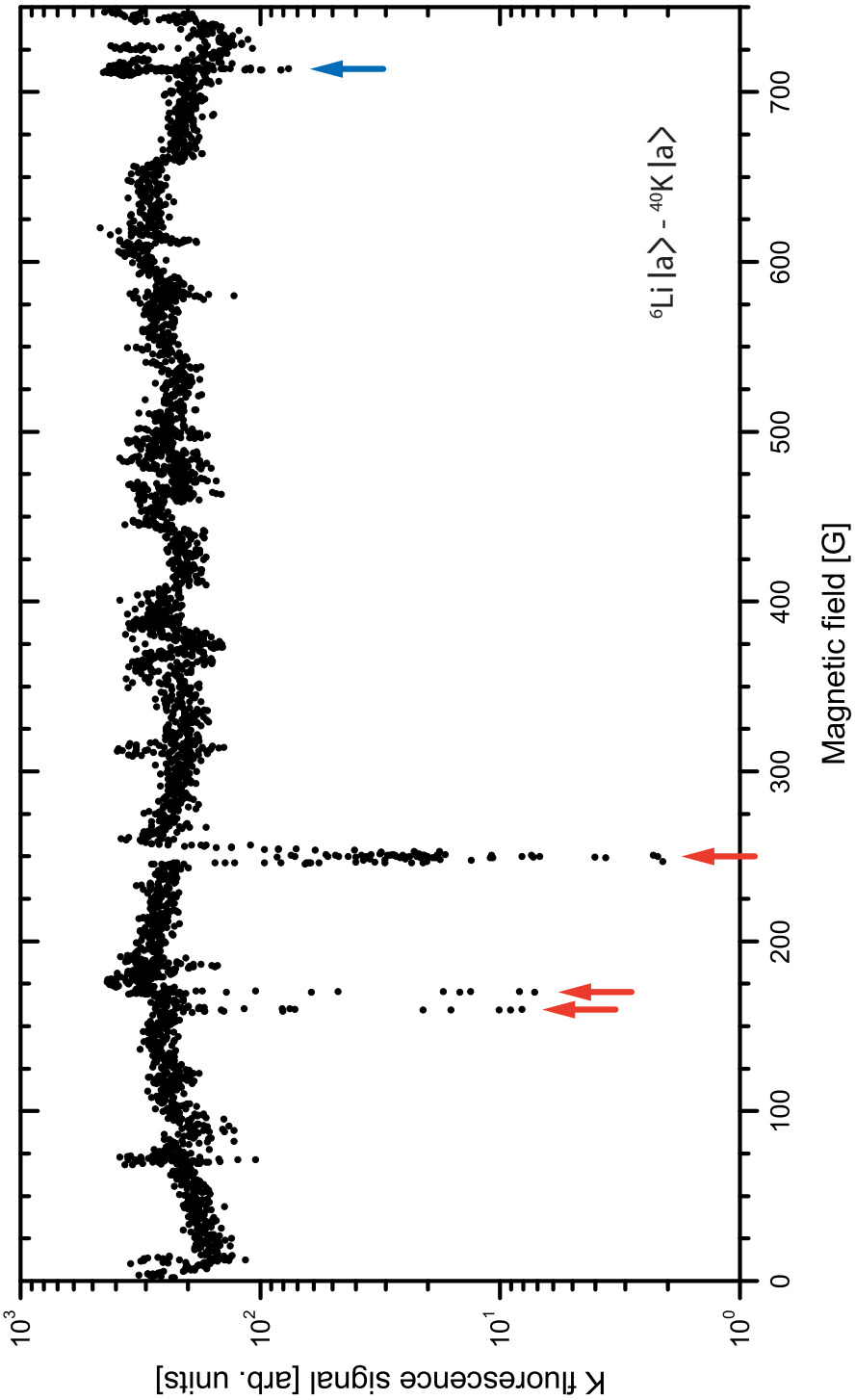

Figure 5.2: Inelastic loss spectroscopy scan for ^{40}K in a ^{6}Li$|a\rangle$-^{40}K$|a\rangle$ mixture. Arrows indicate heteronuclear (red) or homonuclear (blue) resonances.

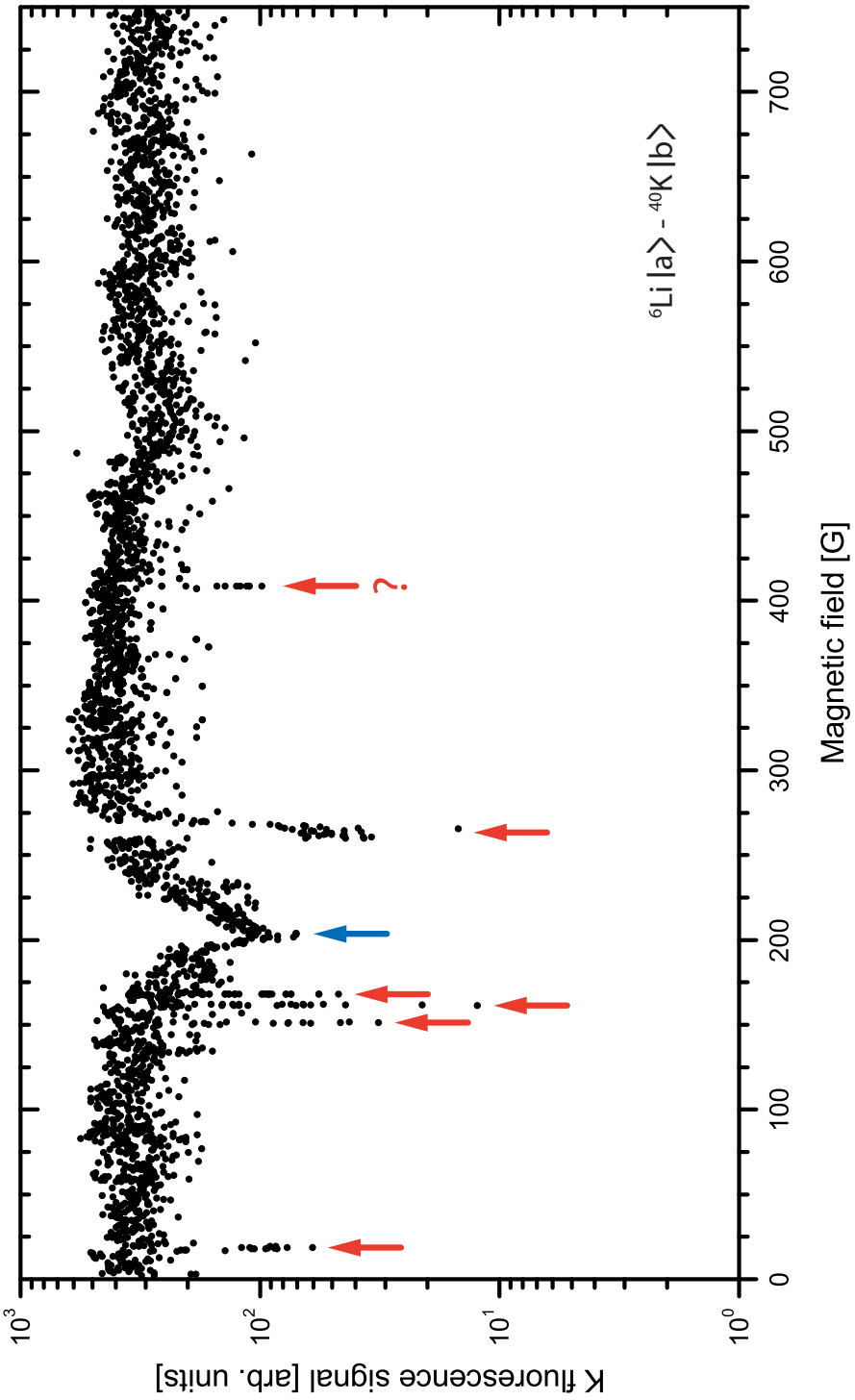

Figure 5.3: Inelastic loss spectroscopy scan for ^{40}K in a ^{6}Li$|a\rangle$-^{40}K$|b\rangle$ mixture. Arrows indicate heteronuclear (red) or homonuclear (blue) resonances.

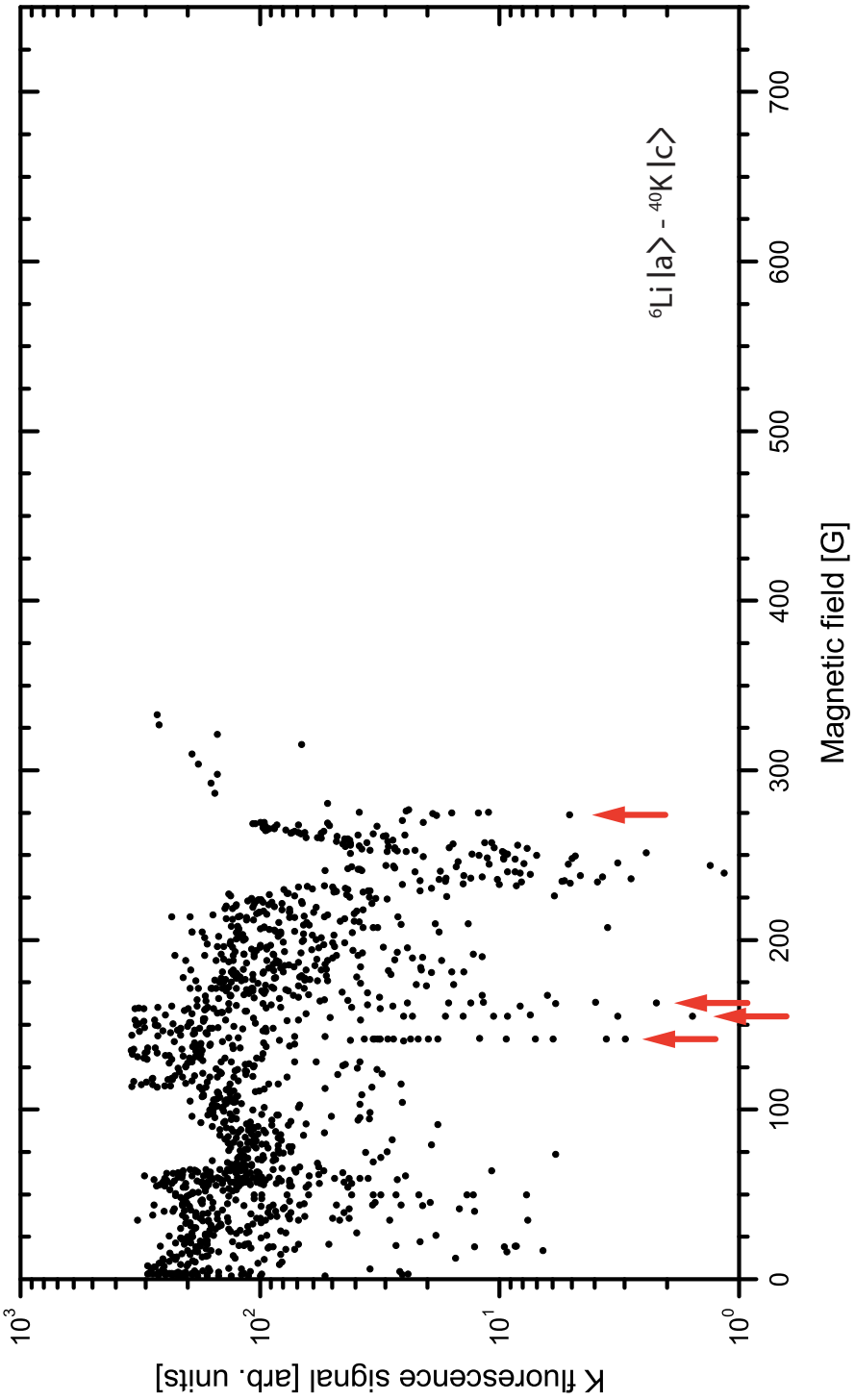

Figure 5.4: Inelastic loss spectroscopy scan for ^{40}K in a ^{6}Li$|a\rangle$-^{40}K$|c\rangle$ mixture. Arrows indicate heteronuclear (red) or homonuclear (blue) resonances.

		Experiment		ABM	Coupled-channels		
channel	m_F	$B_{\text{res}}[G]$	$\Delta B_{\text{exp}}[G]$	$B_{\text{res}}[G]$	$B_{\text{res}}[G]$	ΔB [G]	type
^{6}Li$\|b\rangle$-^{40}K$\|a\rangle$	-5	215.6	1.7	216.7	215.6	0.25	s
^{6}Li$\|a\rangle$-^{40}K$\|a\rangle$	-4	157.6	1.7	158.4	158.2	0.15	s
^{6}Li$\|a\rangle$-^{40}K$\|a\rangle$	-4	168.2	1.2	169.2	168.2	0.10	s
^{6}Li$\|a\rangle$-^{40}K$\|a\rangle$	-4	249.1	10.7	244.3	249.5	-	p
^{6}Li$\|a\rangle$-^{40}K$\|b\rangle$	-3	16.1	3.8	13.9	10.5	-	p
^{6}Li$\|a\rangle$-^{40}K$\|b\rangle$	-3	149.2	1.2	149.7	150.2	0.28	s
^{6}Li$\|a\rangle$-^{40}K$\|b\rangle$	-3	159.5	1.7	159.5	159.6	0.45	s
^{6}Li$\|a\rangle$-^{40}K$\|b\rangle$	-3	165.9	0.6	166.8	165.9	0.001	s
^{6}Li$\|a\rangle$-^{40}K$\|b\rangle$	-3	262.8	10.7	260.7	262.0	-	p
^{6}Li$\|a\rangle$-^{40}K$\|c\rangle$	-2	141.7	1.4	142.5	143.0	0.36	s
^{6}Li$\|a\rangle$-^{40}K$\|c\rangle$	-2	154.9	2.0	154.6	155.1	0.81	s
^{6}Li$\|a\rangle$-^{40}K$\|c\rangle$	-2	162.7	1.7	163.3	162.9	0.60	s
^{6}Li$\|a\rangle$-^{40}K$\|c\rangle$	-2	270.9	13.8	274.0	271.5	-	p

Table 5.1: Heteronuclear Feshbach resonances of ^{6}Li$|a\rangle$-^{40}K$|b\rangle$ found in the inelastic loss spectroscopy scans. Shown are the experimentally determined values of the position B_{res} and width ΔB_{exp}, together with the theoretical results from two different models (see section 5.3 and [62]).

resonances. These results, together with some important properties of the ^{6}Li-^{40}K Feshbach resonances, are discussed in the following section 5.3. Note, that the experimentally measured width ΔB_{exp} of the resonances is different from the width ΔB related to the scattering length singularity. The typical statistical and systematic error in the measured position B_{res} is about 0.5 G for the *s*-wave resonances.

Besides the thirteen new Feshbach resonances between ^{6}Li and ^{40}K, the loss spectra also show two more loss features not attributed to known resonances. In Fig. 5.2, a resonant loss is located at 711.4 G. The loss of ^{40}K$|a\rangle$ could also be reproduces without the presence of ^{6}Li. This indicates a new homonuclear Feshbach resonance for ^{40}K$|a\rangle$. Indeed, model calculations show a f-wave resonance for ^{40}K$|a\rangle$ at this field [118].

Another unidentified loss feature is located at 406.5 G in the ^{6}Li$|a\rangle$-^{40}K$|b\rangle$ loss spectrum. The resonant loss at this field is significantly weaker than the loss at the thirteen heteronuclear Feshbach resonances and it does not appear in every loss spectrum taken around this field. This may indicate a stronger dependance on the temperature or density of the atoms, which was not controlled separately for every scan of this field. We also performed measurements without ^{6}Li atoms to probe the homo- or heteronuclear character. However, due to the weak loss, the measurements did not give a conclusive answer. The theoretical models presented in the following

section 5.3 do not predict a *s*- or *p*-wave heteronuclear Feshbach resonance around this magnetic field. Therefore, the most probable explanation is a higher order resonance, either for $^{40}\mathrm{K}|b\rangle$ or the heteronuclear mixture $^6\mathrm{Li}|a\rangle$-$^{40}\mathrm{K}|b\rangle$. However, further experimental and theoretical work is necessary to fully answer this question.

5.3 Properties of the ^{6}Li-^{40}K Feshbach Resonances

The experimental findings of the resonances in the loss spectra alone is not sufficient for a complete understanding of the ^{6}Li-^{40}K Feshbach Resonances. Many important parameters of the Feshbach resonances like the background scattering length, the involved closed channels, the angular momentum quantum numbers l_o and l_c or the open/closed channel character cannot be directly deduced from the loss spectra. Fortunately, different theoretical models exist that allow to calculate these properties by only knowing the experimentally determined positions. In collaboration with Tobias Tiecke, Jook Walraven, Servaas Kokkelmans, Eite Tiesinga and Paul Julienne, we could fully characterize the ground-state scattering properties of ^{6}Li-^{40}K [62]. This section will discuss the main results.

Two different models were used to interpret the experimental data. One of these models, the asymptotic bound state model (ABM) is presented in section 2.3.2. Fitting the free parameters of the model to the thirteen observed resonance positions allows to assign them to nine *s*-wave and four *p*-wave molecular states. The bound state energies for the four experimentally studied channels are shown in Fig. 5.5 and the theoretical calculated positions are listed in table 5.1. Red dotted lines show the *s*-wave states and blue dashed lines show the *p*-wave states. The open channel threshold is shown by the black solid line. Resonance positions are marked with black dots.

The results from the ABM give a very intuitive picture of the resonance structure. Especially the pattern of the *s*-wave resonances lying close to each other at around 140 G to 220 G is attributed to the flat running molecular levels. *P*-wave resonances occur either at a low field around 15 G or at higher fields above 250 G. The latter *p*-wave resonances show a very broad loss feature in the spectroscopy data. In Fig. 5.5 it can be seen, that the size of these resonances is mainly due to the very small difference in the magnetic moments $\Delta\mu$. This unusual situation leads to *p*-wave resonances that are much larger than the ^{6}Li-^{40}K *s*-wave resonances.

Another notable outcome of the model is the prediction of a *p*-wave Feshbach resonance around 16 G in the $^6\mathrm{Li}|a\rangle$-$^{40}\mathrm{K}|c\rangle$ channel (see Fig. 5.5). This resonance is not recognizable in the experimental data in Fig. 5.4. On the other hand, due to the noisy data in this regime, we cannot exclude the existence of this resonance completely. Another theoretical calculation from Eberhard Tiemann using a different model reproduces our assignments but does not predict the 16 G resonance [119]. Up to now, the existence of this resonance is still an open question. Fine tuning of the potential is also required to improve the theoretical position of the observed *p*-wave resonance at 16.1 G in the $^6\mathrm{Li}|a\rangle$-$^{40}\mathrm{K}|b\rangle$ channel.

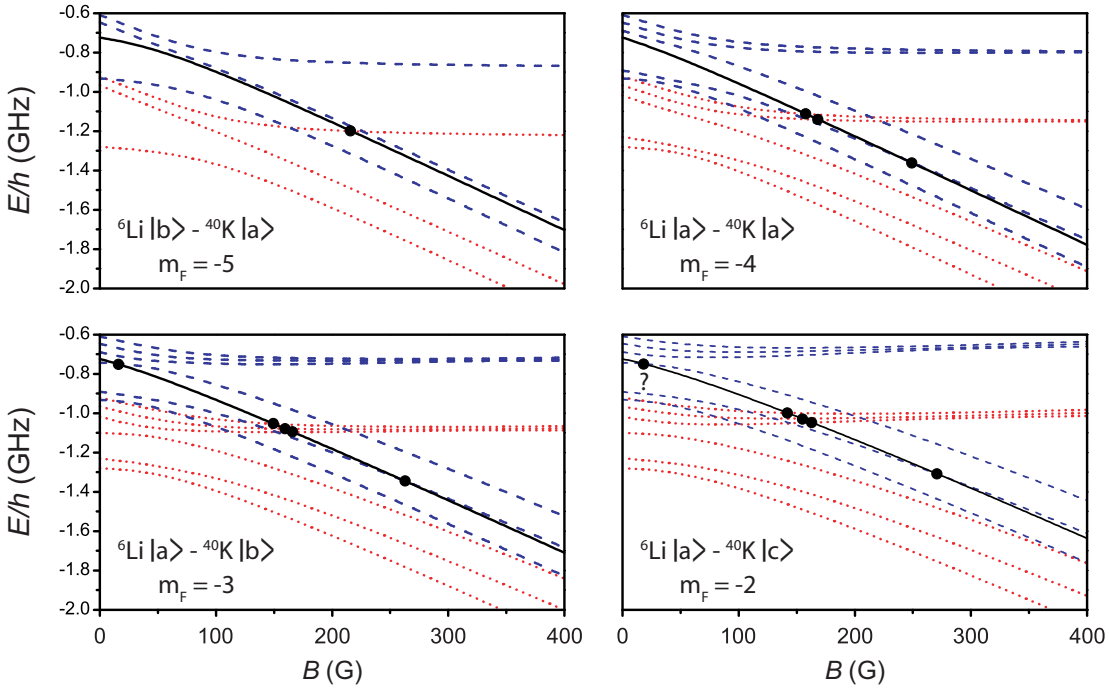

Figure 5.5: Results from the asymptotic bound state model [65]. Red dotted lines show the *s*-wave states and blue dashed lines show the *p*-wave states. The open channel threshold is shown by the black solid line. Resonance positions are marked with black dots.

Further insight into the scattering properties of ^{6}Li-^{40}K can be gained by using an exact coupled-channels model [120] to fit the experimentally observed resonances [62]. The results are also listed in table 5.1. The coupled-channels model can calculate the field dependent *s*-wave scattering length and *p*-wave scattering cross section. This does not only give the positions, but also the widths of the *s*-wave resonances. Although the experimentally measured width cannot be compared directly with the theoretical width, the relative size of the experimental data is reproduces by the coupled-channel model. The determination of the interaction potential also allows to calculate precise values of the singlet and triplet scattering length (see section 2.2.2). The coupled-channel model leads to $a_s = 52.1(3)a_0$ and $a_t = 63.5(1)a_0$, where a_0 is the Bohr radius. Finally, it is possible to calculate the closed and open channel fraction. The nine *s*-wave resonances are all closed-channel dominated.

Once the details of the ^{6}Li-^{40}K interaction potential are fixed by the model calculations, more resonances can be predicted for higher magnetic fields and different channels. The basic pattern of the resonances, which is visible in Fig. 5.5 continues for higher channels. More detailed investigations are currently taking place and will be published in future work.

Chapter 6

Summary and Outlook

This thesis presents the first experimental steps into the world of ultracold interacting heteronuclear Fermi mixtures. This work includes the design and construction of the FeLiKx (Fermionic Li-K experiment) machine and the first experiments to characterize the interaction between ultracold ^{6}Li and ^{40}K atoms.

The design and construction of a machine working with Li, K and Sr atoms required the development of several new or improved technologies. A multi-species oven was developed, which creates a single atomic beam of several species. The oven construction allows long-time operation with small amounts of expensive metals like enriched ^{40}K and the use of several elements with differing operation temperatures. A novel design of an ultra-high vacuum glass cell opened the possibilities to have a very good optical access for different optical dipole traps and high-resolution imaging systems together with the geometrical compactness required to install electromagnetic coils for large magnetic fields. The problem of combining many laser beams of different wavelengths for Li, K and Sr was solved using subsequent stages of optical fibre systems, dichroic mirrors, and achromatic polarizing optics. This concept is especially suited to achieve a stable optical setup that does not require daily realignments. The geometrical layout of the machine foresees future extensions like optical lattices or additional laser systems for Sr. Such upgrades can be implemented without removing the already installed parts.

With the newly build FeLiKx machine, we were able to trap the first mixture of two different fermionic species inside an optical dipole trap. This is an important technological step towards studying heteronuclear fermionic mixtures. The first experiments with this ^{6}Li-^{40}K mixture was to study the feasibility of sympathetic cooling of ^{40}K during the evaporation of ^{6}Li at the well-known 834 G Feshbach resonance. The success of this cooling strategy allowed to explore the magnetic field dependent interactions between the two elements.

Using inelastic loss spectroscopy, we identified thirteen heteronuclear Feshbach resonances for the lowest Zeeman levels of ^{6}Li and ^{40}K. The magnetic field positions of these resonances provided the necessary data for theoretical models to calculate the scattering properties between

ultracold ^{6}Li and ^{40}K [62]. The models predict hundreds of additional resonances for so far unexplored spin states or higher magnetic fields. The *s*-wave scattering length between ^{6}Li and ^{40}K could be determined to be $a_s = 52.1(3)a_0$ for the singlet potential and $a_t = 63.5(1)a_0$ for the triplet potential, where a_0 is the Bohr radius.

The knowledge of the scattering length and Feshbach resonances allows to evaluate the possibilities and strategies for future experiments with fermionic quantum gases with ^{6}Li and ^{40}K. Using one of the Feshbach resonances, the group of Theodor Hänsch and Kai Dieckmann in Munich could produce heteronuclear ^{6}Li-^{40}K molecules with a lifetime of more than 100 ms [121]. The next step towards the exploration of the heteronuclear BEC-BCS crossover requires to cool such molecules into the quantum-degenerate regime. However, as all investigated *s*-wave Feshbach resonances are narrow and closed-channel dominated, the magnetic field range of the crossover is predicted to be very small. Therefore, the technical requirements on the field stability will be higher as for the two known homonuclear systems of ^{6}Li and ^{40}K.

Besides the BEC-BCS crossover, heteronuclear Fermi mixtures offer more possibilities. One example is to study the homonuclear BEC-BCS crossover in the presence of a third, weakly interacting different element. Such mixtures are especially suited to study three-component Fermi gases.

Another field benefitting from the measurements of the ^{6}Li-^{40}K Feshbach resonances is molecular physics. High-precision calculations of the molecular potentials based on data from Feshbach spectroscopy and Fourier transform spectroscopy can be used to study mass-dependent corrections of the important Born-Oppenheimer approximation [122]. Due to the high mass ratio between Li and K, the reduced mass of the dimer is mainly determined by the lightweight Li atom. Consequently, molecules like ^{6}Li^{40}K and ^{7}Li^{40}K are favorable examples because of the high influence from the mass of the Li isotope.

Experiments with ^{6}Li and ^{40}K have just started to contributed important results to the field of ultracold Fermi gases. The continuation of the projects mentioned above will certainly further improve our knowledge about Fermi gases and molecules. Additionally, future projects using more complicated optical potentials like lattices or species selective optical dipole traps will extend the research possibilities with ^{6}Li-^{40}K mixtures. With the first measurements of the interaction properties between ^{6}Li and ^{40}K, the FeLiKx project contributed an important step in these directions and it provides a well-equipped machine for many future experiments.

Acknowledgement

I want to take the opportunity to thank the many people who contributed to the setup, the success and the fun of the FeLiKx project and this thesis.

- I thank our group leader Rudi Grimm for giving me the opportunity to work on this challenging, new project. Rudi's hard work and constant inspiration established a superb research group in Innsbruck. It is this scientific and social background that makes projects like FeLiKx successful and enjoyable.
- Florian Schreck joined Rudi's group the same time I did to co-supervise myself and the FeLiKx project. Without his invaluable experience about all kind of technologies our machine would never work. His open and friendly character made the laborious hours in the lab and outside a really good time. Thank you very much!
- Gerhard Hendl, Gabriel Kerner, Frederik Spiegelhalder, Andreas Trenkwalder, Clarice Aiello and Devang Naik joined the FeLiKx project during the last years and all contributed with their work and ideas. Thank you for all your valuable input and the exciting time.
- I thank the many other students, post-docs and seniors in Rudis group, which were always very helpful with valuable advices.
- The Center for Quantum Physics in Innsbruck also includes the experimental groups of Rainer Blatt and the theory groups of Peter Zoller, Hans-Jürgen Briegel and Helmut Ritsch. I want to thank all members the other *quantum groups* for their friendly support and the good mood.
- All the scientific experiments would not be possible without the administration of the institutes and the professional support from the workshops. Thank you very much for your exceptional efforts and the many things I learned from you.
- My special thanks go to all my old friends from Seligenstadt and Darmstadt, which did not forget me although we could not share a lot of time during the last years. I equally thank my new friends from Innsbruck for all the enjoyable events we had.
- Finally, and most important, I thank all my family for always being there.

Bibliography

[1] G. P. Agrawal and N. K. Dutta, *Semiconductor Lasers* (Kluwer Academic, Boston, 1993).

[2] M. Buchanan, *Mind the Pseudogap*, Nature **409**, 8 (2001).

[3] B. D. Josephson, *The Discovery of Tunnelling Supercurrents*, Rev. Mod. Phys. **46**, 251 (1974).

[4] R. Casalbuoni and G. Nardulli, *Inhomogeneous Superconductivity in Condensed Matter and QCD*, Rev. Mod. Phys. **76**, 263 (2004).

[5] F. Wilczek, *Quantum Chromodynamics: Lifestyles of the Small and Simple*, Nature Phys. **3**, 375 (2007).

[6] M. Inguscio, W. Ketterle, and C. Salomon (eds.), *Ultracold Fermi Gases* (IOS Press, Amsterdam, 2008), Proceedings of the International School of Physics "Enrico Fermi", Course CLXIV, Varenna, 20-30 June 2006.

[7] S. N. Bose, *Plancks Gesetz und Lichtquantenhypothese*, Zeitschrift für Physik **26**, 178 (1924).

[8] A. Einstein, *Quantentheorie des einatomigen idealen Gases*, Sitzungsber. Kgl. Preuss. Akad. Wiss. **1**, 3 (1925).

[9] E. Fermi, *Zur Quantelung des idealen einatomigen Gases*, Zeits. f. Physik **36**, 902 (1926).

[10] P. A. M. Dirac, *On the Theory of Quantum Mechanics*, Proc. Roy. Soc. A **112**, 661 (1926).

[11] R. H. Fowler, *On Dense Matter*, MNRAS **87**, 114 (1926).

[12] A. Sommerfeld, W. V. Houston, and C. Eckart, *Zur Elektronentheorie der Metalle auf Grund der Fermischen Statistik*, Zeits. f. Physik **47**, 1 (1928).

[13] P. Kapitza, *Viscosity of Liquid Helium below the λ-Point*, Nature **141**, 74 (1938).

[14] J. F. Allen and A. D. Misener, *Flow of Liquid Helium II*, Nature **141**, 75 (1938).

[15] H. K. Onnes, *On the Sudden Rate at which the Resistance of Mercury Disappears*, Akad. van Wetenschappen **14**, 818 (1911).

[16] J. Bardeen, L. N. Cooper, and J. R. Schrieffer, *Microscopic Theory of Superconductivity*, Phys. Rev. **106**, 162 (1957).

[17] J. Bardeen, L. N. Cooper, and J. R. Schrieffer, *Theory of Superconductivity*, Phys. Rev. **108**, 1175 (1957).

[18] D. D. Osheroff, R. C. Richardson, and D. M. Lee, *Evidence for a New Phase of Solid ^3He*, Phys. Rev. Lett. **28**, 885 (1972).

[19] J. G. Bednorz and K. A. Müller, *Possible High Tc Superconductivity in the BaLaCuO System*, Z. Phys. B **64**, 189 (1986).

[20] M. H. Anderson, J. R. Ensher, M. R. Matthews, C. E. Wieman, and E. A. Cornell, *Observation of Bose-Einstein Condensation in Dilute Atomic Vapor*, Science **269**, 198 (1995).

[21] M. Inguscio, S. Stringari, and C. E. Wieman (eds.), *Bose-Einstein Condensation in Atomic Gases* (IOS Press, Amsterdam, 1999), Proceedings of the International School of Physics "Enrico Fermi", Course CXL, Varenna, 7-17 July 1998.

[22] B. DeMarco and D. S. Jin, *Onset of Fermi Degeneracy in a Trapped Atomic Gas*, Science **285**, 1703 (1999).

[23] S. Jochim, M. Bartenstein, A. Altmeyer, G. Hendl, S. Riedl, C. Chin, J. Hecker Denschlag, and R. Grimm, *Bose-Einstein Condensation of Molecules*, Science **302**, 2101 (2003).

[24] C. Chin, R. Grimm, P. Julienne, and E. Tiesinga, *Feshbach Resonances in Ultracold Gases* (2008).

[25] M. Fierz, *Über die relativistiche Theorie kräfterfreier Teilchen mit beliebigem Spin*, Helv. Phys. Acta **12**, 3 (1939).

[26] W. Pauli, *The Connection between Spin and Statistics*, Phys. Rev. **58**, 716 (1940).

[27] D. M. Eagles, *Possible Pairing without Superconductivity at Low Carrier Concentrations in Bulk and Thin-film Superconducting Semiconductors*, Phys. Rev. **186**, 456 (1969).

[28] A. J. Leggett, *Diatomic molecules and Cooper pairs*in *Modern Trends in the Theory of Condensed Matter*, A. Pekalski and R. Przystawa, eds. (Springer Verlag, Berlin, 1980), Vol. 115 of Lecture Notes in Physics, p. 13.

[29] S. Giorgini, L. P. Pitaevskii, and S. Stringari, *Theory of Ultracold Fermi Gases*, arXiv:0706.3360v2 (2008).

[30] M. Marini, F. Pistolesi, and G. Strinati, *Evolution from BCS Superconductivity to Bose Condensation: Analytic Results for the Crossover in Three Dimensions*, Eur. Phys. J. B **1**, 151 (1998).

[31] C. Pethick and H. Smith, *Bose-Einstein Condensation in Dilute Gases* (Cambridge University Press, New York, 2008).

[32] P. Nozières and S. Schmitt-Rink, *Bose Condensation in an Attractive Fermion Gas: From Weak to Strong Coupling Superconductivity*, J. Low Temp. Phys. **59**, 195 (1985).

[33] A. Perali, P. Pieri, L. Pisani, and G. C. Strinati, *BCS-BEC Crossover at Finite Temperature for Superfluid Trapped Fermi Atoms*, Phys. Rev. Lett. **92**, 220 404 (2004).

[34] L. P. Gor'kov and T. K. Melik-Barkhudarov, *Contribution to the Theory of Superfluidity in an Imperfect Fermi Gas*, Sov. Phys. JETP **13**, 1018 (1961).

[35] G. B. Partridge, W. Li, R. I. Kamar, Y. Liao, and R. G. Hulet, *Pairing and Phase Separation in a Polarized Fermi Gas*, Science **311**, 503 (2006).

[36] G. B. Partridge, Wenhui Li, Y. A. Liao, R. G. Hulet, M. Haque, and H. T. C. Stoof, *Deformation of a Trapped Fermi Gas with Unequal Spin Populations*, Phys. Rev. Lett. **97**, 190 407 (2006).

[37] M. W. Zwierlein, A. Schirotzek, C. H. Schunck, and W. Ketterle, *Fermionic Superfluidity with Imbalanced Spin Populations*, Science **311**, 492 (2006).

[38] Y. Shin, M. W. Zwierlein, C. H. Schunck, A. Schirotzek, and W. Ketterle, *Observation of Phase Separation in a Strongly Interacting Imbalanced Fermi Gas*, Phys. Rev. Lett. **97**, 030 401 (2006).

[39] A. M. Clogston, *Upper Limit for the Critical Field in Hard Superconductors*, Phys. Rev. Lett. **9**, 266 (1962).

[40] B. S. Chandrasekhar, *A Note on the Maximum Critical Field of High-field Superconductors*, Appl. Phys. Lett. **1**, 7 (1962).

[41] P. Fulde and R. A. Ferrell, *Superconductivity in a Strong Spin-exchange Field*, Phys. Rev. **135**, A550 (1964).

[42] A. I. Larkin and Y. N. Ovchinnikov, *Nonuniform State of Superconductors*, Zh. Eksp. Teor. Fiz. **47**, 1136 (1964).

[43] A. Sedrakian, J. Mur-Petit, A. Polls, and H. Müther, *Pairing in a Two-component Ultracold Fermi Gas: Phases with Broken-Space Symmetries*, Phys. Rev. A **72**, 013 613 (2005).

[44] C. Cohen-Tannoudji, B. Diu, and F. Laloë, *Quantenmechanik* (de Gruyter, Berlin, 1999).

[45] L. Pitaevskii and S. Stringari, *Bose-Einstein Condensation* (Oxford University Press, New York, 2003).

[46] B. H. Bransden and C. J. Joachain, *Physics of Atoms and Molecules* (Pearson Education, Harlow, 2003).

[47] K. M. O'Hara, *Optical Trapping and Evaporative Cooling of Fermionic Atoms*, Ph.D. thesis, Duke University (2000).

[48] F. H. Mies, C. J. Williams, P. S. Julienne, and M. Krauss, *Estimating Bounds on Collisional Relaxation Rates of Spin-polarized ^{87}Rb Atoms at Ultracold Temperatures*, J. Res. Nat. Inst. Stand. Technol. **101**, 521 (1996).

[49] P. J. Leo, E. Tiesinga, P. S. Julienne, D. K. Walter, S. Kadlecek, and T. G. Walker, *Elastic and Inelastic Collisions of Cold Spin-polarized ^{133}Cs Atoms*, Phys. Rev. Lett. **81**, 1389 (1998).

[50] G. Thalhammer, K. Winkler, F. Lang, S. Schmid, R. Grimm, and J. Hecker Denschlag, *Long-lived Feshbach Molecules in a Three-dimensional Optical Lattice*, Phys. Rev. Lett. **96**, 050 402 (2006).

[51] D. S. Petrov, C. Salomon, and G. V. Shlyapnikov, *Weakly Bound Molecules of Fermionic Atoms*, Phys. Rev. Lett. **93**, 090 404 (2004).

[52] D. S. Petrov, C. Salomon, and G. V. Shlyapnikov, *Scattering Properties of Weakly Bound Dimers of Fermionic Atoms*, Phys. Rev. A **71**, 012 708 (2005).

[53] D. S. Petrov, C. Salomon, and G. V. Shlyapnikov, *Diatomic Molecules in Ultracold Fermi Gases − Novel Composite Bosons*, J. Phys. B: At. Mol. Opt. Phys. **38**, S645 (2005).

[54] K. E. Strecker, G. B. Partridge, and R. G. Hulet, *Conversion of an Atomic Fermi Gas to a Long-lived Molecular Bose Gas*, Phys. Rev. Lett. **91**, 080 406 (2003).

[55] C. A. Regal, M. Greiner, and D. S. Jin, *Lifetime of Molecule-Atom Mixtures near a Feshbach Resonance in K*, Phys. Rev. Lett. **92**, 083 201 (2004).

[56] M. Greiner, C. A. Regal, and D. S. Jin, *Emergence of a Molecular Bose-Einstein Condensate from a Fermi Gas*, Nature **426**, 537 (2003).

[57] T. Köhler, K. Góral, and P. S. Julienne, *Production of Cold Molecules via Magnetically Tunable Feshbach Resonances*, Rev. Mod. Phys. **78**, 1311 (2006).

[58] M. Theis, G. Thalhammer, K. Winkler, M. Hellwig, G. Ruff, R. Grimm, and J. Hecker-Denschlag, *Tuning the Scattering Length with an Optically Induced Feshbach Resonance*, Phys. Rev. Lett. **93**, 123 001 (2004).

[59] A. D. Lange, K. Pilch, A. Prantner, F. Ferlaino, B. Engeser, H.-C. Naegerl, R. Grimm, and C. Chin, *Determination of Atomic Scattering Lengths from Measurements of Molecular Binding Energies near Feshbach Resonances*, arXiv:0810.5503v1 .

[60] A. Marte, *Feshbach-Resonanzen bei Stößen ultrakalter Rubidiumatome*, Ph.D. thesis, Technische Universität München (2003).

[61] R. A. Duine and H. T. C. Stoof, *Atom-molecule Coherence in Bose Gases*, Phys. Rep. **396**, 115 (2004).

[62] E. Wille, F. M. Spiegelhalder, G. Kerner, D. Naik, A. Trenkwalder, G. Hendl, F. Schreck, R. Grimm, T. G. Tiecke, J. T. M. Walraven, S. J. J. M. F. Kokkelmans, E. Tiesinga, and P. S. Julienne, *Exploring an Ultracold Fermi-Fermi Mixture: Interspecies Feshbach Resonances and Scattering Properties of ^{6}Li and ^{40}K*, Phys. Rev. Lett. **100**, 053 201 (2008).

[63] A. J. Moerdijk, B. J. Verhaar, and A. Axelsson, *Resonances in Ultracold Collisions of ^{6}Li, ^{7}Li, and ^{23}Na*, Phys. Rev. A **51**, 4852 (1995).

[64] C. A. Stan, M. W. Zwierlein, C. H. Schunck, S. M. F. Raupach, and W. Ketterle, *Observation of Feshbach Resonances between Two Different Atomic Species*, Phys. Rev. Lett. **93**, 143 001 (2004).

[65] T. G. Tiecke, J. T. M. Walraven, and S. J. J. M. F. Kokkelmans, private communication.

[66] M. Bartenstein, A. Altmeyer, S. Riedl, R. Geursen, S. Jochim, C. Chin, J. Hecker Denschlag, R. Grimm, A. Simoni, E. Tiesinga, C. J. Williams, and P. S. Julienne, *Precise Determination of ^{6}Li Cold Collision Parameters by Radio-frequency Spectroscopy on Weakly Bound Molecules*, Phys. Rev. Lett. **94**, 103 201 (2005).

[67] C. H. Schunck, M. W. Zwierlein, C. A. Stan, S. M. F. Raupach, and W. Ketterle, *Feshbach Resonances in Fermionic ^{6}Li*, Phys. Rev. A **71**, 045 601 (2005).

[68] J. Zhang, E. G. M. van Kempen, T. Bourdel, L. Khaykovich, J. Cubizolles, F. Chevy, M. Teichmann, L. Taruell, S. J. J. M. F. Kokkelmans, and C. Salomon, *P-wave Feshbach Resonances of Ultracold ^{6}Li*, Phys. Rev. A **70**, 030 702(R) (2004).

[69] C. A. Regal, C. Ticknor, J. L. Bohn, and D. S. Jin, *Tuning p-wave Interactions in an Ultracold Fermi Gas of Atoms*, Phys. Rev. Lett. **90**, 053 201 (2003).

[70] C. A. Regal and D. S. Jin, *Measurement of Positive and Negative Scattering Lengths in a Fermi Gas of Atoms*, Phys. Rev. Lett. **90**, 230 404 (2003).

[71] C. Ticknor, C. A. Regal, D. S. Jin, and J. L. Bohn, *Multiplet Structure of Feshbach Resonances in Non-zero Partial Waves*, Phys. Rev. A **69**, 042 712 (2004).

[72] C. D. Aiello, *Robust Coil System for Experiments with Ultracold Atoms*, Unpublished Report, Innsbruck University (2007).

[73] A. Trenkwalder, *Design of a Resonator Enhanced Optical Dipole Trap for Fermionic Mixtures*, Diploma Thesis, Innsbruck University (2007).

[74] M. Greiner, I. Bloch, T. W. Hänsch, and T. Esslinger, *Magnetic Transport of Trapped Cold Atoms over a Large Distance*, Phys. Rev. A **63**, 031 401 (2001).

[75] T. L. Gustavson, A. P. Chikkatur, A. E. Leanhardt, A. Görlitz, S. Gupta, D. E. Pritchard, and W. Ketterle, *Transport of Bose-Einstein Condensates with Optical Tweezers*, Phys. Rev. Lett. **88**, 020 401 (2001).

[76] W. D. Phillips and H. Metcalf, *Laser Deceleration of an Atomic Beam*, Phys. Rev. Lett. **48**, 596 (1982).

[77] K. Dieckmann, R. J. C. Spreeuw, M. Weidemüller, and J. T. M. Walraven, *Two-dimensional Magneto-optical Trap as a Source of Slow Atoms*, Phys. Rev. A **58**, 3891 (1998).

[78] T. Tiecke, A. Ludewig, S. Kraft, S. Gensemer, and J. Walraven, *An Intense Clean Source for Cold Lithium*, DPG Verhandlungen 2008 Q 62.1 .

[79] B. DeMarco, H. Rohner, and D. S. Jin, *An Enriched ^{40}K Source for Fermionic Atom Studies*, Rev. Sci. Instrum. **70**, 1967 (1999).

[80] M. Taglieber, A.-C. Voigt, T. Aoki, T. W. Hänsch, and K. Dieckmann, *Quantum Degenerate Two-species Fermi-Fermi Mixture Coexisting with a Bose-Einstein Condensate*, Phys. Rev. Lett. **100**, 010 401 (2008).

[81] T. Tiecke, A. Ludewig, S. Kraft, S. Gensemer, and J. Walraven, *An Ultracold Fermion Mixture of ^{6}Li and ^{40}K*, ICAP 2008 poster TU122 .

[82] A. N. Nesmeyanov, *Vapour Pressure of the Elements* (Academic Press, New York, 1963).

[83] X. Zeng, Z. Wu, T. Call, E. Miron, D. Schreiber, and W. Happer, *Experimental Determination of the Rate Constants for Spin Exchange between Optically Pumped K, Rb, and Cs Atoms and ^{129}Xe Nuclei in Alkali-metal-noble-gas van der Waals Molecules*, Phys. Rev. A **31**, 260 (1985).

[84] M. Asano and K. Kubo, *Vapor Pressure of Strontium below 660°K*, J. Nucl. Sci. Technol. **15**, 765 (1978).

[85] A. J. Boerboom, H. W. Reyn, and J. Kistemaker, *Heat of Sublimation and Vapour Pressure of Strontium*, Physica **30**, 254 (1964).

[86] Y. Priselkov and A. N. Nesmeyanov, *Determination of the Vapor Pressures of Calcium and Strontium Below their Melting Points*, Dokl. Akad. Nauk SSSR **95**, 1207 (1954).

[87] I. Courtillot, *Première observation de la transition fortement interdite $^1S_0$-$^3P_0$ du strontium, pour une horloge optique à atomes piégés*, Ph.D. thesis, Université de Paris VI (2003).

[88] S. Kroboth, *Laserkühlung von Ytterbiumatomen*, Diploma Thesis, University of Stuttgart (2002).

[89] C. A. Stan and W. Ketterle, *Multiple Species Atom Source for Laser-cooling Experiments*, Rev. Sci. Instrum. **76**, 063 113 (2005).

[90] I. Courtillot, A. Quessada, R. P. Kovacich, J.-J. Zondy, A. Landragin, A. Clairon, and P. Lemonde, *Efficient Cooling and Trapping of Strontium Atoms*, Opt. Lett. **28**, 468 (2003).

[91] K. Pilch, A. D. Lange, A. Prantner, G. Kerner, F. Ferlaino, H.-C. Naegerl, and R. Grimm, *Observation of Interspecies Feshbach Resonances in an Ultracold Rb-Cs Mixture*, arXiv:0812.3287v1 .

[92] A. Mosk, S. Jochim, T. Elsässer, M. Weidemüller, and R. Grimm, *Resonator-enhanced Optical Dipole Trap for Fermionic Lithium Atoms*, Optics Lett. **26**, 1837 (2001).

[93] F. Schreck, Mounting of the FeLiKx Experiment Hellma Glass Cell, http://iqoqi006.uibk.ac.at/users/c704250/lab/GlasscellMountingCompressed.pdf.

[94] J. Walls, R. Ashby, J. Clarke, B. Lu, and W. Wijngaarden, *Measurement of Isotope Shifts, Fine and Hyperfine Structure Splittings of the Lithium D Lines*, Eur. Phys. J. D **22**, 159 (2003).

[95] G. Camy, C. J. Bordé, and M. Ducloy, *Heterodyne Saturation Spectroscopy through Frequency Modulation of the Saturating Beam*, Optics Communications **41**, 325 (1982).

[96] R. S. Williamson III, *Magneto-optical Trapping of Potassium Isotopes*, Ph.D. thesis, University of Wisconsin-Madison (1997).

[97] U. Schünemann, H. Engler, R. Grimm, M. Weidemüller, and M. Zielonkowski, *Simple Scheme for Tunable Frequency Offset Locking of Two Lasers*, Rev. Sci. Instrum. **70**, 242 (1999).

[98] G. Ferrari, M. Mewes, F. Schreck, and C. Salomon, *High-power Multiple-frequency Narrow-linewidth Laser Source Based on a Semiconductor Tapered Amplifier*, Opt. Lett. **24**, 151 (1999).

[99] G. Ferrari, R. E. Drullinger, N. Poli, F. Sorrentino, and G. M. Tino, *Cooling of Sr to High Phase-space Density by Laser and Sympathetic Cooling in Isotopic Mixtures*, Phys. Rev. A **73**, 023 408 (2006).

[100] T. P. Dinneen, K. R. Vogel, E. Arimondo, J. L. Hall, and A. Gallagher, *Cold Collisions of Sr*-Sr in a Magneto-optical Trap*, Phys. Rev. A **59**, 1216 (1999).

[101] F. Sorrentino, G. Ferrari, N. Poli, R. Drullinger, and G. M. Tino, *Laser Cooling and Trapping of Atomic Strontium for Ultracold Atom Physics, High-precision Spectroscopy and Quantum Sensors*, Modern Physics Letters B **20**, 1287 (2006).

[102] A. Traverso, R. Chakraborty, Y. N. Martinez de Escobar, P. G. Mickelson, S. B. Nagel, M. Yan, and T. C. Killian, *Inelastic and Elastic Collision Rates for Triplet States of Ultracold Strontium*, arXiv:0809.0936v1 .

[103] H. J. Metcalf and P. van der Straten, *Laser Cooling and Trapping* (Springer, New York, 1999).

[104] W. Süptitz, G. Wokurka, F. Strauch, P. Kohns, and W. Ertmer, *Simultaneous Cooling and Trapping of ^{85}Rb and ^{87}Rb in a Magneto-optical Trap*, Opt. Lett. **19**, 1571 (1994).

[105] M. S. Santos, P. Nussenzveig, L. G. Marcassa, K. Helmerson, J. Flemming, S. C. Zilio, and V. S. Bagnato, *Simultaneous Trapping of two Different Atomic Species in a Vapor-cell Magneto-optical Trap*, Phys. Rev. A **52**, R4340 (1995).

[106] G. D. Telles, L. G. Marcassa, S. R. Muniz, S. G. Miranda, A. Antunes, C. Westbrook, and V. S. Bagnato, *Inelastic Cold Collisions of a Na/Rb Mixture in a Magneto-optical Trap*, Phys. Rev. A **59**, R23 (1999).

[107] J. P. Shaffer, W. Chalupczak, and N. P. Bigelow, *Photoassociative Ionization of Heteronuclear Molecules in a Novel Two-species Magneto-optical Trap*, Phys. Rev. Lett. **82**, 1124 (1999).

[108] M.-O. Mewes, G. Ferrari, F. Schreck, A. Sinatra, and C. Salomon, *Simultaneous Magneto-optical Trapping of Two Lithium Isotopes*, Phys. Rev. A **61**, 011 403 (1999).

[109] U. Schlöder, H. Engler, U. Schünemann, R. Grimm, and M. Weidemüller, *Cold Inelastic Collisions Between Lithium and Cesium in a Two-species Magneto-optical Trap*, Eur. Phys. J. D **7**, 331 (1999).

[110] V. Wippel, C. Binder, and L. Windholz, *Cross-section for Collisions of Ultracold Li with Na*, Eur. Phys. J. D **21**, 101 (2002).

[111] M. Taglieber, A.-C. Voigt, F. Henkel, S. Fray, T. W. Hänsch, and K. Dieckmann, *Simultaneous Magneto-optical Trapping of Three Atomic Species*, Physical Review A **73**, 011 402 (2006).

[112] S. Tassy, N. Nemitz, F. Baumer, C. Höhl, A. Batär, and A. Görlitz, *Sympathetic Cooling in a Mixture of Diamagnetic and Paramagnetic Atoms*, arXiv:0709.0827v1 .

[113] R. Grimm, M. Weidemüller, and Y. B. Ovchinnikov, *Optical Dipole Traps for Neutral Atoms*, Adv. At. Mol. Opt. Phys. **42**, 95 (2000).

[114] G. Modugno, G. Ferrari, G. Roati, R. J. Brecha, A. Simoni, and M. Inguscio, *Bose-Einstein Condensation of Potassium Atoms by Sympathetic Cooling*, Science **294**, 1320 (2001).

[115] F. Schreck, G. Ferrari, K. L. Corwin, J. Cubizolles, L. Khaykovich, M.-O. Mewes, and C. Salomon, *Sympathetic Cooling of Bosonic and Fermionic Lithium Gases Towards Quantum Degeneracy*, Phys. Rev. A **64**, 011 402 (2001).

[116] I. Bloch, M. Greiner, O. Mandel, T. W. Hänsch, and T. Esslinger, *Sympathetic Cooling of ^{85}Rb and ^{87}Rb*, Phys. Rev. A **64**, 021 402 (2001).

[117] A. G. Truscott, K. E. Strecker, W. I. McAlexander, G. B. Partridge, and R. G. Hulet, *Observation of Fermi Pressure in a Gas of Trapped Atoms*, Science **291**, 2570 (2001).

[118] J. Bohn, private communication.

[119] E. Tiemann, private communication.

[120] H. T. C. Stoof, J. M. V. A. Koelman, and B. J. Verhaar, *Spin-exchange and Dipole Relaxation Rates in Atomic Hydrogen: Rigorous and Simplified Calculations*, Phys. Rev. B **38**, 4688 (1988).

[121] A.-C. Voigt, M. Taglieber, L. Costa, T. Aoki, W. Wieser, T. Hänsch, and K. Dieckmann, *Ultracold Heteronuclear Fermi-Fermi Molecules*, arXiv:0810.1306v1 .

[122] S. Falke, H. Knöckel, J. Friebe, M. Riedmann, E. Tiemann, and C. Lisdat, *Potassium Ground-state Scattering Parameters and Born-Oppenheimer Potentials from Molecular Spectroscopy*, Phys. Rev. A **78**, 012 503 (2008).